

**NANOCARBON/POLYMER BRUSH MATERIALS: SYNTHESIS,
CHARACTERIZATION AND APPLICATION**

By

Lang Li

Dissertation

Submitted to the Faculty of the
Graduate School of Vanderbilt University
in partial fulfillment of the requirements

for the degree of

DOCTOR OF PHILOSOPHY

in

Chemistry

December, 2007

Nashville, Tennessee

Approved

Professor Eva M. Harth

Professor Jimmy L. Davidson

Professor Timothy P. Hanusa

Professor David W. Wright

Professor Charles M. Lukehart

ACKNOWLEDGEMENTS

The most important person I would like to thank is, of course, my research advisor, Prof. Charles M. Lukehart. He has been instrumental in ensuring my academic, financial and professional well being during the past five years. In every sense, none of this work would have been possible without his guidance, support, and patience. Many thanks also go to my committee members, Prof. Jimmy L. Davidson, Prof. Timothy P. Hanusa, Prof. David W. Wright, and Professor Eva M. Harth for their time and effort.

I would like to thank Dr. Jiang Li and Prof. W. Katie Zhong for their initial work on surface-functionalization of GCNFs and warm-hearted help at my early stage entering this work. I would like to thank Prof. L. Roy Xu, Ping Wang and Huachen Kuai for their help and collaboration on nanocomposites fabrication and mechanical property measurement. In addition, I also want to thank Blake T. Branson for providing hardness testing data for nanocomposites. I need to thank Drs. R. Cueto and P. Russo of the Biodynamics Institute, Louisiana State University, for providing determinations of polymer molecular weights and polydispersity by GPC-MALLS, and Teresa.A.Croce for GPC analysis.

Moreover, I would like to thank Dr. Grace K. Zoorob, Andrzej Balinski, and Yang Fu for their effort and training on instrumentations. I have been very fortunate to work in Lukehart group and I am grateful for the time with all group members: Dr. Lisa M.

Sullivan, Jason A. Michel, William H. Morris, and Matthew S. Wellons.

This work would not have been possible without the financial support of Vanderbilt University (Discovery Grant), the Department of Chemistry, the Graduate School, the Vanderbilt Institute of Nanoscale Science and Engineering, National Science Foundation (No. CTS-0210366), and U.S. Army Research Office (No. W911NF-04-2-0023).

TABLE OF CONTENTS

	Page
ACKNOWLEDGEMENTS	ii
LIST OF TABLES	vi
LIST OF FIGURES	viii
LIST OF SCHEMES	xiv
Chapter	
I. INTRODUCTION	1
1.1. Nanocarbon Materials	1
1.2. Graphitic Carbon Nanofibers	3
1.3. Ultradispersed Diamond	8
1.4. Surface Chemistry of Nanocarbon Materials	12
1.5. Atom Transfer Radical Polymerization for Surface Functionalization	14
1.6. Dissertation Overview	20
II. SYNTHESIS OF GCNF/POLYMER BRUSHES VIA ATOM TRANSFER RADICAL POLYMERIZATION	24
2.1. Introduction	24
2.2. Experimental Section	25
2.3. Results and Discussion	37
2.4. Conclusions	67
III. SYNTHESIS OF UDD/POLYMER BRUSHES VIA ATOM TRANSFER RADICAL POLYMERIZATION	69
3.1. Introduction	69
3.2. Experimental Section	71
3.3. Results and Discussion	83
3.4. Conclusions	116
IV. APPLICATION OF GCNF/POLYMER BRUSHES AS GAS SENSORS	118

4.1. Introduction	118
4.2. Experimental Section	120
4.3. Results and Discussion	122
4.4. Conclusions	130
V. APPLICATION OF NANOCARBON/POLYMER HYBRID MATERIALS IN POLYMER COMPOSITES	132
5.1. Introduction	132
5.2. Experimental Section	134
5.3. Results and Discussion	137
5.4. Conclusions	150
Appendix	
A. SYNTHESIS OF UDD/EPOXIDE HYBRID MATERIALS VIA RING-OPENING REACTIONS	151
B. SYNTHESIS OF GCNF/EPOXIDE HYBRID MATERIALS VIA RING-OPENING REACTIONS	167
BIBLIOGRAPHY	178

LIST OF TABLES

Table 1. Selected properties of ultradispersed diamond nanocrystals. (Reprinted from ref. 3. Copyright of 2002 Marcel Dekker, Inc.).....	11
Table 2. Elemental analysis results of GCNFs and relative materials	38
Table 3. Conditions and results of ATRP of n-butyl acrylate initiated by GCNF-HBBP-Br.	40
Table 4. Conditions and results of ATRP of nBA initiated by HBBP.	49
Table 5. Conditions and results of ATRP of iBMA in 50% acetone.	53
Table 6. Conditions and results of ATRP of tBA in 50% acetone.	58
Table 7. Conditions and results of ATRP of glycidyl methacrylate initiated by GCNF-Cl.....	65
Table 8. Conditions and results of ATRP of <i>iso</i> -BMA with Br-based initiators in acetone ^a	76
Table 9. Conditions and results of ATRP of <i>iso</i> -BMA with Cl-based initiators in acetone. ^a	78
Table 10. Conditions and results of ATRP of tert-BMA in toluene. ^a	80
Table 11. Elemental analysis of initiator-immobilized UDD samples.....	86
Table 12. Experimental conditions of ATRP to prepare UDD-POMA polymer brushes.	104
Table 13. Experimental conditions of ATRP to prepare UDD-PGMA brushes	112
Table 14. Response sensitivity comparison $(R_v - R_0)/R_0$ of as-prepared GCNF and GCNF-ODA sensors to various organic vapors.....	124
Table 15. Composite specimens with different reinforcement materials incorporated....	138
Table 16. Epoxy/UDD-PGMA nanocomposite specimens with different UDD loading	142
Table 17. Conditions and results of ring-opening reaction of a variety of epoxides with as-received UDD.....	156

Table 18. Conditions and results of ring-opening polymerization of glycidol with as-received UDD particles.....	162
Table 19. Conditions and results of ring-opening reaction of various epoxides with oxidized GCNF nanofibers	171

LIST OF FIGURES

Figure 1. Classification of nanocarbon structures based on the carbon bond hybridization. (Reprinted from ref. 3. Copyright of 2002 CRC Press, Inc.).....	2
Figure 2. Three different types of SWNT (left) and MWNT constructed of three shells of different chiralities (right). (Reprinted from ref. 6. Copyright of 2005 Willey-VCH.)	2
Figure 3. Schematic illustration of mechanism for the growth of a carbon nanofiber from methane catalyzed by a nickel particle via <i>in situ</i> TEM images. (Reprinted from ref. 16. Copyright of 2004 Nature Publishing Group.)	4
Figure 4. Primary structures of three types of graphitic carbon nanofibers with different graphitic sheets orientation: (a) platelet, (b) ribbon, (c) herringbone. (Reprinted from ref. 17. Copyright of 1997 Elsevier B. V.).....	5
Figure 5. Schematic illustration of the controlled detonation synthesis of nanodiamond from carbon containing explosives. (Reprinted from ref. 3. Copyright of 2002 Marcel Dekker, Inc.)	8
Figure 6. Schematic illustration of the structures of a primary UDD particle in detonation soot. (Reprinted from ref. 43. Copyright of 1999 American Institute of Physics.)	10
Figure 7. Oxygen-containing groups a) carboxyl, b) carboxy anhydride, c) lactone, d) phenol, e) carbonyl, f) quinone, and g) ether groups at the edge of a graphite plane. (Reprinted from ref. 56. Copyright of 2002 Wiley-VCH.).....	13
Figure 8. Examples of polymer brushes synthesized by ATRP using “grafting from” approach from various substrates of flat wafers, particles, colloids and polymers. (Reprinted from ref. 79. Copyright of 2003 Wiley-VCH.).....	18
Figure 9. Synthesis of polymer brushes on MWNTs via a “grafting from” ATRP strategy. (Reprinted from ref. 82. Copyright of 2004 American Chemical Society.).....	19
Figure 10. FT-IR spectra of (a) GCNFs, (b) GCNF-HBBP-Br, (c) GCNF-CO ₂ H and (d) GCNF-PBA4.....	40
Figure 11. TGA curves of as-prepared GCNFs, surface-functionalized GCNFs, and PBA.....	42
Figure 12. Dispersibility of (A) GCNF-CO ₂ H sample in chloroform, (B) GCNF-PBA3 sample in chloroform, (C) GCNF-PBA3 sample in toluene, (D) GCNF-PBA3 sample in	

methanol. Concentration of the dispersions is about 2.5 mg/mL.	43
Figure 13. ¹ H-NMR spectra of (A) PBA, (B) GCNF-PBA3 in CDCl ₃	45
Figure 14. TEM images of (A) as-prepared GCNFs and (B), (C) GCNF-PBA3 samples.	46
Figure 15. BET specific surface area of (A) GCNFs, (B) GCNF-CO ₂ H, (C) GCNF-PBA1, (D) GCNF-PBA2, (E) GCNF-PBA3, (F) GCNF-PBA4.....	48
Figure 16. TGA curves of GCNFs, c-GCNFs, GCNF-CO ₂ H, c-GCNF-CO ₂ H, and GCNF-PBA4 samples.....	51
Figure 17. BET specific surface area of GCNFs, c-GCNFs, GCNF-CO ₂ H, and c-GCNF-CO ₂ H.....	51
Figure 18. FT-IR spectra of GCNF-CO ₂ H, GCNF-HEBP-Br, and GCNF-PiBMA.	54
Figure 19. TGA curves of GCNF-CO ₂ H, GCNF-HEBP-Br, c-GCNF-CO ₂ H, GCNF-PiBMA, and PiBMA samples	54
Figure 20. BET specific surface area of (A) GCNF, (B) GCNF-CO ₂ H, (C) c-GCNF-CO ₂ H, and (D) GCNF-PiBMA.....	55
Figure 21. TEM images of individual GCNF-PiBMA carbon nanofiber.....	56
Figure 22. Dispersibility of (A) GCNF-CO ₂ H sample in CCl ₄ , (B), (C), (D) (E) GCNF-PiBMA sample in H ₂ O/CCl ₄ , toluene/H ₂ O, acetone, and methanol, respectively. Concentration of the dispersions is about 2.5mg/mL.	57
Figure 23. TGA curves of GCNF-CO ₂ H, GCNF-HEBP-Br, c-GCNF-CO ₂ H, GCNF-PtBA, GCNF-PAA2, GCNF-PtBA2, and PtBA.	60
Figure 24. BET specific surface area of (A) GCNF, (B) GCNF-CO ₂ H, (C) c-GCNF-CO ₂ H, and GCNF-PtBA samples.	60
Figure 25. Dispersibility test of (A) and (B) GCNF-PtBA2 samples in H ₂ O (upper)/CHCl ₃ (lower) and toluene (upper)/H ₂ O (lower); (C) and (D) GCNF-PAA2 samples in H ₂ O (upper)/CHCl ₃ (lower) and toluene (upper)/H ₂ O (lower).....	61
Figure 26. TGA curves of oxidized GCNF (GCNF-CO ₂ H), chlorine initiator immobilized GCNF (GCNF-Cl) and PGMA brushes grafted GCNF (GCNF-PGMA).....	63
Figure 27. FTIR spectra of oxidized GCNF (GCNF-CO ₂ H), chlorine initiator immobilized GCNF (GCNF-Cl) and PGMA brushes grafted GCNF (GCNF-PGMA).....	64

Figure 28. Dependence of grafted PGMA brushes on the surface of GCNF nanofibers on the polymerization time of surface-initiated ATRP.....	66
Figure 29. TGA curves of GCNF-PGMA3 samples at different time intervals during the 48 h ATRP course.....	67
Figure 30. TEM images of as-received UDD particles.....	83
Figure 31. AFM tapping-mode height image (A) and phase image (B) of an individual as-received UDD particle as spin-coated onto a mica surface.....	84
Figure 32. XRD patterns of as-received UDD and oxidized UDD, UDD-CO ₂ H, samples.....	86
Figure 33. FT-IR spectra of UDD, UDD-CO ₂ H, UDD-Br, and UDD-PiBMA-Br samples.....	88
Figure 34. Solution ¹ H-NMR spectra of UDD-PiBMA-1 brush and of PiBMA in CDCl ₃ solution.....	89
Figure 35. TGA curves of UDD-CO ₂ H, UDD-Br, UDD-PiBMA-1, and PiBMA samples... ..	90
Figure 36. TEM images of UDD-PiBMA-1 sample.....	91
Figure 37. AFM tapping-mode height image (A and B) and phase image (C) of an individual UDD-PiBMA-1 brush as spin-coated onto a mica surface.....	92
Figure 38. BET analysis of (A) UDD, (B) UDD-CO ₂ H, (C) c-UDD-1, and UDD-PiBMA-1 samples.....	93
Figure 39. Dispersibility test: (A) UDD in acetone; (B), (C), (D), (E) UDD-PiBMA-1 in acetone, toluene/H ₂ O, H ₂ O/CCl ₄ , and MeOH. Concentration of the dispersions is about 2.5 mg/mL.....	94
Figure 40. FT-IR spectra of UDD, UDD-Cl, and of UDD-PiBMA-2.....	96
Figure 41. TGA curves of UDD, UDD-Cl, c-UDD-2, UDD-PiBMA-2, and PiBMA-1 samples.....	97
Figure 42. AFM tapping-mode height image (left) and phase image (right) of an individual UDD-PiBMA-2 brush as spin-coated onto a mica surface.....	98
Figure 43. BET analysis of specific surface area of UDD, c-UDD-2, and UDD-PiBMA-2	

samples.....	99
Figure 44. Dispersibility test: (A) UDD in CCl ₄ ; (B), (C), (D), (E) UDD-PiBMA-2 in H ₂ O/CCl ₄ , toluene/H ₂ O, acetone, and MeOH. Concentration of the dispersions is about 2.5 mg/mL.....	100
Figure 45. TGA curves of UDD, UDD-Cl, c-UDD-3, UDD-PtBMA, and PtBMA.	101
Figure 46. BET analysis of specific surface area of UDD, c-UDD-3, and UDD-PtBMA samples.....	102
Figure 47. Dispersibilities (ca. 2.5 mg/mL) of the hydrophobic UDD-PtBMA brush, in water(upper)/CHCl ₃ (lower), vial A, and in toluene(upper)/water(lower), vial B, contrasted with that of the hydrophilic UDD-PMAA brush in toluene(upper)/water(lower), vial C, and in water(upper)/CHCl ₃ (lower), vial D.....	103
Figure 48. Kinetic plots of polymer brush content versus polymerization time: UDD-POMA-1 (square) [OMA]:[TCE]:[PMDETA]:[CuCl] =100:0:1:1; UDD-POMA-2 (circle) [OMA]:[TCE]:[PMDETA]:[CuCl]:[CuCl ₂] =100:0:1.1:1:0.1; UDD-POMA-3 (triangle) [OMA]:[TCE]: [PMDETA]:[CuCl] =100:1:1:1.....	105
Figure 49. FT-IR spectra of as-received UDD, UDD-POMA polymer brush, and POMA polymer.	106
Figure 50. TGA curves of UDD-Cl, UDD-POMA-1 aliquots of 1 h, 4 h, and 24 h, and POMA polymer.	108
Figure 51. ¹ H-NMR spectra of UDD-POMA-4 (polymer content 20 wt%), UDD-POMA-1 (polymer content 55 wt%), and POMA polymer in CDCl ₃	109
Figure 53. Tapping mode AFM images of UDD-POMA polymer brush spin-coated on a mica surface: A) Height image, B) Phase image, C) Cross-intersectional height profile.....	110
Figure 53. High-resolution optical microscopic images of as-received UDD (left) and UDD-POMA-1 (right) in transformer oil at the concentration of 2.5 mg/mL at room temperature.	111
Figure 54. Kinetic plot of polymer brush content versus polymerization time of UDD-PGMA-3 ([GMA]: [PMDETA]:[CuBr]=100:1:1).	113
Figure 55. FT-IR spectra of as-received UDD, UDD-PGMA polymer brush, and PGMA polymer.	114

Figure 56. TGA curves of as-received UDD, UDD-PGMA polymer brush samples with different polymerization time of 4 h, 24 h, and 120 h, and PGMA polymer.	115
Figure 57. BET analysis of specific surface area of A) as-received UDD, B) UDD-Cl, and C) UDD-PGMA-1 polymer brush.....	116
Figure 58. Construction of GCNF/polymer brushes sensors on an interdigitated microelectrode chip (electrode pairs a-a and b-b are connected to multimeter, respectively).....	120
Figure 59. As-prepared GCNF/IME sensor response cycled between ambient atmosphere and acetone, chloroform, methanol, and toluene saturated vapor atmospheres.....	122
Figure 60. GCNF-ODA/IME sensor response cycled between ambient atmosphere and acetone, chloroform, methanol, and toluene saturated vapor atmospheres.	123
Figure 61. GCNF-PBA/IME sensor response cycled between ambient atmosphere and tetrahydrofuran (THF), acetone, toluene, methanol, chloroform, and hexane saturated vapor atmospheres.	126
Figure 62. GCNF-PAA/IME sensor response to tetrahydrofuran (THF), methanol, triethylamine (TEA), and dimethylformamide (DMF) saturated vapor atmospheres.	128
Figure 63. GCNF-PAA sensor response cycled between ambient atmosphere and exposure to NH ₃ vapor atmosphere over 29 wt% aqueous ammonia.....	130
Figure 64. Rockwell E hardness of composite specimens of PE-1 (pure epoxy), CB-1 (epoxy/carbon black), PB-1 (epoxy/UDD), and NC-1 (epoxy/UDD-PGMA).	140
Figure 65. Optical images of composite specimens of A) PE-1 (pure epoxy), B) PB-1 (epoxy/UDD), and C) NC-1 (epoxy/UDD-PGMA).....	141
Figure 67. Iosipescu shear test (left) and Butt-joint tensile test (right) joints.....	144
Figure 68. Shear strength of a series of PMMA-PMMA joints bonded by epoxy/r-GCNF-ODA nanocomposite adhesives with different r-GCNF-ODA loading ..	146
Figure 69. Tensile strength of a series of PMMA-PMMA joints bonded by epoxy/r-GCNF-ODA nanocomposite adhesives with different r-GCNF-ODA loading ..	148
Figure 70. Tensile strength of a series of Al-Al joints bonded by epoxy/r-GCNF-ODA nanocomposite adhesives with different r-GCNF-ODA loading.....	149
Figure 71. FT-IR spectra of as-received UDD and UDD/epoxide hybrid materials with	

various functionalities.....	157
Figure 72. BET results of as-received UDD and UDD/epoxide hybrid materials with various functionalities.....	158
Figure 73. TGA mass-loss curves of as-received UDD and UDD-epoxide hybrid materials with various functionalities.....	159
Figure 74. FT-IR spectra of as-received UDD, UDD-PGE-1 and hydrolyzed UDD-PGE-1.....	160
Figure 75. XRD scans of as-received UDD and UDD-Glycidol-1.....	161
Figure 76. TGA mass-loss curves of UDD-Glycidol-1 at different reaction time.....	164
Figure 77. Grafted polymer amount as a function of reaction time for UDD-Glycidol-1 and UDD-Glycidol-2.....	165
Figure 78. FT-IR spectra of GCNF-CO ₂ H and GCNF/epoxide hybrid materials.....	172
Figure 79. TGA curves of GCNF-CO ₂ H and GCNF-epoxide hybrid materials.....	173
Figure 80. BET analysis of GCNF-CO ₂ H and GCNF-epoxide hybrid materials.....	174
Figure 81. Dispersibility test of GCNF-CO ₂ H in A) Toluene, B) Chloroform, C) Isopropyl alcohol, D) Methanol, E) THF, F) Ethyl acetate, G) Water, H) Acetone, I) DMF at the concentration of about 0.1 mg/mL.....	175
Figure 82. Dispersibility test of GCNF-PGE-1 in A) Toluene, B) Chloroform, C) Isopropyl alcohol, D) Methanol, E) THF, F) Ethyl acetate, G) Water, H) Acetone, I) DMF at the concentration of about 0.1 mg/mL.....	175

LIST OF SCHEMES

Scheme 1. General mechanism of an ATRP process.	16
Scheme 2. Strategy for synthesis of PBA brushes on the surface of herringbone GCNFs.....	30
Scheme 3. Strategy for synthesis of PiBMA brushes on the surface of herringbone GCNFs.	32
Scheme 4. Strategy for synthesis of PtBA brushes on the surface of herringbone GCNFs.....	34
Scheme 5. Strategy for synthesis of PGMA brushes on the surface of herringbone GCNFs.	37
Scheme 6. Synthesis of UDD/polymer brushes via surface-initiated ATRP of methacrylate monomers.....	70
Scheme 7. Strategy I for synthesis of PiBMA brushes from the surface of UDD particles.....	75
Scheme 8. Strategy II for synthesis of PiBMA from the surface of UDD particles.	77
Scheme 9. Strategy for synthesis of PtBMA from the surface of UDD particles.	79
Scheme 10. Strategy for synthesis of POMA from the surface of UDD particles.....	81
Scheme 11. Strategy for synthesis of PGMA from the surface of UDD particles.....	82
Scheme 12. Synthesis of UDD-epoxide hybrid materials	154
Scheme 13. Synthesis of GCNF-epoxide hybrid materials via ring-opening reaction.	168

CHAPTER I

INTRODUCTION

1.1. Nanocarbon Materials

Ever since the discovery of C_{60} ¹ and the following publication by Iijima of fullerene nanotubules,² nanocarbon materials have attracted tremendous attention due to their specific nanometer scale structures and unique thermal, mechanical, and electrical properties. Figure 1 shows the classification of major nanocarbon structures as nanofibers, fullerenes/nanotubes, and nanodiamonds based on the degree of C-C bond hybridization, sp^n . For carbon nanofibers, the hybridization degree is sp^2 due to the graphite structure. The hybridization degrees for fullerenes and carbon nanotubes fall between sp^2 and sp^3 according to the non-ideal C-C bonding comprising these closed-shell structures. Nanodiamonds, however, have the hybridization degree of sp^3 typical of the bulk diamond structure.³

Carbon nanotubes have been the most intensely studied nanocarbon materials since the milestone discovery of multi-walled nanotubes (MWNTs) in 1991,² and the first report of single-walled nanotubes (SWNTs) in 1993.^{4,5} A single-walled carbon nanotube is constructed by rolling up a graphite sheet to form a closed tube with the diameter ranging from 0.4 to 3 nm. As shown in Figure 2, three different types of carbon nanotube, namely zigzag (14, 0), chiral (11, 4), and armchair (8, 8), are defined by their variant

chiral vectors indices (n, m). On the other hand, MWNTs consist of a set of concentric single-walled nanotubes resulting in diameters up to 100 nm.⁶

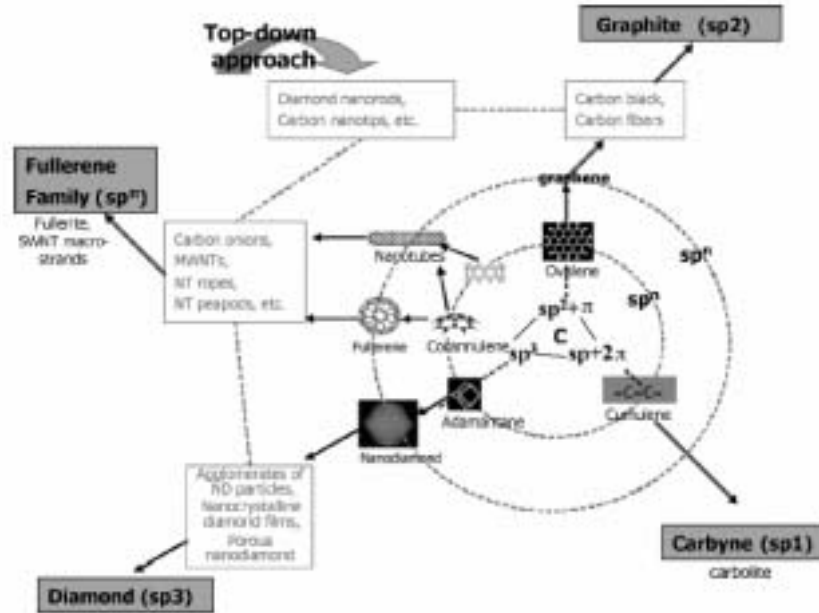


Figure 1. Classification of nanocarbon structures based on the carbon bond hybridization. (Reprinted from ref. 3. Copyright of 2002 CRC Press, Inc.)

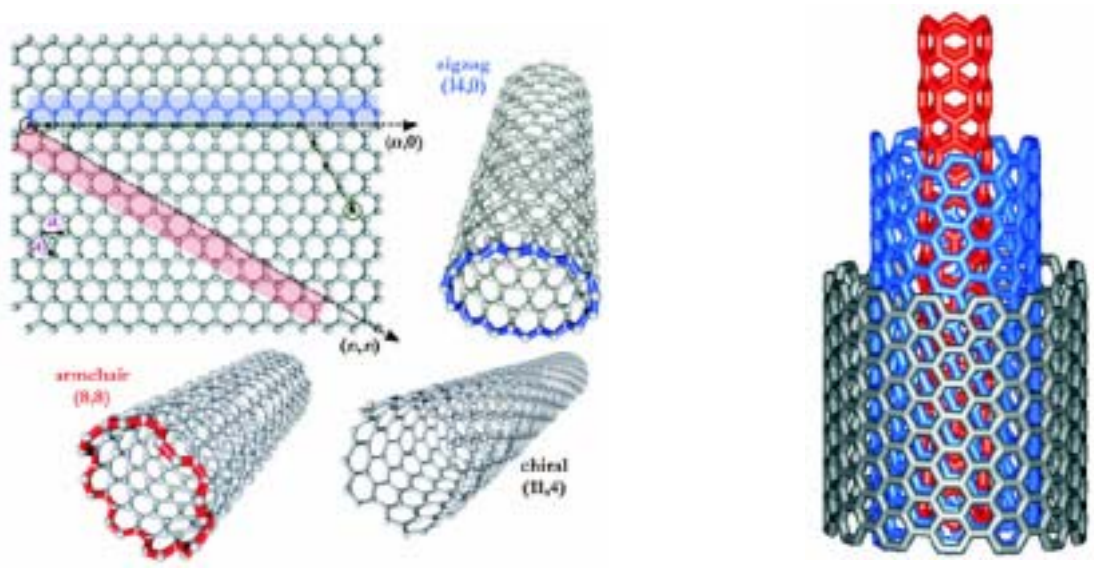


Figure 2. Three different types of SWNT (left) and MWNT constructed of three shells of different chiralities (right). (Reprinted from ref. 6. Copyright of 2005 Wiley-VCH.)

Depending on their chiralities, carbon nanotubes can be metallic or semiconducting.⁷ Because of their extraordinary properties, carbon nanotubes have been exploited in diverse applications as summarized in many review articles and books.⁷⁻¹¹

1.2. Graphitic Carbon Nanofibers

Among nanocarbon materials mentioned above, graphitic carbon nanofibers (GCNFs) may have the longest history of more than 100 years and have been actively studied in the fields of nanoscience and nanotechnology since the 1980s.¹² GCNFs are synthesized by catalytic decomposition of carbonaceous gases, such as methane, ethylene, or carbon monoxide at elevated temperatures (500 °C to 900 °C) leading to the deposition of graphite sheets on the surface of metal or alloy growth catalyst nanoparticles. A mechanism for catalytic growth of carbon nanofibers has been proposed and confirmed within the past two decades.¹²⁻¹⁵ Recently, direct observation, by *in situ* transmission electron microscope (TEM) technology, reveals the actual mechanism of carbon nanofiber growth from methane over supported nickel nanoparticles.¹⁶ In general, the following three steps are involved in the nucleation and growth of carbon nanofibers (see Figure 3): (1) hydrocarbon gaseous molecules are adsorbed and decomposed at the metal/gas interface forming carbon atoms while molecular hydrogens are desorbed, (2) the deposited carbon atoms diffuse along the surface of the metal particle as well as certain contribution from bulk diffusion and precipitate as graphite sheets at another facet(s) of the metal particle, (3) the carbon nanofiber grows by the dominating

surface-transportation of carbon atoms towards and metal atoms away from the graphite-metal interface until the metal particle becomes completely covered by graphite structures (it is remarkable that the metal particle reshapes during the growth course to generate step edges for graphite deposition).

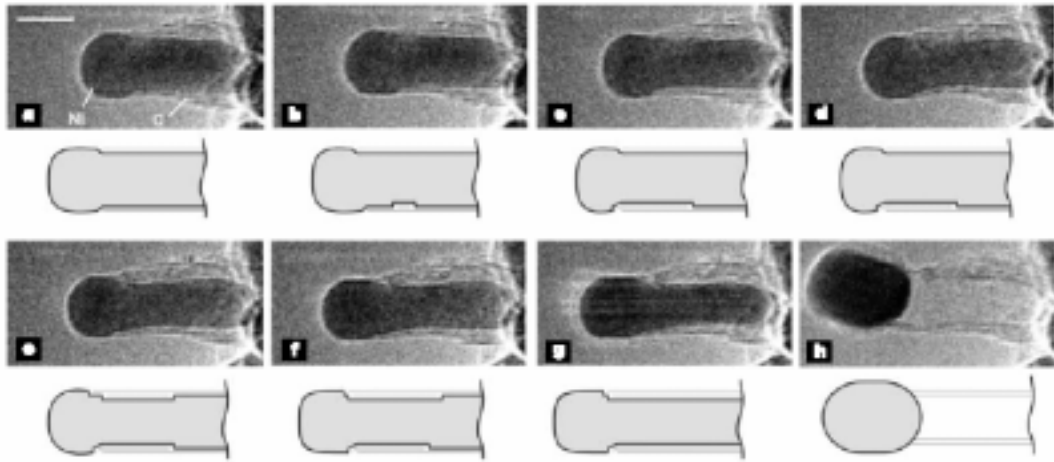


Figure 3. Schematic illustration of mechanism for the growth of a carbon nanofiber from methane catalyzed by a nickel particle via *in situ* TEM images. (Reprinted from ref. 16. Copyright of 2004 Nature Publishing Group.)

Typical average diameters diameter of GCNFs prepared by CVD methods vary from 5 nm to 500 nm, while nanofiber lengths typically range from 1-100 μm or even longer. The primary structures of GCNFs are defined by how graphite sheets stack along the nanofiber with respect to the long-axis orientation. Three fundamental types of GCNFs possessing platelet, ribbon, and herringbone structures have been reported (see Figure 4).¹⁷ For a platelet GCNF, the graphite sheets are stacked perpendicularly to the long axis of the nanofiber, ribbon GCNFs display graphite sheets stacked parallel to the long axis

of the nanofiber, and graphite sheets in herringbone GCNF are stacked obliquely with respect to the nanofiber long axis.

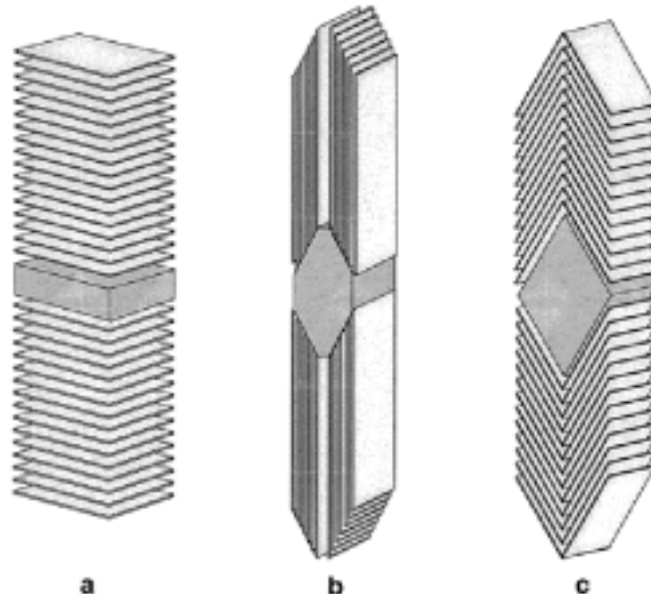


Figure 4. Primary structures of three types of graphitic carbon nanofibers with different graphitic sheets orientation: (a) platelet, (b) ribbon, (c) herringbone. (Reprinted from ref. 17. Copyright of 1997 Elsevier B. V.)

Given such unique structures, GCNFs have physical and chemical properties much different from those of conventional carbon fibers (which have diameters on the micrometer scale). Although carbon nanotubes (CNTs) possess many interesting properties among current materials, GCNFs display very similar properties, especially high tensile strength (1.5-4.8 GPa) and Young's modulus (228-724 GPa) along with low electrical resistivity (10^{-6} to 10^{-5} Ωm).¹⁸ Most importantly, the unique graphite sheets stacking in GCNFs, specifically in platelet and herringbone GCNFs, provides 12

unsaturated edge carbon atoms in a 1 nm^2 ideal sheet. Such a high number density of C edge sites is a great advantage from the surface chemistry point of view, as surface derivatization of these surface sites can render GCNFs amenable to a wide range of materials applications.

Based on their one dimensional nanoscale structures and excellent electronic and mechanical properties, GCNFs have found extensive applications in four major areas: electronic components and devices, hydrogen storage media, catalyst substrates, and nanocomposite materials.

With a field emission threshold between 15 and 50 $\text{V}/\mu\text{m}$, individual GCNFs have been found to be good field emitters.¹⁸ For example, vertically aligned carbon nanofibers grown from a flat silicon surface have been used in field emission devices to achieve desirable field emission characteristics, high apparent field enhancement factor, and high emission site density.¹⁹ Specially prepared GCNFs exhibiting a specific capacitance of 27 F/g may find application as supercapacitors.²⁰

Driven by the hydrogen storage benchmark of 6.5 wt% and 62 kg/m^3 from the U.S. Department of Energy (DOE), GCNFs have been investigated as promising hydrogen storage media due to their large specific surface area. Rodriguez, et. al.,²¹ reported that the platelet GCNFs of 3-50 nm in diameter were capable of absorbing and storing 20 L of hydrogen gas per gram of GCNFs under the pressure of 120 atm at room temperature. They suggest that the ultra-high uptake of hydrogen was related to the spacing between the platelet graphite sheets of 3.37 Å. However, Tibbetts, et. al.,²² reported less than 0.1

wt% hydrogen sorption for herringbone GCNFs at room temperature and 3.5 MPa pressure, and Ahn, et. al.,²³ also claimed limited hydrogen storage to herringbone GCNFs (less than 0.2 wt% at room temperature). It has been suggested that parameters such as pressure, temperature, and nanostructures have to be carefully adjusted to achieve a large volume of hydrogen storage by GCNF materials.²⁴

Applications using GCNFs as catalyst supports have been reviewed by Serp, et al.²⁵ To achieve desirable improvement on catalysis performance, two approaches are used to anchor metallic catalysts on the surface of GCNFs: (1) metal or alloy nanoparticles, such as nickel, rhodium, platinum, and platinum-ruthenium alloy nanoparticles, have been deposited or formed directly on different types of GCNFs by Baker²⁶⁻²⁹ and our group,³⁰⁻³² (2) organometallic complexes have been chemically immobilized on the surface of GCNFs through surface binding by Koningsberger, et. al.³³

GCNFs have been introduced into various matrices as reinforcement additives to prepare nanocomposites with enhanced properties. GCNF/ceramic nanocomposites with enhanced mechanical and electrical properties have been reported by our group^{34,35} and by Hirota, et. al.,³⁶ using silica or Al₂O₃ as matrix ceramics, respectively. Extensive studies have been devoted to GCNF/polymer composites for both thermoplastic and thermosetting polymer resins. Tibbetts, et. al.,^{37,38} fabricated GCNF/polypropylene composites with triple the modulus and tensile strength of pure polypropylene resin. Zeng and co-workers³⁹ reported that the GCNF/PMMA composites with 5 wt% GCNFs display 50 % improvement of tensile strength. Lafdi and Matzek⁴⁰ published a study of

GCNF/epoxy composites having a three-fold increase in modulus. Lozano, et. al.,⁴¹ studied the electrical conductivity of GCNF/polypropylene composites and suggested a critical transition of volume resistance occurring in the region of 9 wt% to 18 wt% carbon nanofiber loading.

1.3. Ultradispersed Diamond

Ultradispersed diamond (UDD) is one form of nanodiamond material.^{3,42} The family of nanodiamond materials consists of a variety of structures, such as diamond nanocrystals found in interstellar dust and meteorites, diamond nanoparticles nucleated from gas phase reaction and nanocrystalline diamond films. These nanodiamond materials are synthesized by diverse methods and possess different structures and purity degrees.

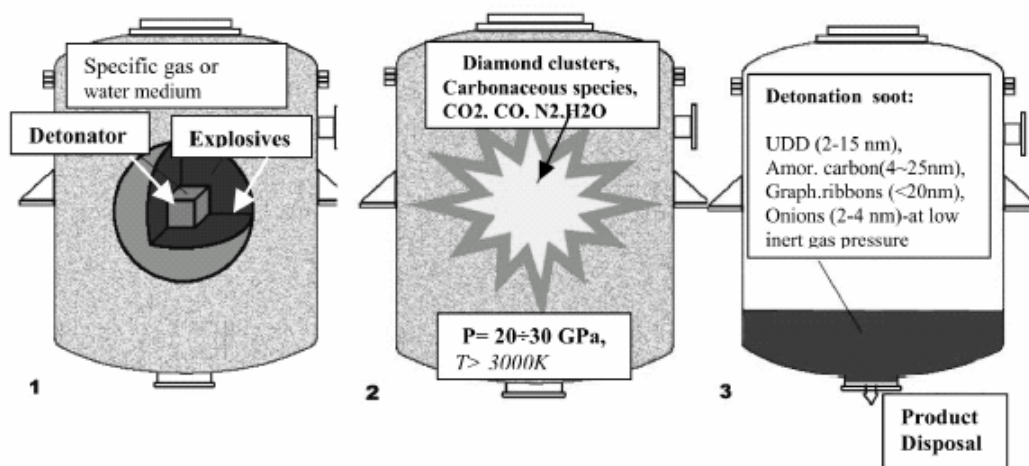


Figure 5. Schematic illustration of the controlled detonation synthesis of nanodiamond from carbon containing explosives. (Reprinted from ref. 3. Copyright of 2002 Marcel Dekker, Inc.)

There are three major commercial methods for synthesis of ultradispersed diamond (UDD): the first one is the “Du Pont method”, in which diamond nanoparticles are transformed from encapsulated carbon precursors by an external shockwave (~ 140 GPa), the second method involves detonation of a mixture of carbon-containing materials, such as graphite, coal, and carbon black, with explosives in air or an inert atmosphere; and the third method employs the same detonation technology except that only carbon-containing explosives are used as precursors.^{3,42} The general process of this last method for UDD synthesis is illustrated in Figure 5. Carbon-containing explosives, typically a mixture of TNT and hexogen, are placed in a pressure-resistant cylindrical reactor with either inert gas or water as coolant. Following ignition, a detonation wave generates high pressure (20-30 GPa) and high temperature (3000-4000 K) that correspond to conditions for thermodynamically stable diamond. The detonation soot consists of 40-80 wt% of diamond structures depending on specified detonation conditions. The UDD nanocrystals in the detonation soot have complicated structures consisting of a diamond core of 4-6 nm in diameter enwrapped in a graphitic shell of onion-like carbon layers or graphitic nanoplatelets (see Figure 6).⁴³ Purification of UDD is performed by subjecting the detonation soot to thermal oxidation with nitric acid under elevated pressure and temperature to remove metal oxide impurities and any free graphitic carbon particles. However, it is practically impossible to etch away all of the graphitic shell of onion-like carbon structures because of the tight bonding between this

shell and the diamond core. Typical purified UDD powders contain 80-90 wt% carbon (with 90-97 % carbon atoms in the form of diamond), 2-3 wt% nitrogen, 0.5-1.5 wt% hydrogen, and ~10 wt% oxygen.

UDD nanocrystals of 4-6 nm in diameter possess unique properties (see Table 1). However, these nanocrystals tend to form primary particles of 20-50 nm in size to minimize surface energy and larger secondary agglomerates up to 1000 nm in diameter. The secondary agglomerates can be easily broken down by mechanical means, while the primary particles are stable in UDD powders. Therefore, the properties of UDD are understood more as collective properties of UDD particles rather than those of individual UDD nanocrystals.

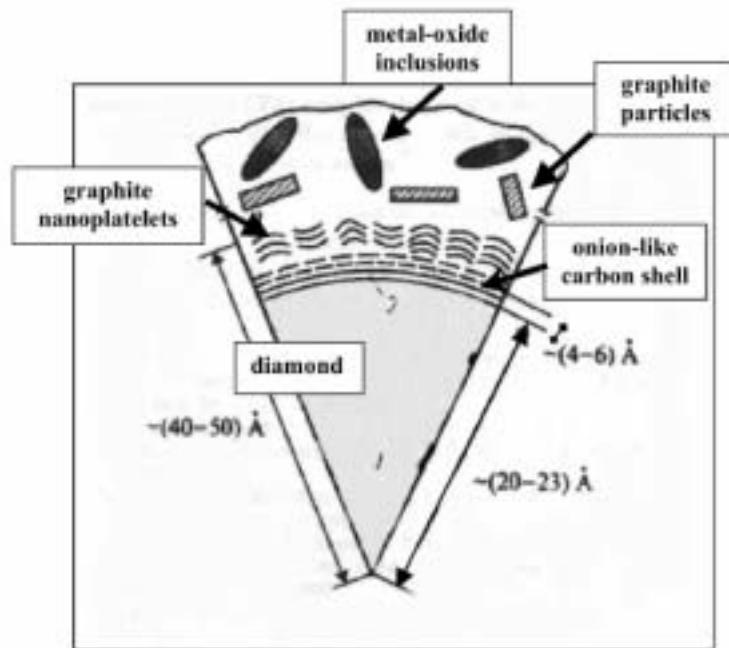


Figure 6. Schematic illustration of the structures of a primary UDD particle in detonation soot. (Reprinted from ref. 43. Copyright of 1999 American Institute of Physics.)

Table 1. Selected properties of ultradispersed diamond nanocrystals. (Reprinted from ref. 3. Copyright of 2002 Marcel Dekker, Inc.)

Structure	Cubic ($a=0.3573 \pm 0.0005$ nm)
Density	3.30 g/cm ³
Particle size	2-20 nm
Average monocrystal size	4,3 nm
Size of uncrushable aggregates	20-50 nm
Specific surface area	300 - 400 m ² /g
Pore volume in powder	0.3-1 sm ³ /g
Density of dislocations	$1,8 \cdot 10^{17}$
Composition (at. %)	C (93.2-100); O (0-6.8)
Initial air oxidation temperature (depends on purity)	430 ⁰ C
Initial vacuum graphitization temperature	1100-1200 ⁰ C
Resistivity	$7,7 \cdot 10^9$ Ωm
Electrophoretic surface charge	-78.44 mV
Refractive index	-2.55 (at $\lambda=580$ nm)

Possessing specific mechanical, electrical, thermoconductive, and surface properties, UDD particles have been used for a variety of applications. UDD particles were added into galvanic coatings by electrochemical deposition to improve wear-resistance, microhardness, and corrosion resistance of these coatings.³ Addition of UDD particles in lubricating oils, greases, and lubricant coolants can increase the service life of motors and transmissions by reducing the friction torque and wear of rubbed surfaces.³ UDD particles can also be applied in magnetic media to improve the properties of magnetic recording devices due to their unique magnetic properties.⁴⁴ Nesterenko, et. al.,^{45,46}

recently reported using microdispersed sintered UDD particles as a new stationary phase for HPLC columns with much improved separation performance. Application of UDD particles in biological areas has been studied as fluorescent cellular biomarkers,^{47,48} artificial bone additives in tissue engineering,⁴⁹ and drug delivery and diagnostics materials by incorporating with peptides.⁵⁰ UDD particles have attracted growing attention as a nanoscale reinforcement material for composite materials. Livramento, et. al.,⁵¹ published the preparation of UDD/copper nanocomposites with substantial hardness increment. UDD/polymer composites have been prepared to provide enhancement in mechanical strength, wear-resistance, and heat-aging resistance.^{3,52}

1.4. Surface Chemistry of Nanocarbon Materials

Lack of solubility in common organic solvents and water is a huge obstacle for the application of carbon nanotubes in many areas requiring wet chemistry. Both non-covalent and covalent approaches have been intensively exploited to modify the surface of CNTs for specific applications.^{6,53} Refluxing CNTs with strong oxidative acids such as sulfuric acid and nitric acid has been confirmed an effective method to modify the CNTs surface by introducing oxygen containing groups, especially carboxyl groups, at the ends and defect sites of CNTs.^{54,55} Further reactions through surface-bound carboxyl groups have enable attachment of a wide range of functional moieties, such as dendrimers, DNAs, proteins, or metal nanoparticles, to CNTs.⁵³

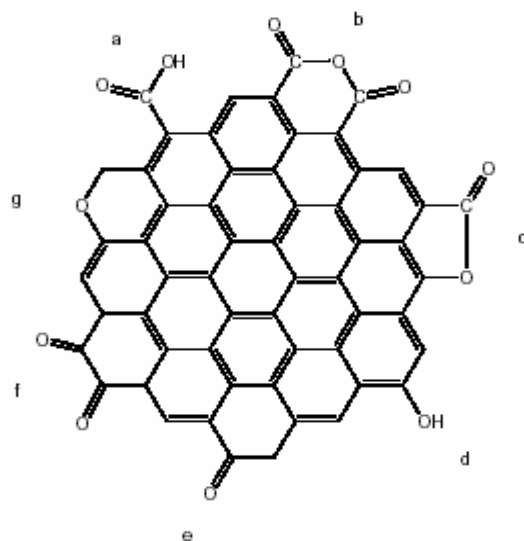


Figure 7. Oxygen-containing groups a) carboxyl, b) carboxy anhydride, c) lactone, d) phenol, e) carbonyl, f) quinone, and g) ether groups at the edge of a graphite plane. (Reprinted from ref. 56. Copyright of 2002 Wiley-VCH.)

Similarly, various surface treatment methods, such as oxidative treatment,⁵⁶⁻⁵⁸ CO₂ etching,³⁷ and plasma coating,⁵⁹ have been used to introduce oxygen atoms on the surface of GCNFs for further chemical functionalization. Among these different techniques, nitric acid treatment is the most common and effective method to achieve controllable surface oxidation of GCNFs. Due to the specific orientations of graphite sheets in GCNFs, as illustrated in Figure 7, chemical oxidation occurs at the edge sites of individual graphene planes and results in the formation of various functional groups, while carboxyl groups generally predominate due to the strong oxidative conditions.⁵⁶⁻⁵⁸

Following the nitric acid oxidation method, our group reported surface-functionalized GCNFs with pendant primary amino groups by immobilizing diamine or triamine molecules on the surface of GCNFs.⁶⁰ Surface-bound carboxyl groups generated by surface oxidation of GCNFs with concentrated nitric acid are converted to more reactive

acyl chloride groups through acylation reaction with thionyl chloride. Then diamine or triamine molecules are reacted with these acyl chloride groups to immobilize pendant primary amino groups as surface-bound linker molecules.

Although commercial available ultradispersed diamond powders are purified by nitric acid oxidation in the production process, additional oxidation by ozone oxidation⁶¹ and heat treatment in air^{62,63} have also been carried out for the purpose of chemical modification of the UDD surface. The surface chemistry of UDD has been extensively studied using various characterization techniques. Maslakov and coworkers⁶⁴ investigated the chemical state of the carbon atoms on UDD surface by Auger electron spectroscopy and revealed that the surface carbon atoms of UDD have the same chemical state as those in graphite, due to the graphitic shell surrounding the diamond core. Kulakova⁶⁵ systematically studied the surface chemistry of UDD and suggested that surface-bound functional groups, such as carboxyl, lactone, anhydride, and carbonyl groups, play an important role in UDD surface chemistry.

1.5. Atom Transfer Radical Polymerization for Surface Functionalization

Since the first reports of atom transfer radical polymerization (ATRP),^{66,67} this controlled/living polymerization technique has been boosted in the past years. A typical ATRP system consists of an initiator, a reductive metal halide complexed with a ligand, monomers, and solvents if necessary. Although other systems using transition metals, such as Ni(II), Ru(II), and Fe(II), have been developed, copper-based ATRP systems are

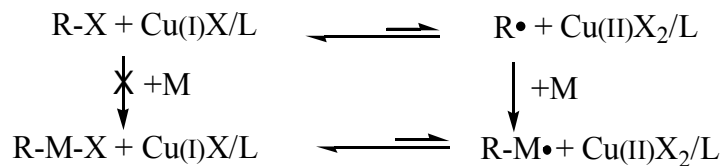
the most well-studied in both mechanism and application aspects.

The presence of radicals rather than ionic intermediates in the ATRP process has been confirmed by the experimental results of radical trapping, regioselectivity, and stereoselectivity of the polymerization.^{66,68} To perform a successful controlled/living radical polymerization, several intrinsic requirements have to be fulfilled in a ATRP process:

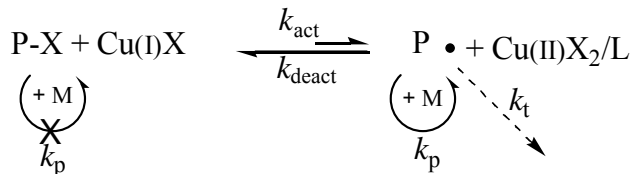
1. Initiators should be consumed at the very early stage to generate a constant number of propagating chains during the polymerization process.
2. In order to obtain low polydispersity, the number of repeating monomer molecules added to the propagating chains should be small during each activation step.
3. Termination and chain transfer reactions should be negligible to maintain the controlled/living feature.

The equations in Scheme 1 represent a general mechanism of a classic ATRP process under ideal conditions. Halogen atom X transfers from an organic halide initiator RX to a copper complex, activating the organic radical of R·, which is then quickly deactivated by backtransfer of the halogen atom X from the copper complex due to the dominant rate constant of deactivation over activation. The equilibrium of activation and deactivation is the key feature to keep constant low concentration of active radicals and consequently to ensure controlled propagation during the polymerization course.

Initiation



Propagation



Scheme 1. General mechanism of an ATRP process.

Given that termination is diminished in ATRP as a result of persistent radical effect^{69,70} and the concentration of propagating chains keeps constant during the polymerization, the kinetic polymerization rate of ATRP can be expressed as:

$$R_p = k_p \cdot K_{\theta} \cdot [M] \cdot [P-X] \frac{[\text{Cu(I)X}]}{[\text{Cu(II)X}_2]}$$

where k_p is the propagation rate constant, $K_{\theta} = k_{\text{act}}/k_{\text{deact}}$ is the equilibrium coefficient between the active and dormant chains ($k_{\text{act}} \ll k_{\text{deact}}$), $[M]$ is the concentration of monomer, $[P-X]$ is the concentration of dormant polymer chains which equals to the concentration of initiator, $[\text{Cu(I)X}]$ is the concentration of copper(I) complex, and $[\text{Cu(II)X}_2]$ is the copper(II) complex concentration. This equation predicts that the polymerization rate is first order respect to the concentration of monomer M , initiator RX ,

and the ratio of copper(I) complex over copper(II) complex. Since the deactivator Cu(II)X_2 accumulates as a persistent radical at the early stage of polymerization, the loss of a certain amount of Cu(I)X as activator is unavoidable. Although the molecular weight defined as $DP = ([M]_0 - [M]) / [RX]_0$ only relies on monomer conversion and initiator concentration, a sufficient concentration of deactivator Cu(II)X_2 is required to execute the controlled/living polymerization. To minimize the termination of propagating polymer chains, a small amount of Cu(II)X_2 respect to Cu(I)X compound can be added initially to the polymerization system, whereas the ratio of Cu(II)/Cu(I) varies in different ATRP systems.

As one of the controlled/living radical polymerization techniques, ATRP has a great advantage that all of its reagents are commercially available.⁷¹ ATRP has been applied successfully to perform the polymerization of a variety of monomers such as styrenes, acrylates, methacrylates, acrylonitrile, isoprene, and acrylamide. Two classes of commercial molecules, α -haloesters and benzyl halides, are the most used initiators in ATRP. Commonly employed ligands are bidentate bipyridines and multidentate aliphatic tertiary amines. Copper halides are used as catalysts more often than other transition metal salts or complexes. Moreover, many common solvents such as benzene, toluene, halobenzene, diphenyl ester, ethylene carbonate, acetonitrile, DMF, and even water can be used in ATRP based on different monomers and ligands involved.

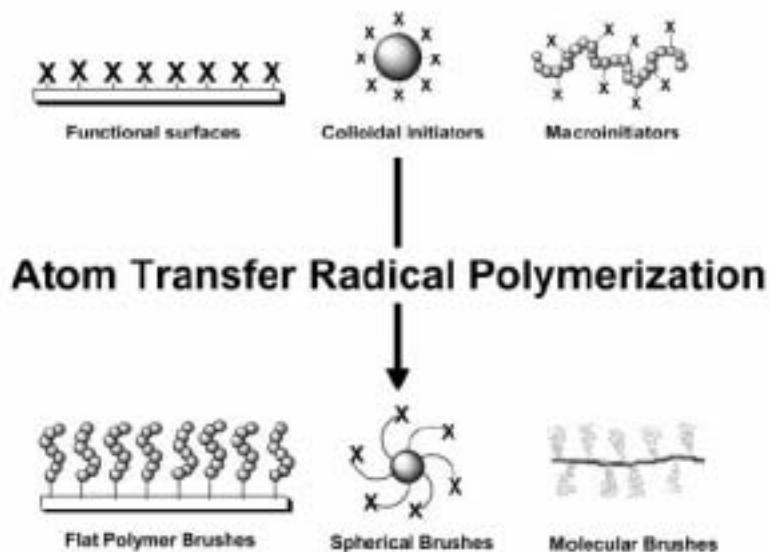


Figure 8. Examples of polymer brushes synthesized by ATRP using “grafting from” approach from various substrates of flat wafers, particles, colloids and polymers. (Reprinted from ref. 79. Copyright of 2003 Wiley-VCH.)

Polymer brushes have attracted much attention as an effective surface modification method to tailor surface properties such as dispersibility, wettability, biocompatibility, and surface functionality.⁷² With the advantage of readily controlling thickness and properties of polymer brushes, ATRP has been widely employed in the preparation of tethered polymer brushes on the surface of various substrates such as silicon wafers,⁷³ metal plates,⁷⁴ metal oxide nanowires,⁷⁵ inorganic particles,⁷⁶⁻⁷⁸ and organic latex (see Figure 8).⁷⁹ A “grafting from” strategy is applied in the synthesis of polymer brushes on the surface of substrates. ATRP initiators are firstly chemically immobilized to the surface through surface chemistries, and *in situ* polymerization of selected monomers is initiated by surface-bound initiators, resulting in tethered polymer chains on the desired substrate surface.

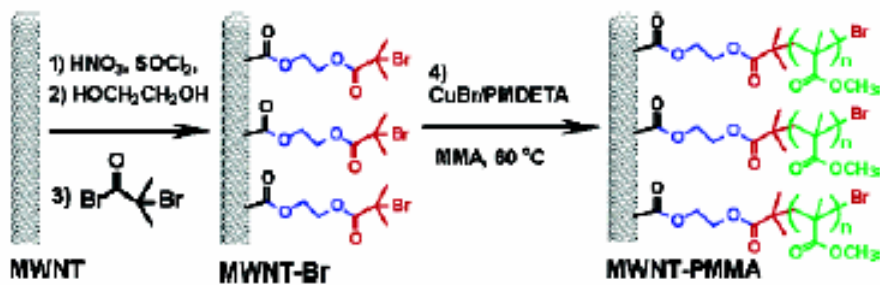


Figure 9. Synthesis of polymer brushes on MWNTs via a “grafting from” ATRP strategy. (Reprinted from ref. 82. Copyright of 2004 American Chemical Society.)

Recently, independent seminal studies on preparation of polymer brushes on multi-walled and single-walled carbon nanotubes have been contemporaneously published by four research groups.⁸⁰⁻⁸³ As demonstrated in Figure 9, the same strategy involving *in situ* ATRP from the surface of carbon nanotubes is applied in each of the four papers: surface-functionalization of carbon nanotubes with α -haloesters as ATRP initiators through surface-bound carboxyl groups induced by sulfuric/nitric acid oxidation, followed by polymerization of (meth)acrylate monomers via a “grafting from” ATRP process. Controllable thickness of the polymer brush layers is obtained by adjustment of the ATRP conditions. Solubility of carbon nanotubes in a variety of organic solvents is dramatically enhanced in the presence of poly(meth)acrylate brushes and water soluble carbon nanotubes can be achieved by the hydrolysis of hydrophobic poly(tert-butyl acrylate) brushes to give hydrophilic poly(acrylic acid) brushes. Moreover, according to Kong, et. al.⁸⁴ and Baskaran, et. al.,⁸³ polymer brushes can be further

extended by ATRP of other monomers to form amphiphilic block polymer brushes on the surface of carbon nanotubes, indicating that the controlled/living feature of ATRP is retained in the polymerization process.

1.6. Dissertation Overview

Our group has successfully achieved surface-functionalization of GCNFs with small organic linker molecules which exhibit enhanced dispersion properties.^{35,60} However, for bulk-scale applications utilizing GCNFs as reinforcement additives in polymer composites, the dispersibility of small-linker-molecules surface-functionalized GCNFs needs to be significantly improved to achieve uniform dispersion of GCNFs in polymer matrices. Similarly, the limited dispersibility of UDD particles in solvents and polymer matrices is still a major hindrance for preparation of stable lubricant suspensions and fabrication of polymeric nanocomposites. Therefore, a new strategy for surface-functionalization of GCNF nanofibers and UDD particles to manipulate their dispersion properties is highly desirable. Since GCNF nanofibers and UDD particles have the same surface oxidation chemistry as CNTs, polymer brushes could also be grown from the surface of GCNF nanofibers and UDD particles via surface-initiated ATRP of (meth)acrylate monomers. In this work, the “grafting from” strategy has been successfully employed for synthesis of organic polymers from the surface of GCNF nanofibers and UDD particles via a known *in situ* polymerization technique. These new GCNF/ or UDD/polymer brush materials have been used as gas sensors and as covalently

integrated additives in polymeric nanocomposites.

The first syntheses of herringbone GCNF/polymer brushes by atom transfer radical polymerization are reported in Chapter II. Using the “grafting from” synthesis strategy, polymerization of (meth)acrylate monomers occurs at surface sites covalently derivatized with ATRP initiators to form GCNF-poly(*n*-butyl acrylate), GCNF-poly(*iso*-butyl methacrylate), GCNF-poly(*tert*-butyl acrylate), and GCNF-poly(glycidyl methacrylate) polymer brushes. Acid hydrolysis of the GCNF-poly(*tert*-butyl acrylate) polymer brush gives a GCNF-poly(acrylic acid) polymer brush. Structures of these GCNF/polymer brushes are confirmed by microscopic, analytical, and spectroscopic characterizations. Solution dispersibilities of GCNF/polymer brushes are determined by the solubility properties of the polymer brush component, with GCNF-poly(meth)acrylate brushes being hydrophobic, whereas the GCNF-poly(acrylic acid) brush is hydrophilic. Because of the unique atomic structure of herringbone GCNF nanofibers, a high surface density of ca. 3 polymer chains/10 nm² on GCNF is achieved.

In Chapter III, UDD/polymer brushes having excellent solution dispersibilities are prepared by ATRP using the same “grafting-from” synthesis strategy. ATRP initiators, covalently attached to oxidized surface carbon atoms of UDD particles, initiate polymerization of methacrylate monomers to form hydrophobic UDD-poly(*iso*-butyl methacrylate), UDD-poly(*tert*-butyl methacrylate), UDD-poly(octodecyl methacrylate), and UDD-poly(glycidyl methacrylate) polymer brushes. Acid hydrolysis of a UDD-poly(*tert*-butyl methacrylate) polymer brush affords a hydrophilic UDD-poly(methacrylic acid) polymer brush. Based on surface area measurements and

GPC data, the calculated surface density of a representative UDD/polymer brush material is ca. 5 polymer chains/100 nm². A wide variety of UDD/polymer brush materials having controlled dispersibility and functional group reactivity are now potentially available using this synthesis strategy.

GCNF/polymer hybrid materials can be used as chemical and biological sensors and the application as chemical gas sensors is demonstrated in Chapter IV. Carbon nanofiber/interdigitated array circuits fabricated with as-prepared herringbone GCNF nanofibers, GCNF nanofibers surface-derivatized with 3, 4'-oxydianiline functional groups (GCNF-ODA), and GCNF-poly(*n*-butyl acrylate) or GCNF-poly(acrylic acid) polymer brushes are evaluated as solid-state gas sensing materials unsupported by a polymer matrix. Analyte vapor detection is observed as an increase in circuit electrical resistance. Analyte chemoselectivities and response times are reported. Maximum response sensitivities range over three orders of magnitude and parallel expected trends in relative degree of vapor/GCNF van der Waals interaction.

Chapter V reports the fabrication of epoxy/nanocarbon nanocomposites by covalently incorporating UDD-PGMA polymer brushes and reactivated GCNF-ODA nanofibers in epoxy matrices. Uniform dispersion of UDD-PGMA in epoxy has been achieved given that PGMA polymer brushes not only enhance the dispersibility of UDD particles but also crosslink with epoxy matrix molecules through glycidyl groups in the polymers. Up to ca. 302 % increase in hardness is obtained at ca. 13.7 wt% UDD loading, indicating a positive influence of UDD-PGMA as reinforcement additives on nanocomposites. Reactivated GCNF-ODA nanofibers are used to prepare epoxy/nanofiber nanocomposite adhesives to bond PMMA and Al specimens, respectively. About ca. 39 % improvement

in shear strength and ca. 33 % tensile strength enhancement have been achieved in PMMA-PMMA joints with epoxy/r-GCNF-ODA nanocomposite adhesives, respectively.

Surface-functionalization of UDD particles can be achieved by a one-step ring-opening reaction or polymerization of epoxides initiated by surface-bound carboxyl groups on UDD particles. Appendix A describes that UDD/epoxide hybrid materials featuring alkyl, phenyl, allyl, chlorine, methacrylic, or hydroxyl groups have been synthesized with organic content ranging from ca. 4.0 wt% to 14.4 wt% via ring-opening reaction of epoxides bearing various functional groups. Ring-opening polymerization of glycidol can be conducted to prepare UDD-Glycidol hybrid materials with surface-grafted polymer content as high as ca. 74.6 wt%.

Surface-functionalization of GCNF nanofibers is also achieved by ring-opening reaction of epoxides initiated by surface-bound carboxyl groups in the presence of tertiary amine catalysts (see Appendix B). GCNF/epoxide hybrid materials featuring various functional groups have been synthesized with organic content ranging from ca. 8.1 wt% to 13.7 wt% via ring-opening reaction of epoxides. Dispersibility of GCNF nanofibers in common solvents can be altered by desired surface-grafted linker molecules, which is important for expanding the applications of GCNF nanofibers.

CHAPTER II

SYNTHESIS OF GCNF/POLYMER BRUSHES VIA ATOM TRANSFER RADICAL POLYMERIZATION

2.1. Introduction

Herringbone GCNFs possess canted graphite sheets stacked in a nested fashion along the long fiber axis. GCNFs of this type can be prepared by catalytic CVD of carboneous gases at elevated temperature having average diameters from 25 nm–200 nm and lengths on the micron scale.¹² The graphitic atomic structure of herringbone GCNFs gives a carbon nanofiber long-axis surface comprised of C(sp²) edge sites, usually passivated by hydrogen atoms. Refluxing as-prepared herringbone GCNFs in concentrated nitric acid not only removes metallic catalyst particles and amorphous carbon impurities but oxidizes C atoms at the edge sites of graphene sheets. Surface-functionalization of herringbone GCNFs with reactive linker molecules using surface oxidation and carboxyl group coupling chemistry occurs without degradation of the structural integrity of the GCNF backbone and affords surface-derivatized GCNFs having a high surface density of functional groups.^{85,86} Covalent binding of such linker molecules to either polymer resins or ceramic condensation oligomers gives GCNF/polymer or GCNF/ceramic hybrid materials.^{35,87} An even greater complexity of functional group derivatization could be achieved by grafting organic polymers to GCNF surface sites to give GCNF/polymer brushes having tunable dispersibilities and surface reactivity. Proven by the synthesis of

hydrophobic and hydrophilic CNT/polymer brushes,⁸⁸ surface-initiated ATRP of (meth)acrylate monomers is a preferable method for growing polymer brushes from the surface of GCNFs.

This chapter reports the synthesis of herringbone GCNF/polymer brushes of GCNF-poly(*n*-butyl acrylate), GCNF-PBA, GCNF-poly(*iso*-butyl methacrylate), GCNF-PiBMA, GCNF-poly(*tert*-butyl acrylate), GCNF-PtBA, GCNF-poly(glycidyl methacrylate), GCNF-PGMA, and GCNF-poly(acrylic acid), GCNF-PAA by *in situ* ATRP using a “grafted from” approach. While GCNF-poly(meth)acrylate polymer brushes exhibit hydrophobic dispersibility, the GCNF-PAA brush is hydrophilic. A synthesis strategy amenable to the preparation of a wide variety of GCNF/polymer materials is demonstrated.

2.2. Experimental Section

Materials

Gaseous ethylene, hydrogen and helium were procured from Air Liquide Gas. 1,4-benzenedimethanol (97%), ethylene glycol (99.8%), 2-bromopropionyl bromide (97%), 2,2,2-trichloroethanol (TCE, 98%), methyl 2-bromopropionate (MBrP, 98%), CuBr (99.999%), CuCl (99.999%), N,N,N',N'',N''-pentamethyldiethylenetriamine (PMDETA, 99%), 4-dimethylaminopyridine (DMAP, 99%), and triethylamine (TEA, 99.5%) were purchased from Aldrich and used as received. *n*-Butyl acrylate (BA, Aldrich, 99%), *iso*-butyl methacrylate (iBMA, Aldrich, 99%), *tert*-butyl acrylate (tBA, Aldrich,

98%) and glycidyl methacrylate (GMA, Aldrich, 97%) were purified by passing through an alumina column and stored under N₂ at -15°C for use. Solvents were distilled before use and other reagents were used without further purification.

Instruments and Measurements

Transmission electron microscopy (TEM) was performed on a Philips CM-20T Electron Microscope operated at 200 KeV. 300 MHz ¹H-NMR spectra were recorded on a Bruker AC300 Fourier transform spectrometer, using CDCl₃ as solvent. Infrared spectra (IR) were obtained from KBr pressed pellets with an ATI Mattson Genesis Series FT-IR spectrometer. Thermogravimetric analyses (TGA) were performed on a Thermal Analysis Instruments High-Resolution TGA 2950 Thermogravimetric Analyzer. Elemental analysis was performed by Atlantic Microlab, Inc., Norcross, GA. BET surface area analysis was carried out on a NOVA 1000 High Speed Surface Area & Pore Size Analyzer using nitrogen gas as the absorbent.

Synthesis of (4-Hydroxymethyl)-Benzyl 2-Bromopropionate (HBBP)

A 500-mL round-bottomed flask was charged with 13.06 g (94.5 mmol) 1,4-benzenedimethanol, 20 mL (0.145 mol) TEA, 0.24 g (2.0 mmol) DMAP and 200 mL anhydrous THF. The solution was cooled to 0 °C and a solution of 10 mL (94.5 mmol) 2-bromopropionyl bromide dissolved into 20 mL anhydrous THF was added dropwise under nitrogen at 0 °C for 2 h. Then the reaction mixture was raised to 40 °C and stirred for 24 h. Solids were removed by suction filtration, and the THF was evaporated under

reduced pressure. The remaining solids were dissolved into 100 mL deionized water and extracted with CH_2Cl_2 for three times. The organic phase was dried over MgSO_4 overnight, and the solvent was removed by rotary evaporation. The light yellow liquid product of HBBP remained in 69.5% yield. $^1\text{H-NMR}$ (300 MHz, CDCl_3): $\delta=1.90$ ($-\text{CH}(\text{CH}_3)\text{Br}$), $\delta=4.22$ ($-\text{CH}_2\text{-OCO-}$), $\delta=4.40$ ($\text{HO-CH}_2\text{-}$), $\delta=4.73$ ($-\text{CH}(\text{CH}_3)\text{Br}$), $\delta=5.22$ ($\text{HO-CH}_2\text{-}$), $\delta=7.40$ ($-\text{CH}_2\text{-C}_6\text{H}_4\text{-CH}_2\text{-}$).

Synthesis of 2-Hydroxyethyl-2'-Bromopropionate (HEBP)

A 500-mL round-bottomed flask was charged with 62.0 g (1.00 mol) ethylene glycol, 16.0 mL (0.114 mol) TEA, and 200 mL anhydrous THF. The solution was cooled to 0 °C, and a solution of 21.6 g (0.10 mol) 2-bromopropionyl bromide dissolved into 20 mL anhydrous THF was added dropwise under nitrogen at 0°C for 2 h. Then the reaction temperature was raised to 40 °C for 24 h. Solids were removed by suction filtration, and the solvent was removed under reduced pressure. The remaining solids were dissolved into 100 mL deionized water and extracted with CH_2Cl_2 three times. The organic phase was dried over MgSO_4 overnight, and the solvent was removed by rotary evaporation. The colorless liquid product was collected by distillation under reduced pressure. Yield: 61.8%. $^1\text{H-NMR}$ (300 MHz, CDCl_3): $\delta=1.90$ ($-\text{CH}(\text{CH}_3)\text{Br}$), $\delta=4.29$ ($-\text{CH}_2\text{-OCO-}$), $\delta=3.85$ ($\text{HO-CH}_2\text{-}$), $\delta=4.53$ ($-\text{CH}(\text{CH}_3)\text{Br}$), $\delta=2.06$ ($\text{HO-CH}_2\text{-}$).

Synthesis of Herringbone GCNFs

The GCNFs with herringbone structure were grown from the Fe/Cu catalyst powder

as reported elsewhere.⁶⁰ The Fe/Cu catalyst with atomic ratio of 7:3 was prepared by co-precipitation of $\text{Fe}(\text{NO}_3)_3 \cdot 9\text{H}_2\text{O}$ and $\text{Cu}(\text{NO}_3)_2 \cdot 3\text{H}_2\text{O}$ with ammonium bicarbonate in water. The precipitate was dried at 110 °C overnight and ground to fine powder. The powder was weighed into a quartz boat placed in a tubular furnace and calcined in an air flow at 400 °C for 4 h. Then a H_2/He (1:4) flow of 250 mL/min was applied to reduce the iron/copper oxide at 500 °C for 20 h. After further reduction of the catalyst at 600 °C for 2 h, ethylene was introduced to grow GCNFs with a gas composition of $\text{C}_2\text{H}_4/\text{H}_2/\text{He}$ (4:1:1) at 600 °C for 90 min. Obtained GCNFs were cooled to room temperature under He protection.

Oxidation and Acylation of GCNFs

Surface oxidization of as-prepared GCNFs was performed in concentrated nitric acid at 140 °C for 4h. The product was filtered and washed with deionized water until $\text{pH} \approx 7$. The surface-oxidized carbon nanofibers (GCNF- CO_2H) were dried in vacuum at room temperature for 2 days to remove residual water. Then GCNF- CO_2H nanofibers were reacted with thionyl chloride at 70 °C for 24 h in the presence of a small amount of dimethylformamide (DMF). The mixture was cooled and washed with anhydrous THF under nitrogen until the supernatant liquid was clear. The black solid product of GCNF- $\text{C}(\text{O})\text{Cl}$ was dried with nitrogen flow at room temperature for further reaction.

Preparation of HBBP-Immobilized GCNFs (GCNF-HBBP-Br)

A 100-mL round-bottomed flask was charged with 0.42 g GCNF- $\text{C}(\text{O})\text{Cl}$, 8.47 g

(31.1 mmol) HBBP and 0.03 g (0.29 mmol) TEA. The mixture was allowed to react at 75 °C under N₂ protection for 144 h. The black solids were washed with methanol several times to remove excess HBBP and TEA. The product of GCNF-HBBP-Br was collected after filtration through a 0.2 μm Millipore PC membrane and dried in vacuum at room temperature.

Preparation of HEBP-Immobilized GCNFs (GCNF-HEBP-Br)

A 100-mL round-bottomed flask was charged with 0.98 g GCNF-C(O)Cl, 6.53 g HEBP and 0.047 g TEA. The mixture was allowed to react at 75 °C under the protection of N₂ for 96 h. Purification process was the same as that of GCNF-HBBP-Br.

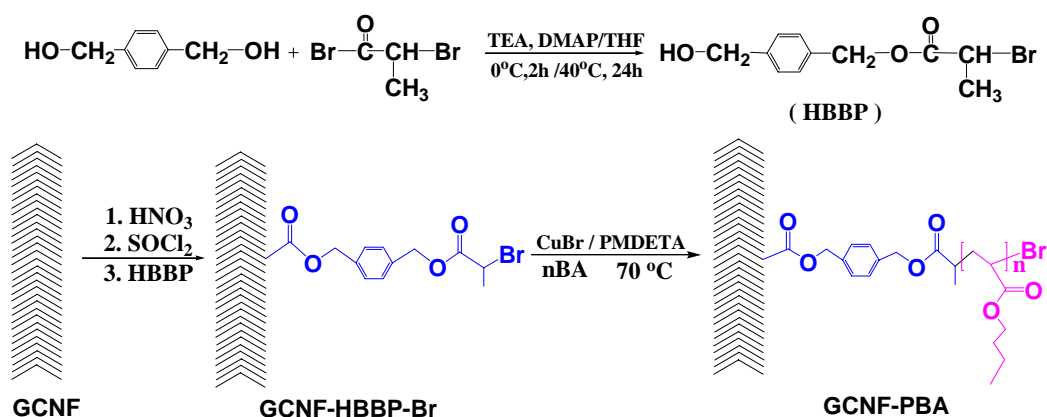
Preparation of TCE-Immobilized GCNFs (GCNF-Cl)

A 250-mL Schlenk flask was charged with 4.0 g GCNF-C(O)Cl, 20 mL TCE and 20 mL anhydrous THF, followed by adding 0.2 mL TEA. Under N₂ protection, the flask was set up with a dry condenser and put into 75 °C oil bath for 48 h. The reaction mixture was filtered through a 0.45 μm Nylon membrane, washed with methanol 4 times, and then the GCNF-Cl product was vacuum dried at room temperature overnight.

*Synthesis of GCNF-Poly(*n*-Butyl Acrylate) (GCNF-PBA)*

For a typical polymerization: a 100-mL dried Schlenk flask was charged with 200 mg GCNF-HBBP-Br, 112 mg (0.78 mmol) CuBr, 162 μL (0.78 mmol) PMDETA, and 1.00 g (7.8 mmol) *n*-butyl acrylate. The reaction mixture was degassed by five freeze-pump-thaw cycles. The flask was put into a 70 °C oil bath, and the mixture was

kept stirring for 116 h. The reaction was quenched by liquid nitrogen, and 30 mL THF was added to disperse the black solid. The product was filtered through a 0.2 μm Nylon membrane and washed with THF. The dispersion-filtration-wash process was repeated six times to ensure no un-grafted polymers remained in the residue. Then the dark solid was dispersed in methanol followed by filtration to remove catalyst reagents. The collected product was dried in vacuum at room temperature, resulting in 356 mg solid product.



Scheme 2. Strategy for synthesis of PBA brushes on the surface of herringbone GCNFs.

ATRP of n-BA in the Presence of GCNF-CO₂H

The polymerization conditions were the same as that of the ATRP of *n*-butyl acrylate except that as-prepared GCNFs were added at the ratio of *n*-butyl acrylate: GCNFs = 10:1 wt/wt. The product was purified by dispersing the resulting mixture into 30 mL THF, filtering through a 0.2 μm Nylon membrane, and washing with excess THF. The dispersion-filtration-wash process with THF was repeated six times. The filtrate was

distilled under reduced pressure and dried in vacuum at 50 °C overnight. The residual solid was washed with MeOH three times and dried in vacuum at room temperature overnight.

*ATRP of *n*-BA*

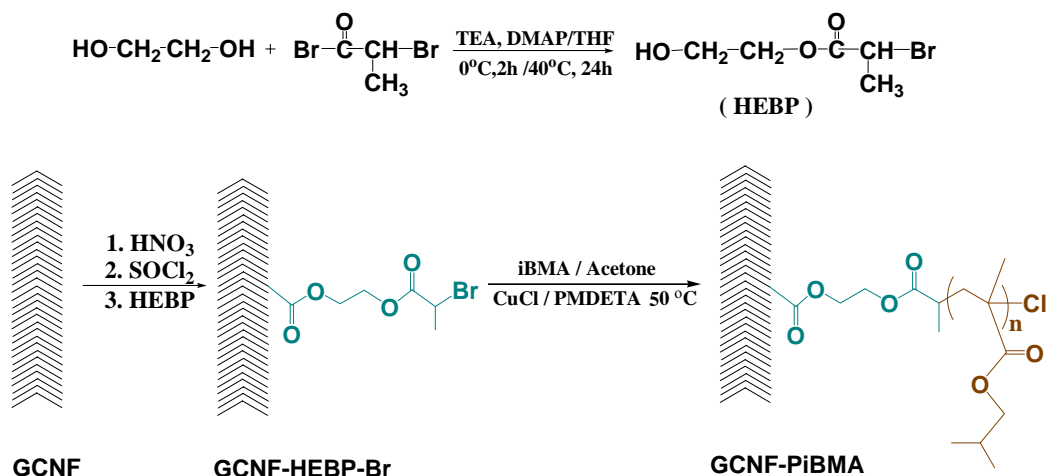
Control experiments of *n*-butyl acrylate polymerization initiated by HBBP were carried out in bulk to establish a synthesis protocol for the preparation of GCNF-PBA polymer brushes. In a typical experiment, a dry 100-mL Schlenk flask was charged with 44.8 mg CuBr (0.31 mmol), 64.9 μ L PMDETA (0.31 mmol), 85.2 mg HBBP (0.31 mmol), and 2.0 g *n*-butyl acrylate (15.6 mmol). The mixture was degassed by three freeze-pump-thaw cycles, and the flask was put into an oil bath at 70 °C for 2 h. The mixture was quenched by liquid nitrogen and then dissolved in 30 mL THF. The solution was passed through an alumina column to remove catalyst molecules. Solvent was removed by rotary evaporation under reduced pressure and the viscous liquid product of PBA was dried in vacuum at 50 °C overnight.

*Cleavage of Poly (*n*-Butyl Acrylate) from GCNF-PBA*

A typical cleavage reaction was performed by dispersing 0.1602 g GCNF-PBA3 into 100 mL toluene followed by adding 100 mL *n*-butanol and 5 mL concentrated sulfuric acid and refluxing the mixture at 100 °C for 9 days. Solvent was removed by rotary evaporation under reduced pressure. The residual solid was dispersed into 100 mL CHCl₃ and extracted with water three times to remove any sulfuric acid. The organic dispersion was filtered through a 0.2 μ m Nylon membrane and washed with CHCl₃. The filtrate was

distilled under reduced pressure to remove the solvent and dried in vacuum overnight at 40 °C. Molecular weight and polydispersity of the cleaved PBA were measured by GPC. ($M_w = 31,300$, $M_w/M_n = 1.73$)

Synthesis of GCNF-Poly(iso-Butyl Methacrylate) (GCNF-PiBMA)



Scheme 3. Strategy for synthesis of PiBMA brushes on the surface of herringbone GCNFs.

For a typical polymerization: a 25-mL dried round-bottom flask was charged with 0.20 g GCNF-HEBP-Br and 12.3 mg (0.124 mmol) CuCl. The flask was sealed with a rubber septum and degassed and refilled with nitrogen for three times. Deoxygenated acetone (4 mL) was added into the flask followed by the addition of 26 μL (0.124 mmol) PMDETA via syringe. The mixture was stirred for 10 min to form the Cu complex. After the addition of 4 mL (24.7 mmol) deoxygenated iso-butyl methacrylate via syringe, the flask was put into a 50 °C oil bath for 96 h. The reaction was quenched by liquid nitrogen and THF was added to disperse the black solid. The product was filtered through a 0.2

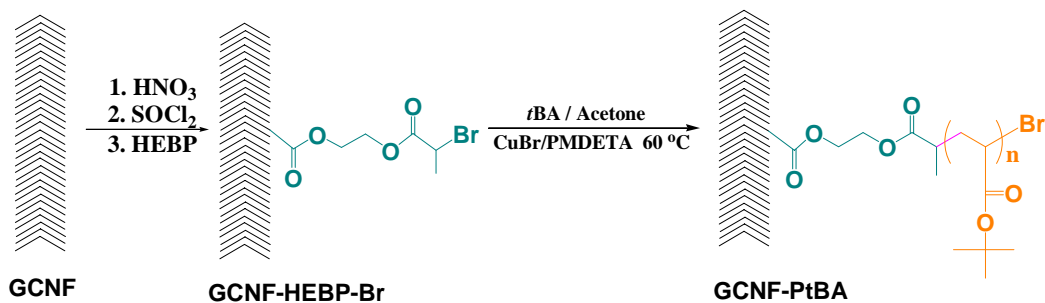
μm Nylon membrane and washed with THF. The dispersion-filtration-wash process was repeated six times to ensure no un-grafted polymers were left in the residue. Then the dark solids were dispersed in methanol followed by filtration to remove catalyst reagents. The collected product was dried in vacuum at room temperature.

ATRP of iso-BMA in the Presence of GCNF-CO₂H

A 25-mL dried round-bottom flask was charged with 0.20 g GCNF-CO₂H and 12.3 mg (0.124 mmol) CuCl. The flask was sealed with a rubber septum and degassed and refilled with nitrogen for three times. Deoxygenated acetone (4 mL) was added into the flask followed by the addition of 26 μL (0.124 mmol) PMDETA via syringe. The mixture was sonicated for 15 min to form a fine dispersion. Then 4 mL (24.7 mmol) deoxygenated *iso*-butyl methacrylate was added into the flask via syringe, and the mixture was stirred for 5 min. Finally, 30 μL (0.247 mmol) HEBP was added via syringe, and the flask was put into a 50 °C oil bath for 20 h. The reaction was quenched by liquid nitrogen, and THF was added to disperse the black solids. The product was filtered through a 0.2 μm Millipore Nylon membrane and washed with THF. The filtrate was passed through an alumina column, rotary evaporated to remove the solvent, and vacuum dried at 50 °C overnight. The solid residue was purified by repeating dispersion-filtration-wash process THF four times to ensure no un-grafted polymers were left in the residue. The collected solid was dried in vacuum at room temperature overnight.

*Synthesis of GCNF-Poly(*tert*-Butyl Acrylate) (GCNF-PtBA)*

A 25-mL dried round-bottom flask was charged with 0.20 g GCNF-HEBP-Br and 38.7 mg (0.27 mmol) CuCl. The flask was sealed with a rubber septum and degassed and refilled with nitrogen for three times. Deoxygenated acetone (4 mL) was added into the flask followed by the addition of 56.6 μ L (0.27 mmol) PMDETA via syringe. The mixture was sonicated for 15 min to form an even dispersion. After the addition of 4 mL (27 mmol) deoxygenated *tert*-butyl acrylate via syringe, the flask was put into a 60 °C oil bath for 22 h. The purification process of the product was the same as that of GCNF-PiBMA.



Scheme 4. Strategy for synthesis of PtBA brushes on the surface of herringbone GCNFs.

ATRP of t-BA in the Presence of GCNF-CO₂H

A 25-mL dried round-bottom flask was charged with 0.20 g GCNF-COOH and 38.7 mg (0.27 mmol) CuBr. The flask was sealed with a rubber septum and degassed and refilled with nitrogen for three times. Deoxygenated toluene (4 mL) was added into the flask followed by the addition of 56.6 μ L (0.27 mmol) PMDETA via syringe. The mixture was sonicated for 15 min to form an even dispersion. Then 4 mL (27 mmol) of

deoxygenated *tert*-butyl acrylate was added into the flask via syringe, and the mixture was stirred for 5 min. Finally, 30 μ L (0.27 mmol) MBrP was added via syringe, and the flask was put into a 60 °C oil bath for 22 h. The purification process of the product was the same as that of GCNF-PiBMA.

ATRP of t-BA (PtBA)

A 25-mL dried round-bottom flask was charged with 38.7 mg (0.27 mmol) CuBr. The flask was sealed with a rubber septum and degassed and refilled with nitrogen for three times. Deoxygenated acetone (4 mL) was added into the flask followed by the addition of 56.6 μ L (0.27 mmol) PMDETA via syringe. Then 4 mL (27 mmol) deoxygenated iso-butyl acrylate was added into the flask via syringe, and the mixture was stirred for 5min. Finally, 30 μ L (0.27 mmol) MBrP was added via syringe, and the flask was put into a 60 °C oil bath for 22 h. The reaction was quenched by liquid nitrogen, and acetone was added to dilute the mixture. The catalyst was absorbed by passing the solution through an alumina column, and the solvent was removed by rotary evaporation. The polymer product was dried in vacuum at 50 °C overnight.

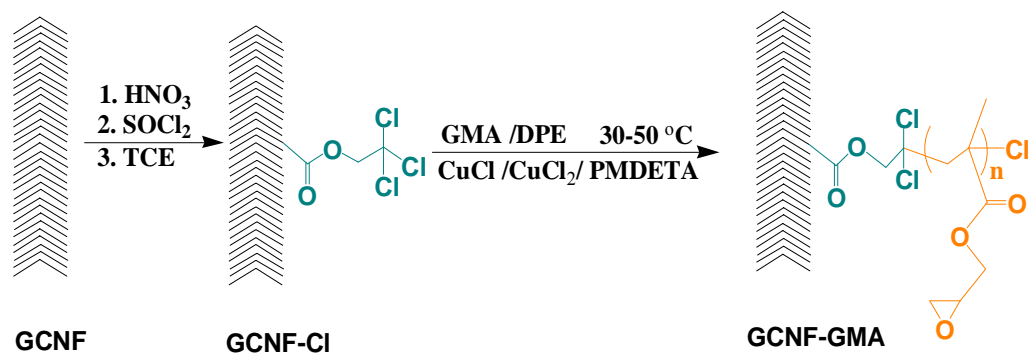
Preparation of GCNF-Poly(Acrylic Acid) (GCNF-PAA)

Hydrophilic poly(acrylic acid) brushes on the surface of GCNFs were obtained by acidic hydrolysis of PtBA chains in the GCNF-PtBA sample into PAA brushes. Typically, 50 mg of GCNF-PtBA was dispersed into 15 mL CHCl_3 in a 25-mL flask and 2.5 mL $\text{CF}_3\text{CO}_2\text{H}$ was added thereafter. The mixture was stirred at room temperature for 24 h under nitrogen protection. The reaction mixture was rotary evaporated under vacuum to

remove the reagents, and the black powder of GCNF-PAA was collected and dried in vacuum at room temperature.

Synthesis of GCNF-Poly(Glycidyl Methacrylate) (GCNF-PGMA)

A 15-mL round-bottomed flask, with a magnetic stir bar, was charged with 8.0 mg (0.060 mmol) CuCl₂ and 0.20 g GCNF-Cl. The flask was sealed with a rubber septum and degassed and refilled with N₂ three times. Deoxygenated DPE (4 mL) was added into the flask followed by three freeze-pump-thaw cycles to remove adsorbed oxygen. The mixture was sonicated 10 min to form a uniform dispersion. A 10-mL round-bottomed flask was charged with 60.0 mg (0.604 mmol) CuCl. The flask was sealed with a rubber septum and degassed and refilled with N₂ three times. 4 mL (30.2 mmol) deoxygenated GMA and 140 μL (0.664 mmol) PMDETA were added into the flask via syringe and the mixture was stirred for 15 min to form a green homogeneous solution. The monomer solution was transferred into the GCNF-Cl dispersion flask by cannula. The flask was put into room temperature water bath for 24 h. CHCl₃ was added to dilute the reaction mixture and unreacted monomers were removed by centrifuge. The solid residue was redispersed in a CHCl₃/MeOH (9/1, v/v) solvent mixture and centrifuged six times to remove ungrafted polymers and catalyst. The solid product of GCNF-PGMA was collected and dried in a vacuum oven overnight at room temperature.



Scheme 5. Strategy for synthesis of PGMA brushes on the surface of herringbone GCNFs.

2.3. Results and Discussion

Three types of GCNFs with herringbone, platelet, and ribbon structures, have been prepared by chemical vapor deposition of carbonaceous gases on metal nanoparticles.¹⁷ In this work, however, herringbone GCNFs are used to demonstrate the preparation of polymer brushes on the surface of GCNFs because: (1) herringbone GCNFs have a high number density of surface reactive sites, (2) herringbone GCNFs are prepared in higher yield than that of GCNFs with the other two structures. The herringbone GCNFs were prepared by catalytic deposition of ethylene at 600 °C using Fe/Cu alloy nanoparticles as catalyst. Surface-oxidation of as-prepared GCNFs is carried out in concentrated nitric acid to introduce reactive carboxyl groups on the GCNF surface.⁵⁶ Studies on GCNFs surface oxidation with nitric acid indicate that the structure of individual nanofibers remains intact after surface treatment. However, the BET specific surface area of oxidized nanofibers, especially herringbone GCNFs, increases significantly due to enhancement of the nanofiber surface roughness as a result of edge-site etching of

graphitic sheets which are stacked along the long nanofiber axis. Oxidized GCNFs have a specific surface area value of ca. 25.56 m²/g compared with ca. 15.31 m²/g for as-prepared GCNFs. Oxidized GCNFs have 6.6 carboxylic groups per 1000 carbon atoms based on the elemental analysis results shown in Table 2. Therefore, the number of carboxylic groups per unit surface area is ca. 1.3×10¹⁹ groups per square meter (13 groups/ nm²), which is consistent with the literature value of 2.5×10¹⁹ oxygen atoms per square meter.⁵⁶

Table 2. Elemental analysis results of GCNFs and relative materials

Element	C (wt%)	H (wt%)	O (wt%)	N (wt%)	Br (wt%)	Cl (wt%)
GCNFs	95.78	0.29	0.22	-	-	-
GCNF-CO ₂ H	91.84	0.50	7.4	0.26	-	-
GCNF-HBBP-Br	90.64	0.74	6.09	-	0.92	-
GCNF-HEBP-Br	92.89	0.45	5.98	0.18	0.50	-
GCNF-Cl	93.52	0.42	5.03	-	-	1.03

Carboxyl groups on the surface of oxidized GCNFs are converted to acyl chloride groups with SOCl₂ followed by reaction with HBBP or HEBP to immobilize ATRP initiators onto the surface of GCNFs, respectively. Elemental analysis confirms the presence of bromine atoms in GCNF-HBBP-Br nanofibers at ca. 0.92 wt%, which is

equal to ca. 3.1×10^{18} bromine atoms per square meter (3.1 Br/nm^2), whereas the surface coverage for GCNF-HEBP-Br is ca. 1.7×10^{18} bromine atoms per square meter (1.7 Br/nm^2) and for GCNF-Cl is ca. 8.0×10^{17} chlorine atoms per square meter (0.8 Cl/nm^2).

*GCNF-Poly(*n*-Butyl Acrylate) Brushes (GCNF-PBA)*

ATRP of acrylate and methacrylate monomers have been used to prepare polymer brushes on solid substrates. Liu, et al.⁸⁹ reported the first synthesis of polymer brushes on the surface of carbon black particles by *in situ* ATRP of *n*-butyl acrylate. Since carbon black particles themselves react as radical-scavenging reagents, the polymerization rate of the ATRP of *n*-butyl acrylate in the presence of unfunctionalized carbon black particles was 10 times lower than that of normal ATRP of *n*-butyl acrylate in the absence of carbon black particles. When ATRP of *n*-butyl acrylate was initiated by immobilized initiators on the surface of carbon black particles, the polymerization rate was even slower. Similar results are obtained in our experiments (see Table 3). ATRP of *n*-butyl acrylate is performed in bulk at 70° C with CuBr/PMDETA complex as catalyst. Different monomer/GCNF-HBBP-Br ratios and monomer/catalyst ratios are used to carry out the polymerization. The polymerization rate is so slow that only 35 wt% polymer content is obtained even after 263 h of reaction for GCNF-PBA4.

At the late stage of polymerization, the viscosity of the reaction mixture increases due to the interaction between polymer chains grafted from the surface of GCNFs. A similar phenomenon was observed when polymer brushes grew from the surface of carbon black

particles and carbon nanotubes.

Table 3. Conditions and results of ATRP of n-butyl acrylate initiated by GCNF-HBBP-Br.

Sample	[nBA]:[I] ^a	Catalyst Ratio ^b	Temp()	Time (h)	PBA wt% ^c
GCNF-PBA1	3400:1	200:1:1	70	168	11
GCNF-PBA2	3400:1	10:1:1	70	96	17
GCNF-PBA3	340:1	10:1:1	70	116	34
GCNF-PBA4	750:1	10:1:1	70	263	35

- a. Molarity of immobilized initiators calculated by (weight of GCNF-HBBP-Br × 0.115 mmol/g).
 b. Catalyst Ratio = [nBA] : [CuBr] : [PMDETA]. c. Obtained from TGA curves.

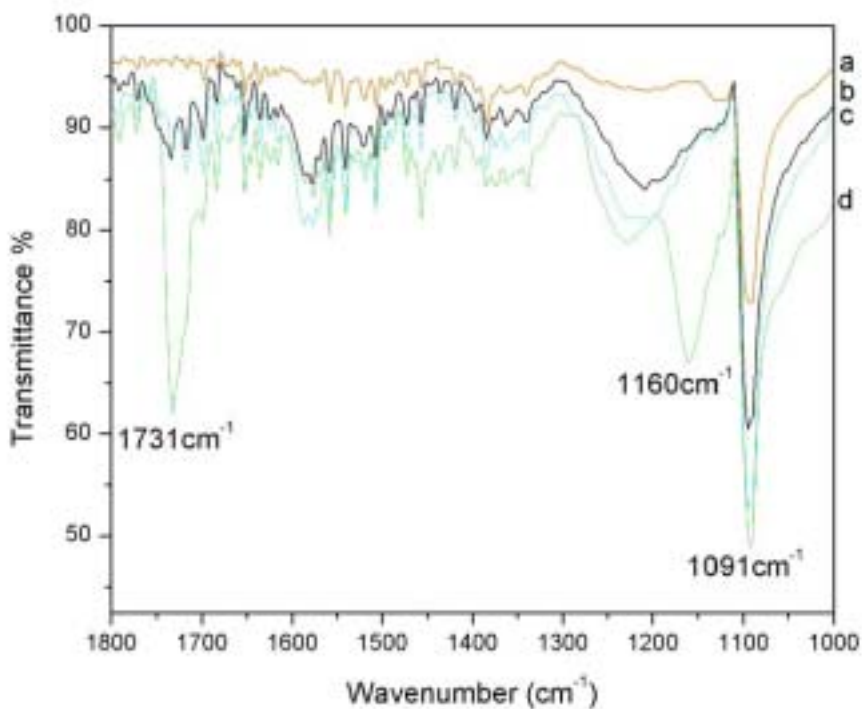


Figure 10. FT-IR spectra of (a) GCNFs, (b) GCNF-HBBP-Br, (c) GCNF-CO₂H and (d) GCNF-PBA4.

Surface-functionalization of GCNFs can be detected by FT-IR spectra recorded with KBr plates as shown in Figure 10. The characteristic bands of as-prepared GCNFs are discussed in detail elsewhere.⁵⁶ The intense 1091 cm^{-1} and broad 1217 cm^{-1} bands are assigned to the C-C stretching vibration, while the weak band at 1580 cm^{-1} is attributed to the vibration of aromatic rings in graphitic sheets. After oxidation, new bands at 1716 cm^{-1} and 1731 cm^{-1} appear in the spectrum of GCNF-CO₂H, which are assigned to the C=O stretching in the form of carboxyl and ester groups, respectively. Meanwhile, the intensity of the 1217 cm^{-1} band is greatly enhanced because C-O stretching and O-H bending bands also fall in this region. The GCNF-HBBP-Br spectrum is very similar to that of GCNF-CO₂H except that there is a slight enhancement of the 1731 cm^{-1} band, which is consistent with the elemental analysis result that only ca. 24.2% carboxyl groups have been converted to initiator molecules. Since poly(*n*-butyl acrylate) brushes have been grafted from the surface of GCNFs, characteristic absorption bands of poly(*n*-butyl acrylate) are expected to appear in the GCNF-PBA4 spectrum. Intensity of the 1731 cm^{-1} band increases significantly due to C=O stretching band and a new absorption band at 1160 cm^{-1} is clearly observed, which is associated with the C-O stretching vibration of *n*-butyl ester groups.

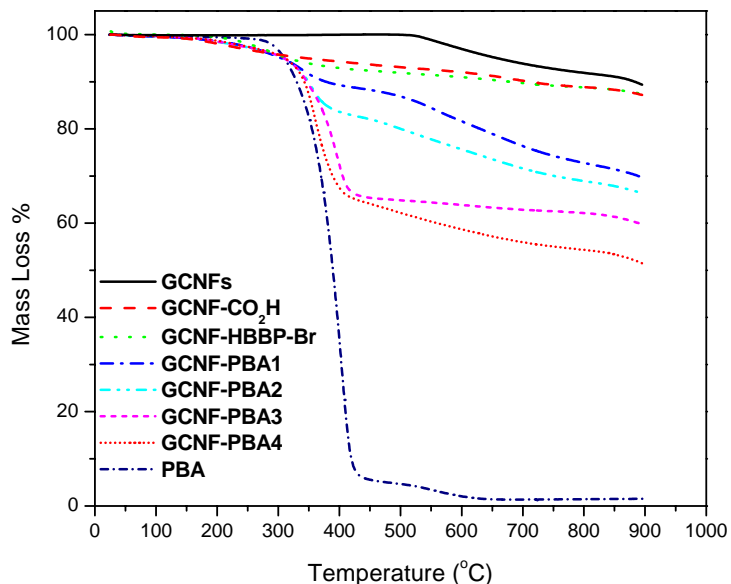


Figure 11. TGA curves of as-prepared GCNFs, surface-functionalized GCNFs, and PBA.

Figure 11 illustrates the sequential TGA curves of as-prepared GCNFs, oxidized GCNFs, initiator-immobilized GCNFs, poly(*n*-butyl acrylate) brushes-functionalized GCNFs, and pure poly(*n*-butyl acrylate), respectively. TGA analysis was carried out under a nitrogen gas atmosphere to avoid oxidation of the samples by oxygen present in air.

For as-prepared GCNFs, no mass-loss can be observed before the onset at 570 °C due to the excellent thermal stability of the tightly stacked structure of graphitic sheets in GCNFs, whereas the mass-loss of about ca. 10.6 % from 570 °C to 900 °C is attributed to the release of hydrocarbon moieties from hydrogen terminated edge-sites on GCNFs surface. Surface oxidation introduces oxygen atoms onto the surface of GCNFs by etching the edge of graphitic sheets. Surface carboxyl groups are less stable than the

aromatic rings of graphite in the thermal gravimetric analysis environment. Therefore, CO₂ and CO are gradually released when temperature increases from 150 °C to 900 °C. The GCNF-Br curve has a similar profile as that of GCNF-CO₂H because the small amount of immobilized initiator molecules in GCNF-HBBP-Br sample can result in only a slightly enhanced mass-loss.

Unlike GCNF-CO₂H and GCNF-HBBP-Br samples, the TGA curves of GCNF-PBA samples exhibit sharp mass-loss events from 330 °C to 400 °C. Rapid mass-losses in this temperature region are clearly associated with PBA polymer brushes as shown by the characteristic pure PBA mass-loss profile centered at 400 °C. Polymer content of each GCNF-PBA sample, GCNF-PBA1 – GCNF-PBA4, can thus be determined from this mass-loss event, as shown in Table 3.

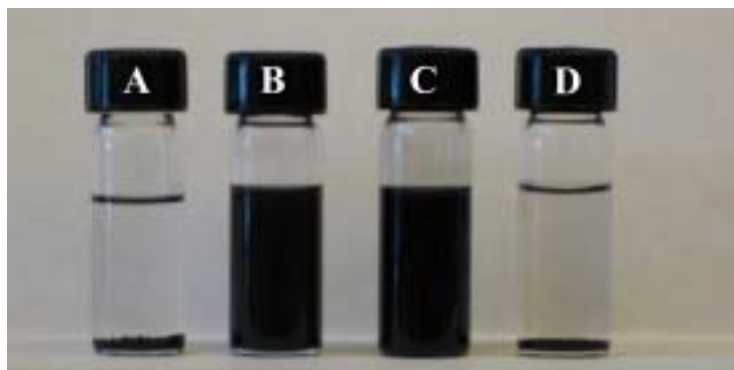


Figure 12. Dispersibility of (A) GCNF-CO₂H sample in chloroform, (B) GCNF-PBA3 sample in chloroform, (C) GCNF-PBA3 sample in toluene, (D) GCNF-PBA3 sample in methanol. Concentration of the dispersions is about 2.5 mg/mL.

When as-prepared GCNFs or oxidized GCNFs are dispersed into an organic solvent such as chloroform, THF, or acetone, they precipitate from the dispersion in less than 10 min. The dispersibility of GCNF-HBBP-Br or GCNF-HEBP-Br nanofibers in organic solvents is slightly enhanced due to the presence of surface-immobilized organic molecules, but these nanofibers also precipitate out after several hours. However, the presence of poly(*n*-butyl acrylate) brushes on the surface of GCNFs significantly improves the dispersibility of GCNF-PBA samples in common organic solvents such as THF, chloroform, and toluene (see Figure 12). When GCNF-PBA samples are dispersed into strong polar solvents such as methanol, DMF, and DMSO, which are known to be poor solvents for poly(*n*-butyl acrylate), nanofibers precipitate immediately.

Comparison of the two $^1\text{H-NMR}$ spectra shown in Figure 13 indicates the presence of poly(*n*-butyl acrylate) in GCNF-PBA3. The proton signals at 0.91 ppm, 1.34 ppm, and 1.58 ppm in the spectrum of GCNF-PBA3 are assigned to the methyl and methylene groups of the *n*-butyl side chain of the poly(*n*-butyl acrylate), respectively. Compared with the spectrum of pure PBA, intensities of signals corresponding to the backbone protons are dramatically reduced in the GCNF-PBA3 spectrum due to poor relaxation of nuclear spins of surface-bound polymer chains with restricted motions.⁹⁰

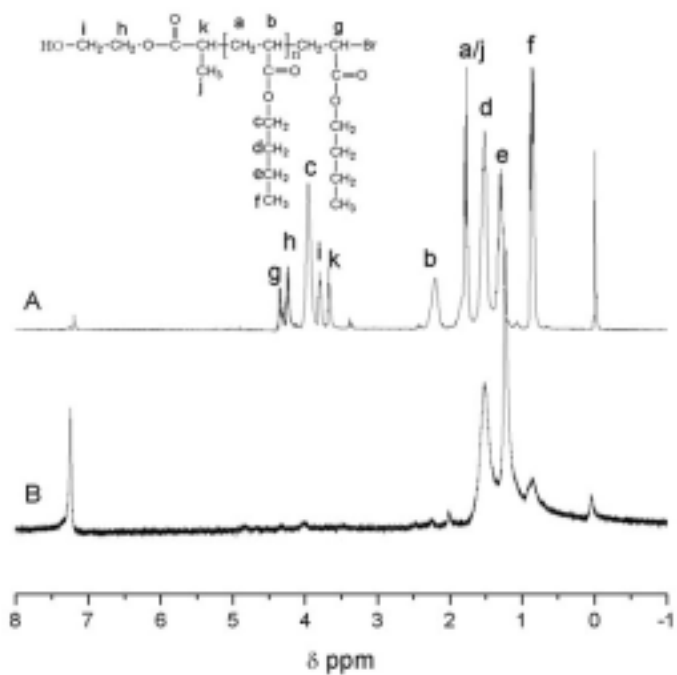


Figure 13. ¹H-NMR spectra of (A) PBA, (B) GCNF-PBA3 in CDCl₃.

Direct evidence for polymer brush formation on the surface of GCNFs comes from transmission electron microscopy (TEM) analysis. Figure 14 shows TEM images of as-prepared GCNFs and GCNF-PBA3. At lower magnification, the diameter of individual nanofibers ranges from ca. 30 nm to ca. 200 nm because of the broad size distribution of the growth catalyst Fe/Cu alloy particles.

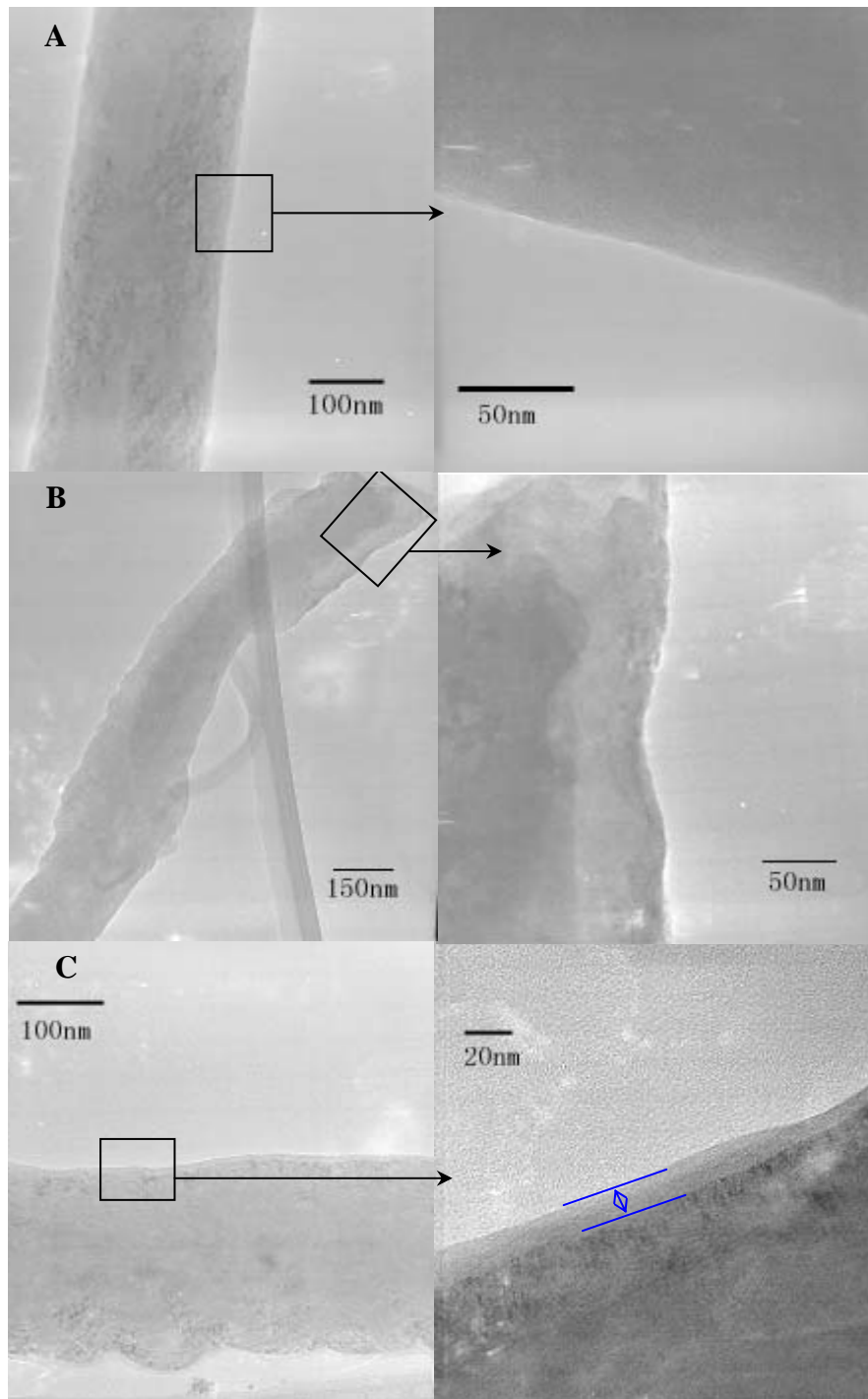


Figure 14. TEM images of (A) as-prepared GCNFs and (B), (C) GCNF-PBA3 samples.

Individual nanofibers of GCNF-PBA3, imaged in high contrast, are covered by

polymer layers of lower contrast, which are formed by the polymer brushes wrapping around the surface of nanofibers. However, polymer layer thickness varies from nanofiber to nanofiber and even along different regions of a single nanofiber. Variation in polymer layer thickness, a phenomenon not observed with carbon nanotube/polymer brushes, is caused by the rugged morphology of the surface of GCNFs.⁸⁸ During the oxidation process, defects at the edge sites of GCNFs surface are more vulnerable for oxidation attack and the local concentrations of carboxyl groups near such defective areas are expected to be higher. Consequently, a higher concentration of immobilized initiator molecules occurs near these local regions during surface derivatization. According to the mechanism of ATRP, higher initiator concentration results in higher polymerization rate. Therefore, longer polymer chains grow at these surface defect sites.

The measured molecular weight and polydispersity of PBA brushes cleaved from the surface of GCNF-PBA4 sample ($M_w=31,300$, $M_w/M_n=1.73$) are consistent with the TEM observation of polymer layers on individual GCNFs with variable thickness. Based on the BET surface area of oxidized GCNFs ($26 \text{ m}^2/\text{g}$), an average surface density of the polymer brush chains in GCNF-PBA4 polymer brushes is calculated to be ca. 3 polymer chains/ 10 nm^2 . As an ideal stacking pattern of graphene sheets contains ca. 120 unsaturated edge carbon atoms/ 10 nm^2 , ca. 1 of every 40 GCNF surface edge sites is functionalized with a polymer chain.

On the other hand, polymer brushes enwrapped on the nanofiber surface have a remarkable effect on GCNF surface morphology. As shown in Figure 15, GCNF-PBA

samples have a much smaller value of specific surface area than GCNF-CO₂H and as-prepared GCNFs, because the rugged surfaces of GCNFs are now covered by a smooth polymer layer. Moreover, the specific surface area decreases as polymer brush content increases due to this surface-smoothing effect.

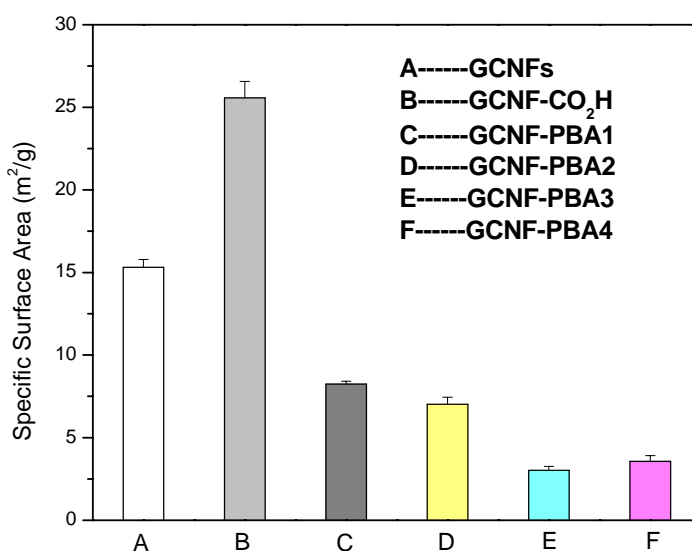


Figure 15. BET specific surface area of (A) GCNFs, (B) GCNF-CO₂H, (C) GCNF-PBA1, (D) GCNF-PBA2, (E) GCNF-PBA3, (F) GCNF-PBA4.

To prove that these polymer brush chains are covalently grafted from the surface of GCNFs by surface initiated ATRP, two control experiments were carried out. Polymerizations of *n*-butyl acrylate initiated by free HBBP initiators were performed in the presence of as-prepared GCNFs and oxidized GCNFs, respectively, under identical conditions used for bulk polymer ATRP (sample PBA0). The polymerizations were

quenched by liquid nitrogen, and the reaction mixtures were dispersed in THF, filtered, and washed with THF repeatedly. The black solids were collected and labeled as c-GCNFs and c-GCNF-CO₂H, respectively. The obtained filtrates were further purified by passing through an alumina column followed by vacuum drying to give the corresponding polymer products, PBA1 and PBA2, respectively.

Table 4. Conditions and results of ATRP of nBA initiated by HBBP.

Sample	[nBA]:[CuBr]:[PMDETA]:[HBBP]	Temp (C)	Time (h)	Mw Mn	Mw/ Mn	Yield (%)
PBA0	50:1:1:1	70	2	19,800	1.23	99.1
PBA1 ^a	50:1:1:1	70	2	13,400	1.30	58.5
PBA2 ^b	50:1:1:1	70	20	24,700	1.53	98.6

a. In the presence of as-prepared GCNFs, [BA]:[GCNFs]= 10:1 (wt/wt). b. In the presence of GCNF-CO₂H, [BA]:[GCNF-CO₂H]= 10:1 (wt/wt).

Molecular weight and polydispersity of these PBA samples obtained from GPC (see Table 4) indicate that the presence of as-prepared GCNFs or GCNF-CO₂H nanofibers had a negative effect on ATRP polymerization of *n*-BA, giving lower polymerization rates and broader polymer chain molecular weight distributions. Furthermore, TGA curves of the c-GCNFs and c-GCNF-CO₂H samples are quite different from those of as-prepared GCNFs and GCNF-CO₂H nanofibers. The c-GCNF curve has a ca. 31 %

mass-loss compared with the ca. 10.6 % mass-loss observed for as-prepared GCNFs, and similar comparison is notable for c-GCNFs and as-prepared GCNFs in Figure 16. These results indicate that some oligomer fragments are covalently attached on the nanofiber surface during the polymerization process. Because GCNFs are radical scavengers, it is unavoidable that some oligomer radicals formed at the beginning stage of ATRP process are trapped by GCNFs. However, the sharp mass-loss profile from 330 °C to 400 °C for polymer chains of PBA is not observed in neither c-GCNF nor c-GCNF-CO₂H nanofibers, indicating that without surface immobilized initiators, GCNF and GCNF-CO₂H nanofibers cannot grow polymer brushes from the surface under the same ATRP conditions.

The surface entrapment of oligomer fragments is also supported by the BET specific surface area analysis (see Figure 17). The c-GCNFs sample has a specific surface area ca. 7.75 m²/g, which is only about half of the GCNFs sample ca. 15.31 m²/g. Likewise, the c-GCNF-CO₂H sample has much less specific surface area ca. 10.55 m²/g than that of GCNF-CO₂H ca. 25.56 m²/g. This surface smoothing effect is due to the trapped oligomer fragments covering part of the nanofibers' surface.

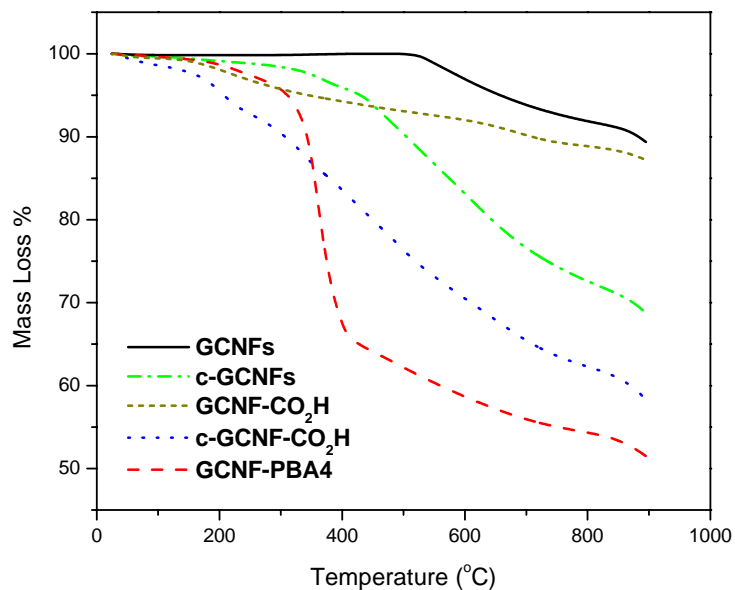


Figure 16. TGA curves of GCNFs, c-GCNFs, GCNF-CO₂H, c-GCNF-CO₂H, and GCNF-PBA4 samples.

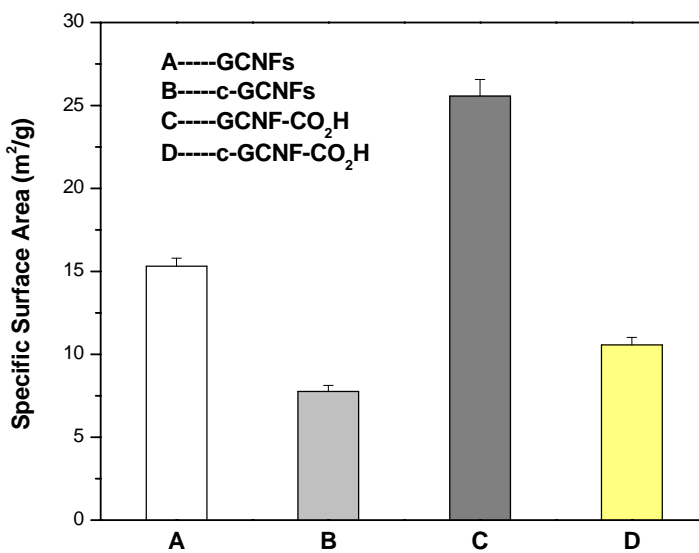


Figure 17. BET specific surface area of GCNFs, c-GCNFs, GCNF-CO₂H, and c-GCNF-CO₂H.

GCNF-Poly (iso-Butyl Methacrylate) Brushes (GCNF-PiBMA)

ATRP of iBMA initiated by GCNF-HEBP-Br is carried out to prepare poly (*iso*-butyl methacrylate) brushes on the surface of GCNFs. Unlike the *in situ* ATRP of *n*-BA in bulk, acetone is used as solvent in ATRP of iBMA to improve solubility of the catalyst complex in relatively nonpolar iBMA.⁹¹ The “halogen exchange” technique is required in ATRP of methacrylate monomers to achieve controlled polymerization, because, while the dormant species are very reactive, the tertiary radicals are relatively stable, resulting in a larger equilibrium constant ($K_{eq} = k_{deact}/k_{act}$) and higher concentration of reactive radical species.⁹² Matyjaszewski et. al.⁹¹ revealed that an R-Br/CuCl system, which results in fast initiation and deactivation, is generally the best initiator/catalyst pair for ATRP of methacrylate monomers. In this work, since the initiator, GCNF-HEBP-Br, is R-Br based, CuCl is used as the catalyst. The polymerization is effected at 50 °C for 96 h, resulting in a polymer content of 45 wt% in the GCNF-PiBMA sample. A control experiment is also carried out under similar conditions in which ATRP of iBMA is initiated by EBriB in the presence of GCNF-CO₂H to give a polymer sample labeled as c-PiBMA-Br (see Table 5). No significant difference is observed between the absence and presence of GCNF-CO₂H nanofibers, and controlled molecular weight and narrow polydispersity are obtained for both PiBMA-Br and c-PiBMA-Br.

Functional moieties on the surface of GCNFs can be identified by FT-IR as shown in

Figure 18. The weak band appearing near 1716 cm^{-1} in the spectrum of GCNF-CO₂H is assigned to the C=O stretching from carboxyl groups. The GCNF-HEBP-Br spectrum is very similar to that of GCNF-CO₂H except for the presence of the characteristic carboxyl C=O stretching band at 1728 cm^{-1} in the latter spectrum. For the GCNF-PiBMA sample, on the other hand, the intensity of the 1728 cm^{-1} band increases significantly, and the C-H stretching at 2954 cm^{-1} also increases in intensity, indicating the presence of polymer moieties.

Table 5. Conditions and results of ATRP of iBMA in 50% acetone.

Sample	[iBMA]:[I]	Catalyst Ratio ^d	T (°C)	Time (h)	Mn	Mw/Mn	Yield
PiBMA-Br	100:1 ^b	200:1:1:1	50	20	20,200	1.17	80.1%
c-PiBMA-Br ^a	100:1 ^b	200:1:1:1	50	20	18,700	1.19	77.8%
GCNF-PiBMA	2000:1 ^c	200:1:1:1	50	96	-	-	-

a. In the presence of GCNF-CO₂H; b. [I]=[EBriB]; c. [I]=[GCNF-HEBP-Br]; d. Catalyst Ratio = [iBMA]:[CuCl]:[PMDETA].

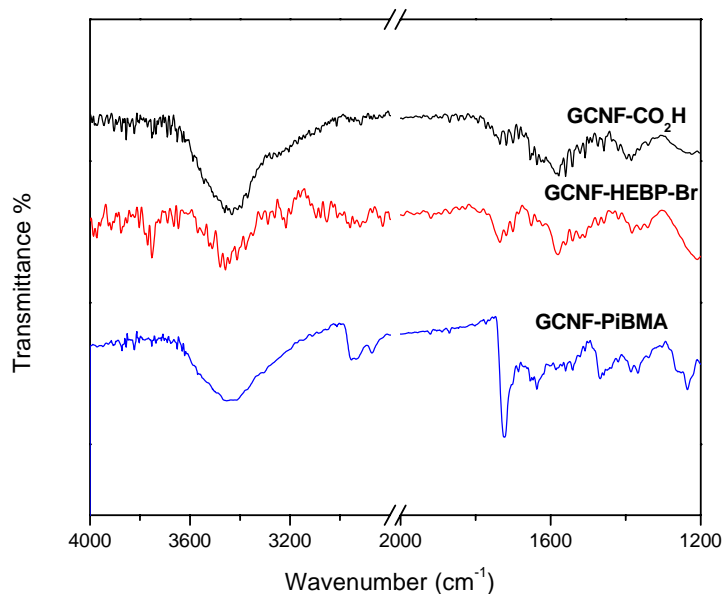


Figure 18. FT-IR spectra of GCNF-CO₂H, GCNF-HEBP-Br, and GCNF-PiBMA.

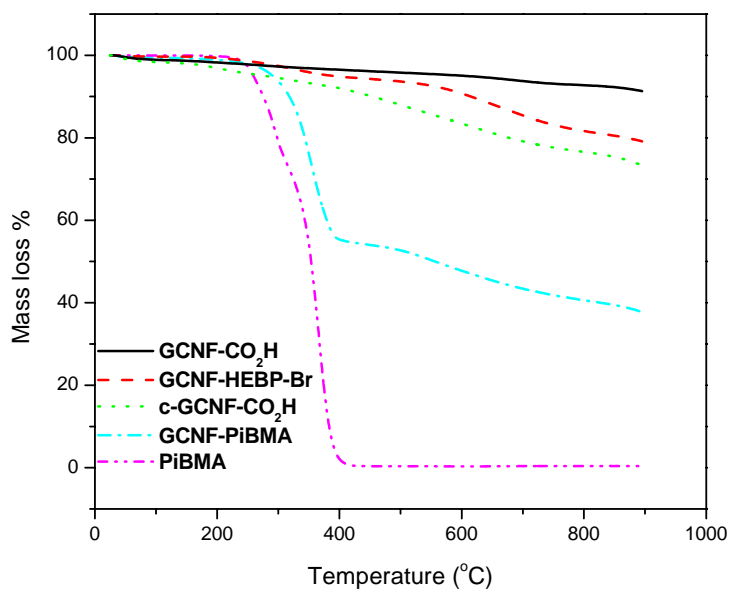


Figure 19. TGA curves of GCNF-CO₂H, GCNF-HEBP-Br, c-GCNF-CO₂H, GCNF-PiBMA, and PiBMA samples

Figure 19 shows the TGA curves of GCNF-CO₂H, GCNF-HEBP-Br, c-GCNF-CO₂H, GCNF-PiBMA, and PiBMA samples recorded under nitrogen. The sharp mass-loss event from 300 °C to 400° C in the GCNF-PiBMA profile is clearly associated with the decomposition of grafted PiBMA brush, since the free PiBMA sample has a characteristic mass-loss in the same temperature range. The profile of c-GCNF-CO₂H sample is different from that of the GCNF-CO₂H sample and has a larger mass-loss than GCNF-HEBP-Br in the entire temperature range from 150 °C to 900 °C, indicating that oligomer radicals are grafted on the surface of c-GCNF-CO₂H during the polymerization process because GCNF-CO₂H nanofibers can act as radical scavengers.

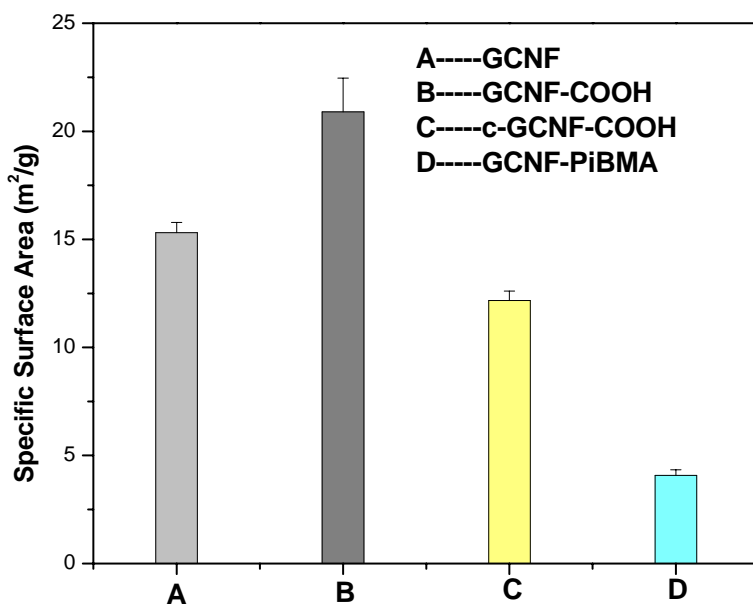


Figure 20. BET specific surface area of (A) GCNF, (B) GCNF-CO₂H, (C) c-GCNF-CO₂H, and (D) GCNF-PiBMA

The c-GCNF-CO₂H sample has a specific surface area ca. 12.1 m²/g, much smaller than ca. 20.9 m²/g for GCNF-CO₂H (see Figure 20). Figure 20 also shows that the specific surface area of GCNF-PiBMA sample is reduced greatly to ca. 4.1 m²/g due to the surface-grafted polymer brushes. The grafted polymer brushes collapse and form a polymer layer around the surface of carbon nanofibers, therefore, the rough surface of GCNF-CO₂H is converted to a smooth polymer coating, resulting in much smaller specific surface area for the GCNF-PiBMA sample.

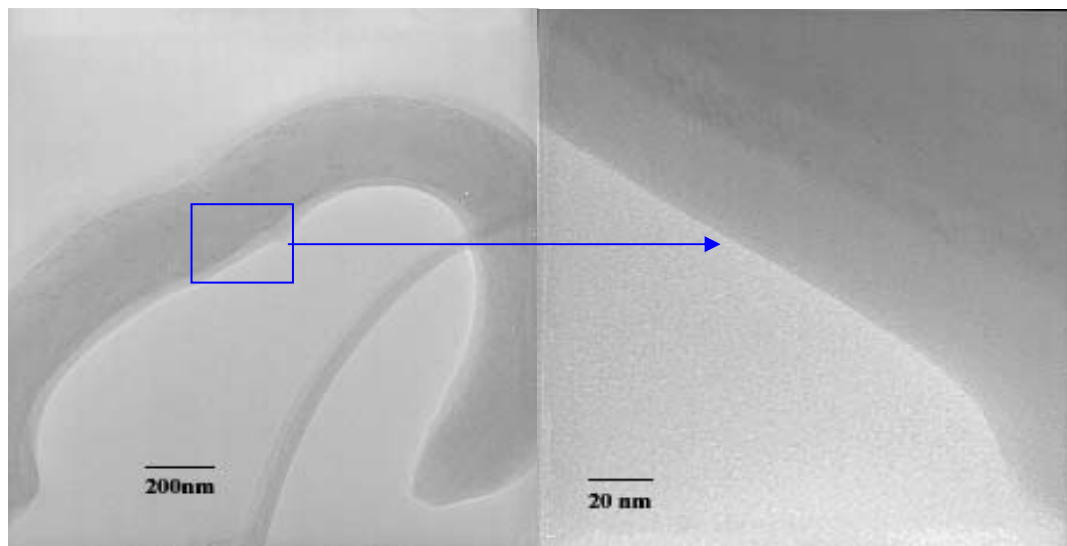


Figure 21. TEM images of individual GCNF-PiBMA carbon nanofiber.

Figure 21 presents the TEM images of an individual nanofiber of GCNF-PiBMA. It is clear that the GCNF-PiBMA nanofiber (dark contrast) is covered by a polymer layer (lighter contrast). The polymer layer is formed by polymer brushes wrapping around the nanofiber surface and, as found in GCNF-PBA nanofibers, the thickness of this polymer

layer varies along the nanofiber. For example, the thickness of polymer layer increases from around 30 nm to about 50 nm along the nanofiber.

A dispersibility test of GCNF-PiBMA samples in a series of organic solvents with various polarities confirms dramatic improvement of carbon nanofiber dispersibility in nonpolar and weak polar solvents. As shown in Figure 22, GCNF-CO₂H nanofibers precipitate from carbon tetrachloride immediately after a sonication treatment, whereas GCNF-PiBMA samples form stable dispersions in carbon tetrachloride, toluene, and acetone. GCNF-PiBMA does not disperse in polar solvent of methanol, as methanol does not dissolve PiBMA polymer chains very well.

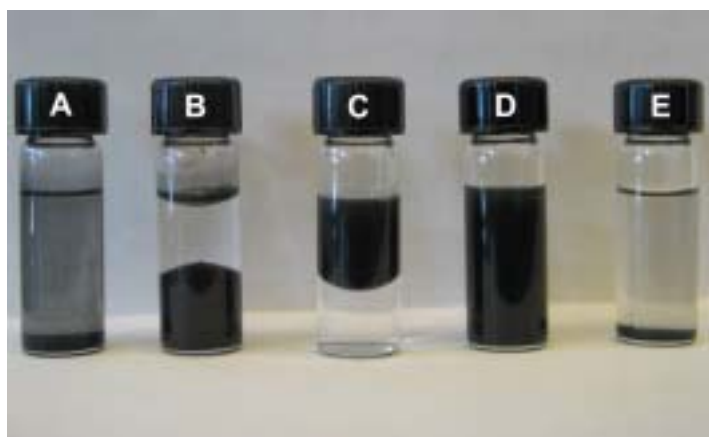


Figure 22. Dispersibility of (A) GCNF-CO₂H sample in CCl₄, (B), (C), (D) (E) GCNF-PiBMA sample in H₂O/CCl₄, toluene/H₂O, acetone, and methanol, respectively. Concentration of the dispersions is about 2.5mg/mL.

GCNF-Poly (tert-Butyl Acrylate) Brushes (GCNF-tBA) and GCNR-Poly (Acrylic Acid) Brushes (GCNF-PAA)

It is demonstrated above that the *in situ* ATRP strategy is successful in synthesis of

both polyacrylate and polymethacrylate brushes on the surface of GCNFs. For applications in biological fields, hydrophilic polymer brushes are desirable for enhancement of the dispersibility of GCNFs in aqueous media. To synthesize hydrophilic polymer brushes on the surface of GCNFs, hydrophobic PtBA brushes are firstly synthesized by the *in situ* ATRP strategy, and then the *tert*-butyl groups in PtBA chains are removed by hydrolysis with CF₃CO₂H to obtain hydrophilic PAA brushes.

Table 6. Conditions and results of ATRP of tBA in 50% acetone.

Sample	[tBA]:[I]	Catalyst Ratio ^d	T (°C)	Time (h)	Mn	Mw/Mn	Yield	PtBA
PtBA-Br	100:1 ^b	100:1:1:1	60	22	7900	1.06	79.1%	-
c-PtBA-Br ^a	100:1 ^b	100:1:1:1	60	22	3900	1.08	44.0%	-
GCNF-PtBA1	2200:1 ^c	100:1:1:1	60	22	-	-	-	18 %
GCNF-PtBA2	2200:1 ^c	100:1:1:1	60	144	-	-	-	23 %

a. In the presence of GCNF-CO₂H; b. [I]=[MBrP]; c. [I]=[GCNF-HEBP-Br]; d. Catalyst Ratio = [tBA]:[CuBr]:[PMDETA].

ATRP of *t*-BA with GCNF-HEBP-Br as initiator is carried out in acetone solution to prepare PtBA brushes on the surface of GCNFs. The polar solvent acetone is used to improve the solubility of the catalyst during ATRP polymerization of *t*-BA.⁹³ Two samples of GCNF-PtBA were prepared by ATRP of tBA at 60 °C for 22 h and 144 h, respectively (see Table 6). However, no significant viscosity increase of the reaction mixture is observed during the polymerization process for either sample. Polymer brush

content in GCNF-PtBA1 and GCNF-PtBA2 is 18 wt% and 23 wt%, respectively.

TGA curves of GCNF-PtBA samples shown in Figure 23 reveal different features from those of GCNF-PBA and GCNF-PiBMA nanofibers. Two sharp mass-loss events originate from the loss of PtBA brushes: the first one from 200 °C to 240 °C is attributed to dissociation of tert-butyloxy groups from the PtBA sides chains, while the second mass-loss event from 240 °C to 440 °C is assigned to the gradual decomposition of PtBA backbone atoms.⁸⁴ Free polymers of PtBA start to lose mass at only 150 °C, which is about 50 °C lower than the PtBA grafted on the surface of GCNFs. Dissociation temperature increase for the PtBA moieties in GCNF-PtBA is attributed to the confined movement of the surface-immobilized polymer chains. TGA curve of GCNF-PAA2 presents a different profile from that of GCNF-PtBA2. Continuous mass-loss of PAA moieties from 100 °C to 440 °C is attributed to the intrinsic low thermal stability of the PAA chains. The smaller polymer content in GCNF-PAA2 is consistent with the loss of tert-butyloxy groups by hydrolysis of PtBA polymer chains.

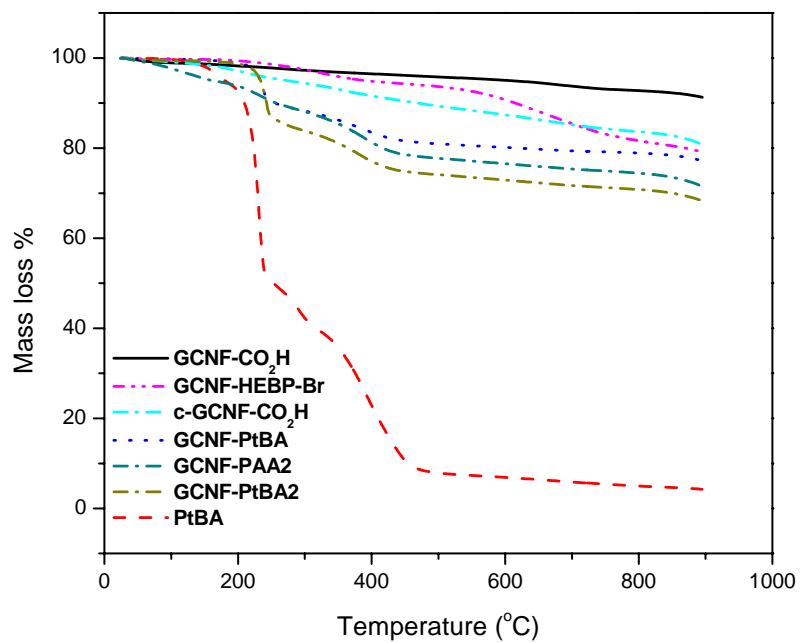


Figure 23. TGA curves of GCNF-CO₂H, GCNF-HEBP-Br, c-GCNF-CO₂H, GCNF-PtBA, GCNF-PAA2, GCNF-PtBA2, and PtBA.

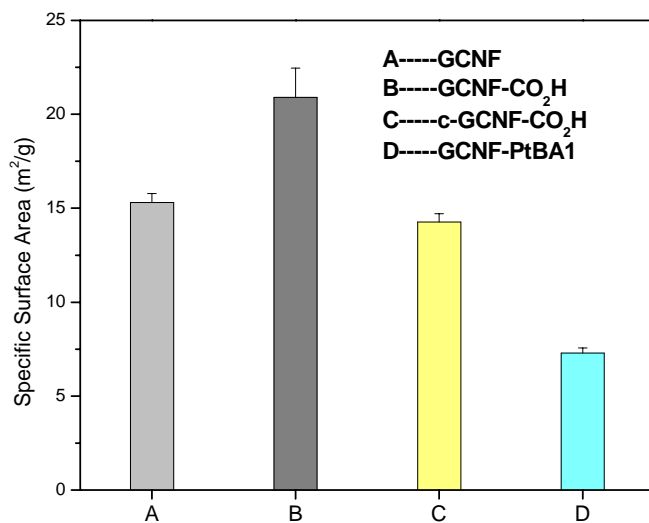


Figure 24. BET specific surface area of (A) GCNF, (B) GCNF-CO₂H, (C) c-GCNF-CO₂H, and GCNF-PtBA samples.

As shown in Figure 24, the specific surface area of GCNF-PtBA1 is ca. 7.19 m²/g, smaller than that of GCNF-CO₂H ca. 20.90 m²/g, because the rugged nanofibers surface is covered by a smooth layer of PtBA brushes. Note that c-GCNF-CO₂H also has a smaller specific surface area ca. 14.72 m²/g than that of GCNF-CO₂H. As discussed in previous section of GCNF-PBA, oligomer fragments are entrapped on the nanofibers surface during the polymerization process due to the radical scavenger nature of carbon nanofibers and the c-GCNF-CO₂H nanofiber surface is partially covered by the oligomer fragments, resulting in reduction of the specific surface area of nanofibers.

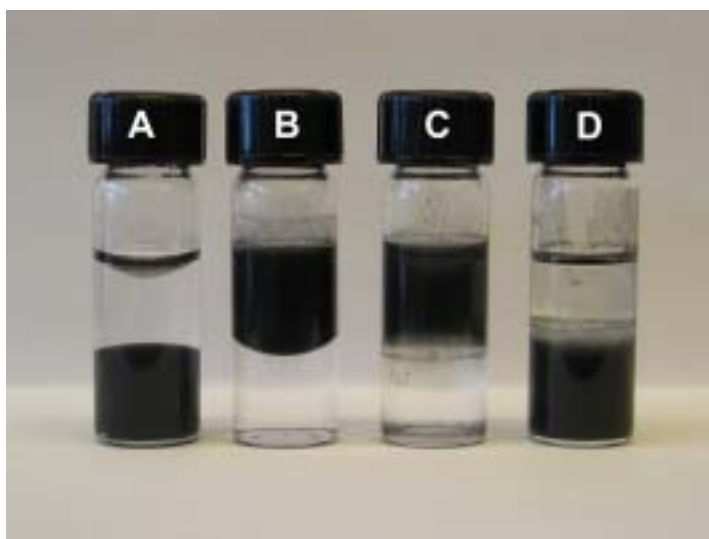


Figure 25. Dispersibility test of (A) and (B) GCNF-PtBA2 samples in H₂O (upper)/CHCl₃ (lower) and toluene (upper)/H₂O (lower); (C) and (D) GCNF-PAA2 samples in H₂O (upper)/CHCl₃ (lower) and toluene (upper)/H₂O (lower).

Dispersibility of GCNF-PtBA samples is greatly improved by surface-grafted PtBA brushes. Figure 25 reveals that GCNF-PtBA2 forms stable dispersions in CHCl₃ and toluene, respectively. When the hydrophobic polymers of PtBA are converted to hydrophilic polymers of PAA, however, the GCNF-PAA2 sample does not disperse into either CHCl₃ or toluene but forms stable dispersions in water.

GCNF-Poly(Glycidyl Methacrylate) Brushes (GCNF-PGMA)

Due to the reactivity of oxirane functional groups, glycidyl methacrylate has been a widely applied commercial monomer and has played a very important role in polymer coatings, adhesives and matrix resins.⁹⁴ Homo and copolymers of GMA with controlled molecular weight and low polydispersity have been prepared using ATRP technology and polymerization conditions, including solvents, catalysts, ligands, and temperatures, have been established.^{95,96} Surface-initiated ATRP of GMA to prepare poly (glycidyl methacrylate) brushes on the surface of silicon wafers has also been reported.^{97,98} Further ring opening of the oxirane side chains of PGMA brushes by primary amine groups has been performed to introduce other functional groups, such as glucose oxidase and alkyl substituents.⁹⁹

To incorporate oxirane groups into GCNF/polymer brushes for applications requiring covalent binding to epoxy resins, surface-initiated ATRP of GMA was carried out to prepare GCNF-PGMA brushes using GCNF-Cl as initiator, CuCl and CuCl₂ as catalyst, and PMDETA as ligand. The formed GCNF-PGMA brushes were purified by the same procedures as other GCNF-polymer brushes discussed earlier in this chapter to make sure

that no free polymers are absorbed onto the GCNF nanofibers.

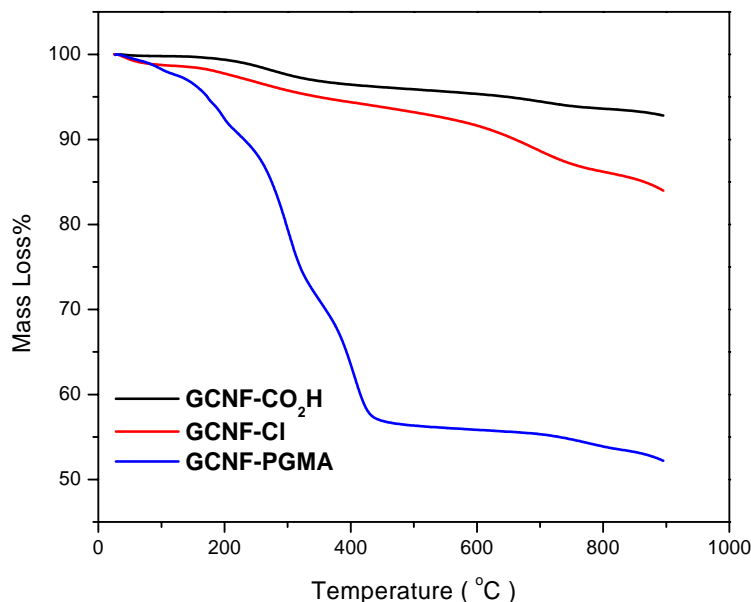


Figure 26. TGA curves of oxidized GCNF (GCNF-CO₂H), chlorine initiator immobilized GCNF (GCNF-Cl) and PGMA brushes grafted GCNF (GCNF-PGMA).

Comparison of TGA curves, shown in Figure 26, reveals the presence of grafted PGMA brushes in the GCNF-PGMA sample. The mass-loss event from 100 °C to 430 °C is attributed to the thermal decomposition of PGMA chains grafted on the surface of GCNFs. Surface-grafted PGMA brushes are also identified in the FT-IR spectrum of GCNF-PGMA (see Figure 27). GCNF-Cl nanofibers have a similar spectrum as oxidized GCNF nanofibers, while the spectrum of GCNF-PGMA shows absorption bands at 2933 cm⁻¹ and 2865 cm⁻¹, characteristic for C-H stretching, and a carbonyl C=O stretching band at 1716 cm⁻¹ with high intensity from ester groups in the PGMA polymer chains.

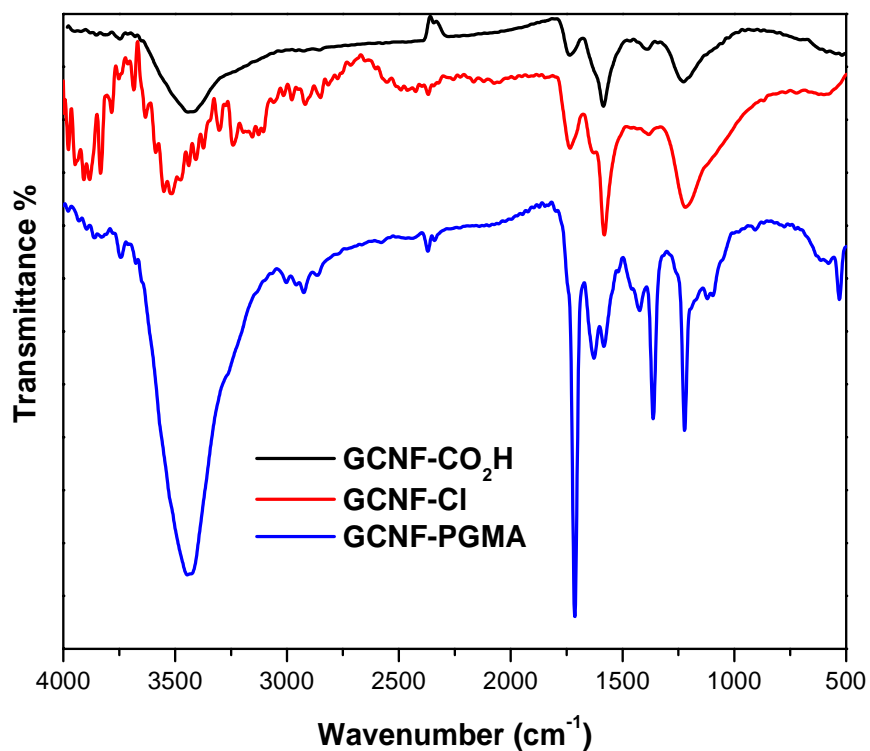


Figure 27. FTIR spectra of oxidized GCNF (GCNF-CO₂H), chlorine initiator immobilized GCNF (GCNF-Cl) and PGMA brushes grafted GCNF (GCNF-PGMA).

Polymerization conditions for the synthesis of GCNF-PGMA polymer brushes are based on the reported procedures with some minor modifications to optimize ATRP of GMA from the surface of GCNFs. Typical conditions are listed in Table 7. The resultant PGMA brushes have reasonable polymer contents up to ca. 38.1 wt% for GCNF-PGMA3.

Table 7. Conditions and results of ATRP of glycidyl methacrylate initiated by GCNF-Cl

Sample	[GMA]:[I] ^a	Catalyst Ratio ^b	Concentration	Temp (°C)	Time (h)	PGMA wt% ^c
GCNF-PGMA1	4575:1	100:1:0.1:1.1	50%	30	48	24.9
GCNF-PGMA2	4575:1	50:1:0.1:1.1	100%	30	24	32.1
GCNF-PGMA3	4575:1	50:1:0.1:1.1	50%	30	48	38.1
GCNF-PGMA4	4575:1	50:1:0.1:1.1	50%	50	24	28.0

a. Molarity of immobilized initiators calculated by (weight of GCNF-Cl \times 3.3×10^{-5} mol/g). b. Catalyst Ratio = [GMA]:[CuCl]:[CuCl₂]:[PMDETA]. c. Obtained from the TGA curves.

The polymerization rate of surface-initiated ATRP of GMA by GCNF-Cl is determined by thermogravimetric analysis of samples taken at desired times during the polymerization process. As shown in Figure 28, the growth rate of polymer brush levels off after about 5 h of polymerization, which means that the polymerization of GMA for either GCNF-PGMA1 or GCNF-PGMA3 is not a true living/controlled ATRP because a plot of polymer content over time should be linear for an ideal ATRP system. The low concentration of initiators on the surface of GCNF fibers might be responsible for the uncontrolled nature of GMA polymerization and the variant local environment on rugged surface of GCNFs also plays an important role in the deviation from normal solution ATRP kinetics. For ATRP, the polymerization rate is proportional to the concentration of both initiator and monomer, so the rate of polymerization for GCNF-PGMA3 is expected to be higher than that of GCNF-PGMA1 because the latter has lower initiator

concentration. The same comparison applies to GCNF-PGMA2 and GCNF-PGMA4 because of higher monomer concentration in the former system as shown in Table 7.

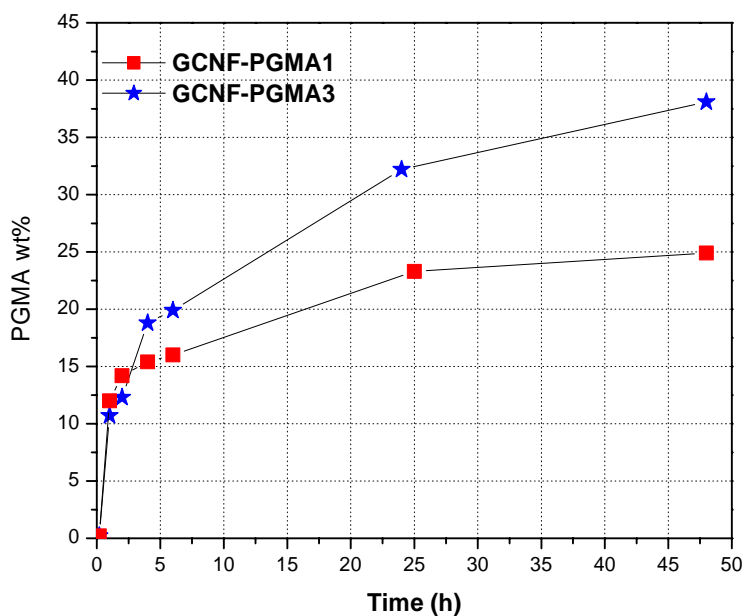


Figure 28. Dependence of grafted PGMA brushes on the surface of GCNF nanofibers on the polymerization time of surface-initiated ATRP.

A series of TGA curves of GCNF-PGMA3 samples taken at different time intervals is shown in Figure 29. It is notable that these curves have similar profiles with a continuous mass-loss event from 100 °C to 430 °C, characteristic for decomposition of PGMA chains, and the mass-loss corresponding to polymer brushes of PGMA increases from about ca. 10 wt% at 1 h to ca. 38.1 wt% at 48 h as the polymerization time increases.

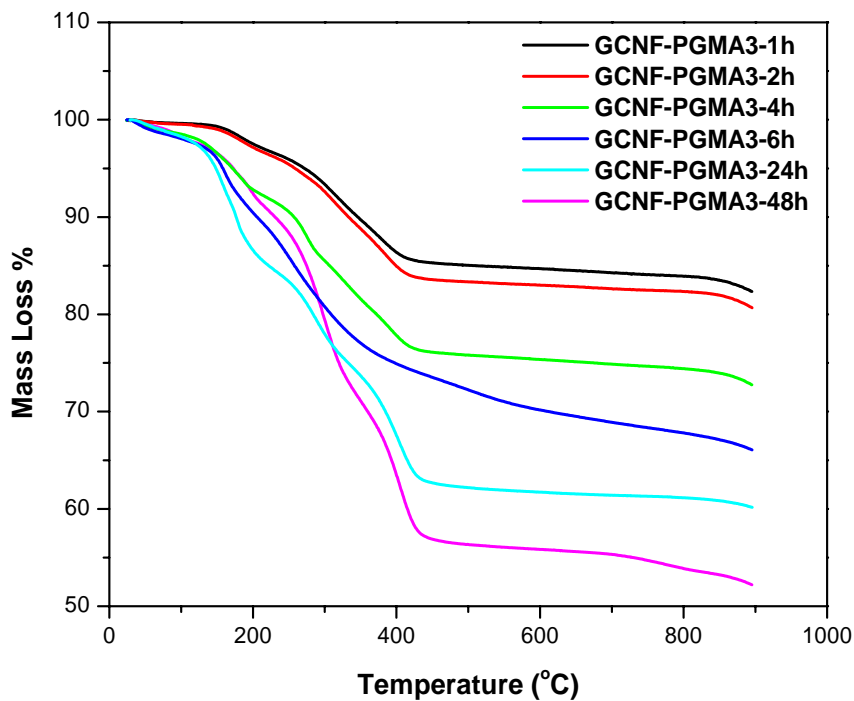


Figure 29. TGA curves of GCNF-PGMA3 samples at different time intervals during the 48 h ATRP course.

2.4. Conclusions

A new strategy for surface-functionalization of GCNFs has been developed by growing polymer brushes from the surface of herringbone GCNFs via *in situ* ATRP. Sequential surface-functionalization of as-prepared GCNFs by oxidation with nitric acid, acylation with thionyl chloride, and esterification with HBBP, HEBP, or TCE immobilizes ATRP initiator molecules onto the surface of GCNFs. ATRP of *n*-butyl acrylate initiated by the initiator-immobilized GCNFs affords GCNF-poly (*n*-butyl acrylate) polymer brushes. ATRP of *iso*-butyl methacrylate, *tert*-butyl acrylate, and

glycidyl methacrylate in acetone or DPE solution gives the corresponding GCNF-poly(*iso*-butyl methacrylate), GCNF-poly (*tert*-butyl acrylate), and GCNF-poly(glycidyl methacrylate) polymer brushes, respectively. Chain length of polymer brushes can be controlled by changing the conditions of *in situ* ATRP. GCNF-PBA, GCNF-PiBMA, GCNF-PtBA, and GCNF-PGMA polymer brushes form stable dispersions in non-polar and weak-polar organic solvents, such as chloroform, toluene, and acetone, due to the excellent solubility of surface-grafted polymers in these solvents. Acid hydrolysis of a GCNF-poly(*tert*-butyl acrylate) polymer brush forms a hydrophilic GCNF-poly(acrylic acid) polymer brush which has good dispersibility in water.

CHAPTER III

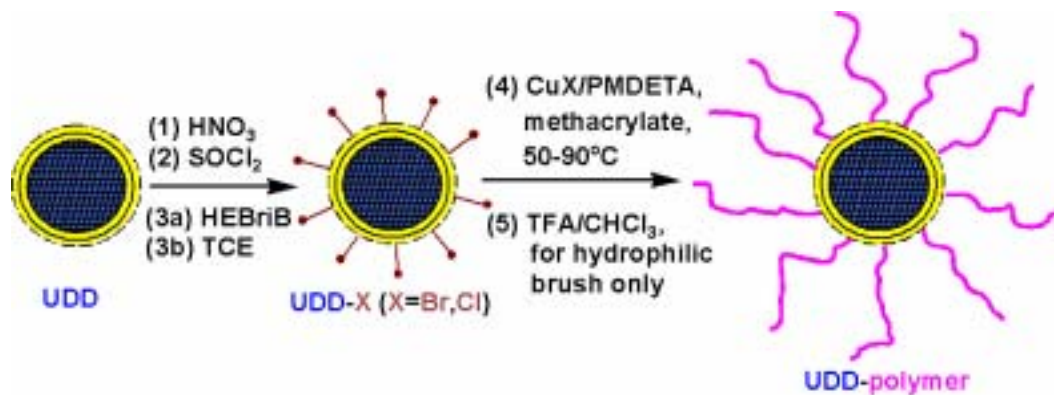
SYNTHESIS OF UDD/POLYMER BRUSHES VIA ATOM TRANSFER RADICAL POLYMERIZATION

3.1. Introduction

Ultradispersed diamond (UDD) prepared by detonation of carbonaceous materials consists of diamond nanocrystals 4-6 nm in diameter that tend to form primary particles 20-50 nm in diameter. These particles survive severe conditions of purification of UDD from the detonation soot and cannot be reduced in size by mechanical grinding.³ UDD particles are covered by an onion-like carbon shell consisting of several layers of graphite carbon.^{43,100} Purification of as-prepared UDD powder entails exposure to oxidative acids resulting in the formation of functional groups, such as hydroxyl and carboxyl groups, on the surface of UDD particles.

It is of great interest to incorporate UDD particles into coatings or bulk materials to impart the remarkable properties of diamond to surfaces and composites. UDD particles have been used to improve the wear- and corrosion-resistance of galvanic coatings, lubricating oils/greases, and magnetic media coatings by incorporating as-prepared UDD or UDD modified with small molecules into various organic/polymer matrices.³ Several potential medical applications of UDD-blended materials have also been reported.¹⁰¹ Partial oxidation of the graphitic shell layer phase of UDD is readily achieved and has

been used to facilitate interactions with surfactant and to enhance poor UDD dispersibility in solvents or water.^{52,61,64,65,102} Recently, the formation of novel glass coatings of dispersed, surface-fluorinated UDD has been reported.¹⁰³



Scheme 6. Synthesis of UDD/polymer brushes via surface-initiated ATRP of methacrylate monomers.

For bulk-scale applications utilizing UDD, such as fabrication of composite materials, the dispersibility of UDD particles need to be greatly enhanced. Controlling the surface reactivity and hydrophobic/hydrophilic dispersion properties of surface-functionalized UDD is highly desirable. These objectives have now been achieved using the same “grafting-from” approach described in Chapter II for GCNF/polymer brushes, by which organic polymers of choice can be grown directly from UDD particle surfaces in remarkably high surface density via *in situ* ATRP technique. This chapter reports the first syntheses of UDD/polymer brush materials, specifically hydrophobic UDD-poly(*iso*-butyl methacrylate), UDD-PiBMA, UDD-poly(*tert*-butyl methacrylate),

UDD-PtBMA, UDD-poly(octadecyl methacrylate), UDD-POMA, UDD-(glycidyl methacrylate), UDD-PGMA, and hydrophilic UDD-poly(methacrylic acid), UDD-PMAA. As illustrated below in Scheme 6, ATRP initiators, hydroxyethyl-2-bromoisobutyrate (HEBriB) or 2,2,2-trichloroethanol (TCE), are covalently immobilized on the surface carboxyl sites, UDD-CO₂H, via an ester linkage. The *in situ* ATRP of methacrylate monomers present in solution from grafted initiator molecules gives the corresponding UDD/polymer brush materials. Both hydrophobic and hydrophilic UDD/polymer brushes have been prepared.

3.2. Experimental Section

Materials

Ethylene glycol (99.8%), 2-bromo-2'-methylpropionyl bromide (97%), ethyl 2-bromoisobutyrate (EBriB, 98%), 2,2,2-trichloroethanol (TCE, 98%), CuBr (99.999%), CuCl (99.999%), N,N,N',N'',N'''-pentamethyldiethylenetriamine (PMDETA, 99%), and triethylamine (TEA, 99.5%) were purchased from Aldrich and used as received. Iso-Butyl methacrylate (iBMA, Aldrich, 99%), tert-butyl methacrylate (tBMA, Aldrich, 98%), octadecyl methacrylate (OMA, tech, Aldrich) and glycidyl methacrylate (GMA, Aldrich, 97%) were purified by passing through an alumina column and stored under N₂ at -15 °C before use. Ultradispersed diamond (UDD) was provided by ALIT (Ukraine).

Solvents were distilled before use, and other reagents were used without further purification.

Instruments and Measurements

Transmission electron microscopy (TEM) was performed on a Philips CM-20T Electron Microscope operated at 200 KeV. 300 MHz ^1H -NMR spectra were recorded on a Bruker AC300 Fourier Transform Spectrometer, using CDCl_3 as solvent. Infrared spectra (IR) were obtained from KBr pressed pellets on an ATI Mattson Genesis Series FT-IR spectrometer. Thermogravimetric analyses (TGA) were performed on a Thermal Analysis Instruments High-Resolution TGA 2950 Thermogravimetric Analyzer. Elemental analysis was performed by Atlantic Microlab, Inc., Norcross, GA. BET surface-area analysis was carried out on a NOVA 1000 High Speed Surface Area & Pore Size Analyzer with nitrogen gas as the absorbent. Atomic force microscopy (AFM) images were taken with a Digital Instruments Multimode IIIa Nanoscope SPM in tapping mode using standard silicon cantilevers with a resonance frequency around 330KHz. To prepare AFM samples, UDD/polymer brush sample was dispersed in THF at a concentration about 1×10^{-4} mg/mL under sonication for 1h, followed by spin casting 1-2 drops of the dispersion on the freshly cleaved mica surface at the spin speed of 4,000 rpm at room temperature. Polymer molecular weights and polydispersity measurements were obtained by gel permeation chromatography (GPC) using a Waters GPC equipped with four 5 mm Waters columns (300mm x 7.7mm) connected in series with increasing pore size and a Waters 2414 refractive index detector. Polystyrene standards were used as calibration, and THF

was used as eluent at a flow rate of 1.00 mL/min.

Synthesis of Hydroxyethyl-2-Bromoisobutyrate (HEBriB)

A 500mL round-bottomed flask was charged with 31.0 g (0.50 mol) of ethylene glycol, 16.0 mL (0.114 mol) TEA, and 200 mL anhydrous THF. The solution was cooled to 0°C, and a solution of 23.0g (0.10mol) of 2-bromo-2'-methylpropionyl bromide dissolved into 20 mL anhydrous THF was added dropwise under nitrogen at 0°C for 2 h. Then the reaction mixture was raised to 45°C and stirred for 24h. Solids were removed by suction filtration, and solvent was removed under reduced pressure. The remaining solids were dissolved into 100 mL deionized water and extracted with CH₂Cl₂ three times. The organic phase was dried over MgSO₄ overnight and the solvent was removed by rotary evaporation. The colorless liquid product was collected by distillation under reduced pressure. Yield: 77.8%. ¹HNMR (300MHz, CDCl₃): δ=1.90 (-C(CH₃)₂Br), δ=4.29 (-CH₂-OCO-), δ=3.85 (HO-CH₂-), δ=2.06 (HO-CH₂-).

Preparation of HEBriB-Immobilized UDD (UDD-Br)

Surface oxidization of as-received UDD (1.00 g) was performed in 100 mL concentrated nitric acid at 140 °C for 6 h. The product, UDD-CO₂H, was diluted with deionized water and filtered through a 0.2 μm Millipore Nylon membrane. After thorough washing with deionized water, UDD-CO₂H was dried in vacuo at room temperature for 48 h to remove residual water. Acylation of surface-oxidized nanodiamond was carried out by reacting 0.70 g UDD-CO₂H in 24.5 g thionyl chloride at 70 °C for 24 h in the presence of 0.40 g DMF. The mixture was cooled to room

temperature and washed with anhydrous THF under nitrogen until the supernate was clear. The product, UDD-C(O)Cl, was dried with a nitrogen flow at room temperature. A 100-mL round-bottomed flask was charged with 0.56 g UDD-C(O)Cl, 10.00 g HEBriB and 0.02 g TEA. The mixture was allowed to react at 75 °C under N₂ gas for 140 h. The solid was filtered through a 0.2 μm Millipore Nylon membrane, and the residue was washed with methanol six times to remove excess HEBriB and TEA. The product was collected and dried in vacuum at room temperature overnight. Elemental analysis (wt%): C, 86.55; H, 0.56; O, 9.79; N, 2.22; Br, 0.88.

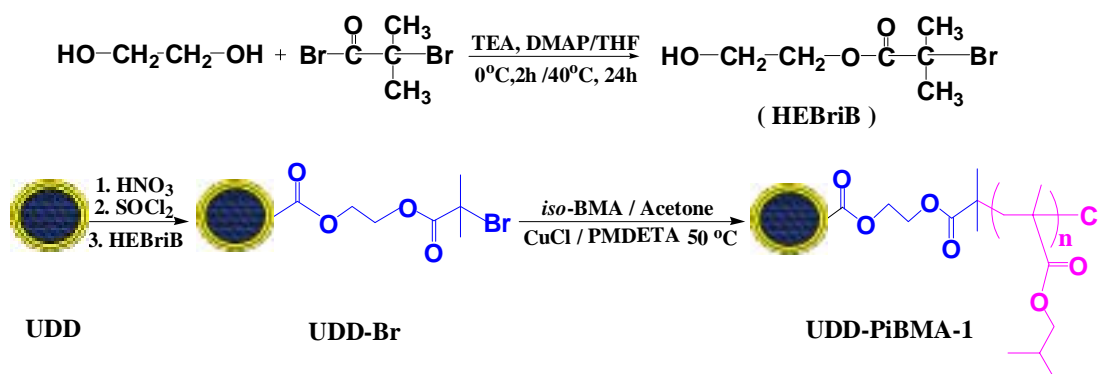
Preparation of TCE-Immobilized UDD (UDD-Cl)

Without additional surface oxidization, 2.43 g as-received UDD was directly reacted with 75.0 g thionyl chloride at 70 °C for 48 h in the presence of 1.0 g DMF. The mixture was cooled to room temperature and washed with anhydrous THF under nitrogen until the supernate was clear. The product, UDD-C(O)Cl, was dried with a nitrogen flow at room temperature. A 100-mL round-bottomed flask was charged with 2.20 g UDD-C(O)Cl, 20.0 g TCE and 0.04 g TEA. The flask was heated in a 75 °C oil bath for 110 h. The purification process for the product of UDD-Cl was the same as that of UDD-Br. Elemental analysis (wt%): C, 87.99; H, 0.55; O, 8.27; N, 2.36; Cl, 0.83.

Synthesis of UDD-Poly(iso-Butyl Methacrylate) Using UDD-Br (UDD-PiBMA-1)

Equipped with a stirring bar, a 25-mL dried, round-bottom flask was charged with 0.2 g UDD-Br and 12.3 mg (0.124 mmol) CuCl. The flask was sealed with a rubber septum and degassed and refilled with nitrogen three times. Deoxygenated acetone (4 mL)

was added into the flask followed by adding 26 μL (0.124 mmol) PMDETA via syringe. The mixture was sonicated for 15 min to form an even dispersion. After adding 4 mL (24.7 mmol) deoxygenated iso-butyl methacrylate via syringe, the flask was heated in a 50 $^{\circ}\text{C}$ oil bath for 22 h. The reaction was quenched by liquid nitrogen and THF was added to disperse the solids. The product was filtered through a 0.2 μm Millipore Nylon membrane and washed with THF. The dispersion-filtration-wash process was repeated six times. Then the solids were dispersed in methanol, followed by filtration to remove catalyst. The collected product was dried in vacuum at room temperature for 16 h.



Scheme 7. Strategy I for synthesis of PiBMA brushes from the surface of UDD particles

ATRP of iso-BMA in the Presence of As-Received UDD (c-UDD-1/c-PiBMA-1)

A 25-mL dried, round-bottom flask was charged with 0.20 g UDD and 12.3 mg (0.124 mmol) CuCl. The flask was sealed with a rubber septum and degassed and refilled with nitrogen three times. Deoxygenated acetone (4 mL) was added into the flask followed by the addition of 26 μL (0.124 mmol) PMDETA via syringe. The mixture was sonicated for 15 min to form a uniform dispersion. Then 4 mL (24.7 mmol) of

deoxygenated iso-butyl methacrylate was added into the flask via syringe, and the mixture was stirred for 5 min. Finally, 36.4 μL (0.247 mmol) EBriB was added via syringe, and the flask was heated in a 50 $^{\circ}\text{C}$ oil bath for 22 h. The reaction was quenched by liquid nitrogen and THF was added to disperse the solids. The product was filtered through a 0.2 μm Millipore Nylon membrane and washed with THF. The filtrate was passed through an alumina column, rotary evaporated to remove the solvent, and vacuum dried at 50 $^{\circ}\text{C}$ for 16 h. The solid residue was purified by repeated dispersion-filtration-wash process using THF four times to remove ungrafted polymers. The collected solid was dried in vacuum at room temperature for 16 h.

ATRP of iso-BMA Initiated by EBriB (PiBMA-1)

The polymerization procedures are the same as those described above except that no as-received UDD was involved. A comparison of reaction conditions and results of ATRP of iso-BMA monomer with Br-based initiator in the absence and presence of as-received UDD is provided in Table 8, respectively.

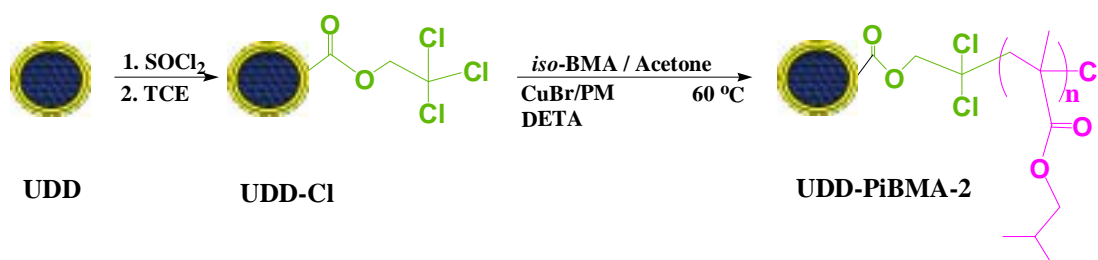
Table 8. Conditions and results of ATRP of *iso*-BMA with Br-based initiators in acetone^a

Sample	[<i>iso</i> -BMA]:[I] ^c	t(h)	Mn	Mw/Mn	Yield (%)
PiBMA-1	100:1	20	14,800	1.11	82.1
c-PiBMA-1 ^b	100:1	22	15,600	1.09	80.3

a. At a catalyst ratio, [iso-BMA]:[CuCl]:[PMDTA], of 200:1:1 at 50 $^{\circ}\text{C}$; b. In the presence of as-received UDD; c. [I]=[EBriB].

Synthesis of UDD-Poly(iso-Butyl Methacrylate) Using UDD-Cl (UDD-PiBMA-2)

A 25-mL dried, round-bottom flask was charged with 0.2 g UDD-Cl and 17.8 mg (0.124 mmol) CuBr. The flask was sealed with a rubber septum and degassed and refilled with nitrogen for three times. Deoxygenated acetone (4 mL) was added into the flask followed by the addition of 26 μ L (0.124 mmol) PMDETA via syringe. The mixture was sonicated for 15 min to form a uniform dispersion. After the addition of 4 mL (24.7 mmol) deoxygenated iso-butyl methacrylate via syringe, the flask was heated in a 60 °C oil bath for 24 h. The purification process of the UDD-PiBMA-2 product was the same as that described in the section for UDD-PiBMA-1.



Scheme 8. Strategy II for synthesis of PiBMA from the surface of UDD particles.

ATRP of iso-BMA in the Presence of As-Received UDD (c-UDD-2/c-PiBMA-2)

A 25-mL dried, round-bottom flask was charged with 0.20 g UDD and 17.8 mg (0.124 mmol) CuBr. The flask was sealed with a rubber septum and degassed and refilled with nitrogen for three times. Deoxygenated acetone (4 mL) was added into the flask followed by the addition of 26 μ L (0.124 mmol) PMDETA via syringe. The mixture was sonicated for 15 min to form a uniform dispersion. Then 4 mL (24.7 mmol)

deoxygenated iso-butyl methacrylate was added into the flask via syringe, and the mixture was stirred for 5 min. Finally, 23.8 μL (0.247 mmol) TCE was added via syringe, and the flask was heated in a 60 $^{\circ}\text{C}$ oil bath for 24 h. The purification process of the product was the same as that described in the section for UDD-PiBMA-1.

ATRP of iso-BMA Initiated by TCE (PiBMA-2)

The polymerization procedures are the same as those described above except that no as-received UDD was involved. A comparison of reaction conditions and results of ATRP of iso-BMA monomer with Cl-based initiator in the absence and presence of as-received UDD is provided in Table 9, respectively.

Table 9. Conditions and results of ATRP of iso-BMA with Cl-based initiators in acetone.^a

Sample	[iso-BMA]:[I] ^c	Mn	Mw/Mn	Yield (%)
PiBMA-2	100:1	13,600	1.12	82.7
c-PiBMA-2 ^b	100:1	11,900	1.11	84.0

a. At a catalyst ratio, [iso-BMA]:[CuBr]:[PMDETA], of 200:1:1 at 60 $^{\circ}\text{C}$ for 24 h; b. In the presence of as-received UDD; c. [I]=[TCE].

Synthesis of UDD-Poly(tert--Butyl Methacrylate) (UDD-PtBMA)

A 25-mL dried, round-bottom flask was charged with 0.2 g UDD-Cl and 23.8 mg (0.246 mmol) CuCl. The flask was sealed with a rubber septum and degassed and refilled with nitrogen for three times. Deoxygenated toluene (4 mL) was added into the flask followed by the addition of 51.4 μL (0.246 mmol) PMDETA via syringe. The mixture

was sonicated for 15 min to form a uniform dispersion. After the addition of 4 mL (24.6 mmol) deoxygenated *tert*-butyl methacrylate via syringe, the flask was heated in a 90 °C oil bath for 24 h. The purification process of the UDD-PtBMA product was the same as that of UDD-PiBMA-1.



Scheme 9. Strategy for synthesis of PtBMA from the surface of UDD particles.

ATRP of tert-BMA in the Presence of As-Received UDD (c-UDD-3/c-PtBMA)

A 25-mL dried, round-bottom flask was charged with 0.20 g of as-received UDD and 23.8 mg (0.246 mmol) CuCl. The flask was sealed with a rubber septum and degassed and refilled with nitrogen three times. Deoxygenated toluene (4 mL) was added into the flask followed by the addition of 51.4 μ L (0.246 mmol) PMDETA via syringe. The mixture was sonicated for 15 min to form a uniform dispersion. Then 4 mL (24.6 mmol) deoxygenated *tert*-butyl methacrylate was added into the flask via syringe, and the mixture was stirred for 5 min. Finally, 23.7 μ L (0.246 mmol) TCE was added via syringe, and the flask was heated in a 90 °C oil bath for 24 h. The purification process of the product was the same as that described in 2.3.5.

ATRP of tert-BMA Initiated by TCE (PtBMA)

The polymerization procedures are the same as those described in 2.3.11. except that no as-received UDD was involved. A comparison of reaction conditions and results of ATRP of tert-BMA monomer with Cl-based initiator in the absence and presence of as-received UDD is provided in Table 10, respectively.

Table 10. Conditions and results of ATRP of tert-BMA in toluene.^a

Sample	[tert-BMA]:[I] ^c	Mn	Mw/Mn	Yield(%)
PtBMA	100:1	12,600	1.17	95
c-PtBMA ^b	100:1	12,700	1.16	92

a. At a catalyst ratio, [tert-BMA]:[CuCl]:[PMDETA], of 100:1:1 at 90 °C for 21 h; b. In the presence of as-received UDD; c. [I]=[TCE].

Preparation of UDD-Poly (Methacrylic Acid) (UDD-PMAA)

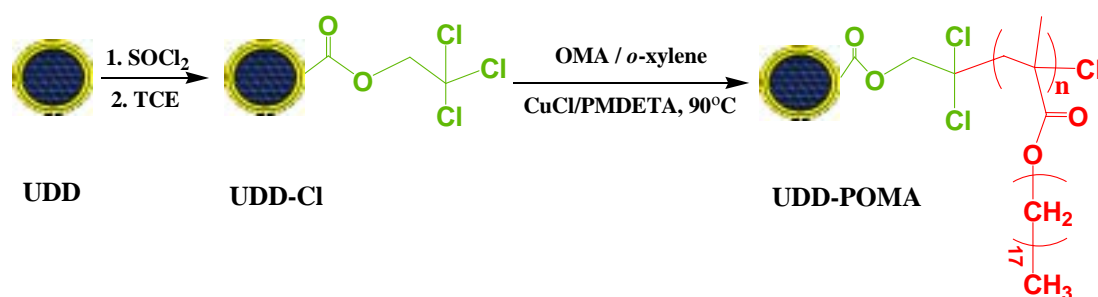
Hydrophilic poly(methacrylic acid) brushes on the surface of UDD were obtained by acidic hydrolysis of PtBMA chains in the UDD-PtBMA sample. Typically, 226 mg UDD-PtBMA was dispersed into 30 mL CHCl₃ in a 100 mL flask by sonication, and 10 mL CF₃CO₂H was added afterward. The mixture was stirred at room temperature for 24 h under nitrogen protection. The solvent was removed by rotary evaporation to collect UDD-PMAA powder and the product was dried in vacuum at room temperature for 16h.

Cleavage of Poly (iso-Butyl Methacrylate) from UDD-PiBMA-2

The cleavage reaction was performed by dispersing 100 mg UDD-PiBMA-2 into 50 mL toluene followed by adding 100 mL iso-butanol and 5 mL concentrated sulfuric acid and refluxing the mixture at 100 °C for 7 days. Solvent and reagents were removed

by rotary evaporation at reduced pressure. The residual solid was dispersed into 100 mL CHCl_3 and extracted with water three times to remove sulfuric acid. The organic dispersion was filtered through a 0.2 μm Millipore Nylon membrane and washed with CHCl_3 . The filtrate was dried via rotary evaporation, and the product of cleaved polymer was dried in vacuum at 40 $^\circ\text{C}$ for 16 h. Molecular weight and polydispersity of the cleaved PiBMA were obtained by GPC: $M_n = 78,400$; $M_w/M_n = 2.47$.

Synthesis of UDD-Poly(Octadecyl Methacrylate) (UDD-POMA)

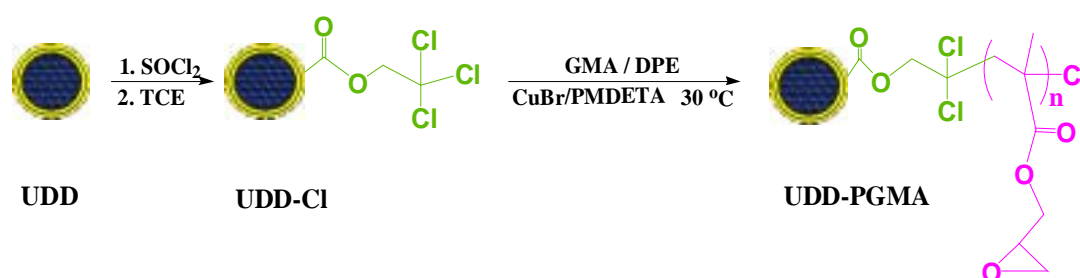


Scheme 10. Strategy for synthesis of POMA from the surface of UDD particles.

A 25-mL round-bottomed flask, equipped with a magnetic stir bar, was charged with 20mg (0.2 mmol) CuCl and 0.2g UDD-Cl. The flask was sealed with a rubber septum and degassed and refilled with N_2 three times. Deoxygenated acetone (4 mL) was added into the flask followed by the addition of 42 μL (0.2 mmol) PMDETA via syringe. The mixture was sonicated for 15 min to form a uniform dispersion. After the addition of 4 mL (20.0 mmol) deoxygenated OMA via syringe, an initial sample was taken and the flask was placed into a 90 $^\circ\text{C}$ oil bath. Aliquots were removed after 1, 2, 4, and 6 h. After 24 h, the reaction mixture was quenched with liquid N_2 and diluted with THF. The

mixture was centrifuged and washed with THF six times to remove ungrafted polymers. Then the solid residue was dispersed in THF and precipitated into excess methanol to remove catalyst. By filtering through a 0.45 μ m Nylon membrane, the solid product of UDD-POMA was collected and dried in a vacuum oven overnight at room temperature.

Synthesis of UDD-Poly(Glycidyl Methacrylate) (UDD-PGMA)



Scheme 11. Strategy for synthesis of PGMA from the surface of UDD particles.

A 25-mL round-bottomed flask, with a magnetic stir bar, was charged with 43.4 mg (0.302 mmol) CuBr and 0.20 g UDD-Cl. The flask was sealed with a rubber septum and degassed and refilled with N_2 three times. Deoxygenated DPE (4 mL) was added into the flask followed by the addition of 63.6 μ L (0.302 mmol) PMDETA via syringe. The mixture was sonicated for 15 min to form a uniform dispersion. After the addition of 4 mL (30.2 mmol) deoxygenated GMA via syringe, an initial sample was taken and the flask was placed into a $30\text{ }^\circ\text{C}$ oil bath. Aliquots were removed after 1, 2, 4, and 6 h. After 24 h, the reaction mixture was quenched with liquid N_2 and diluted with THF. The mixture was centrifuged and washed with THF six times to remove ungrafted polymers. The solid product of UDD-PGMA was collected and dried in the vacuum oven overnight

at room temperature.

3.3. Results and Discussion

The ultradispered diamond used in this work is a commercial product. Some basic characterizations, such as TEM, AFM, XRD, and FT-IR, are conducted to obtain structural information about as-received UDD powder. From the TEM images shown in Figure 30, UDD particles have a relatively wide size distribution. Image A shows individual UDD nanocrystals more than ca. 20 nm in diameter, whereas nanocrystals in image B have particle size smaller than ca. 10 nm. These nanocrystals form uncrushable particles with diameters in tens of nanometers to reduce surface energy. AFM images of an individual UDD particle on a mica surface (see Figure 31) reveal that this particle has a diameter about 80 nm.

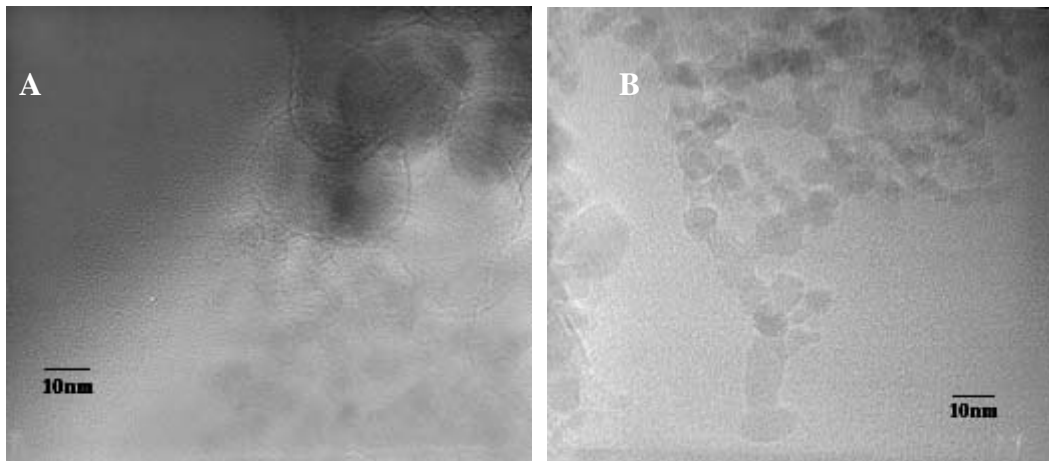


Figure 30. TEM images of as-received UDD particles.

The graphitic shell surrounding diamond nanoparticles is difficult to visualize by TEM and AFM due to the poor phase contrast. XRD is a powerful tool for characterizing UDD, because the diamond core has specific (111), (220), and (311) x-ray reflections at 43.9, 75.3, and 91.5 degrees in 2θ , respectively.^{43,52,101} As shown in Figure 32, symmetric broad diffraction peaks at 43.5 and 75.1 degrees in 2θ are observed from the nanocrystalline diamond core structure, while a sharp diffraction peak at 21.6 degrees in 2θ is attributed to diffraction from the (222) planes of the fullerene shell. When as-received UDD is treated with concentrated nitric acid at 140 °C for 6 h, additional carboxyl groups are formed on UDD particle surfaces. The integrated-intensity ratio of the fullerene (222)/diamond (111) diffraction peaks observed in the diffraction pattern of UDD-CO₂H is smaller than that of as-received UDD, indicating that the onion-like carbon shells are partially etched off by nitric acid oxidation.

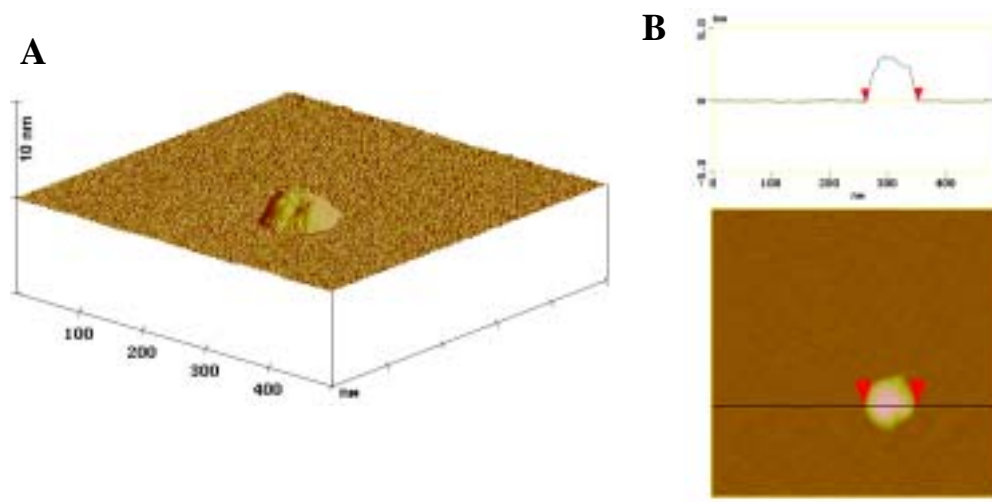


Figure 31. AFM tapping-mode height image (A) and phase image (B) of an individual as-received UDD particle as spin-coated onto a mica surface.

Oxidized UDD is further reacted with thionyl chloride and HEBriB consecutively to immobilize bromine-based ATRP initiator molecules at surface sites (UDD-Br), whereas as-received UDD is directly reacted with thionyl chloride followed by esterification with TCE to attach chlorine-based ATRP initiator molecules on the surface (UDD-Cl). Elemental analysis (see Table 11) shows the presence of ca. 0.88 wt% bromine atoms in UDD-Br and ca. 0.83 wt% chlorine atoms in UDD-Cl. BET analysis indicates that oxidized UDD has a specific surface area of ca. 121.78 m²/g compared with ca. 131.22 m²/g for as-received UDD. The slight reduction in specific surface area after oxidation could be attributed to partial etching off the initially rough surface. Surface density of initiator molecules is ca. 5.4×10^{17} bromine atoms per square meter (54 Br/100 nm²) for UDD-Br and ca. 1.08×10^{18} chlorine atoms per square meter (36 Cl/100 nm²) for UDD-Cl.

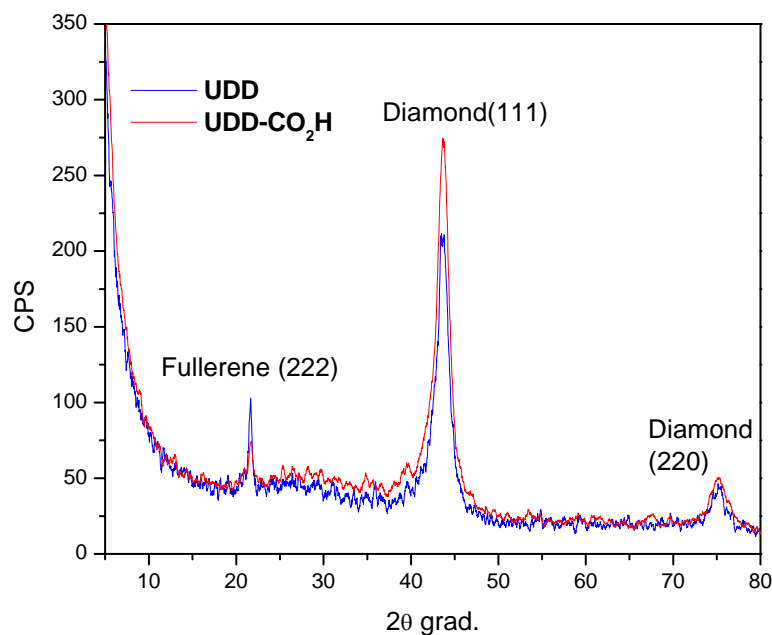


Figure 32. XRD patterns of as-received UDD and oxidized UDD, UDD-CO₂H, samples.

Table 11. Elemental analysis of initiator-immobilized UDD samples.

Element	C (wt%)	H (wt%)	O (wt%)	N (wt%)	Br (wt%)	Cl (wt%)
UDD-Br	86.55	0.56	9.79	2.22	0.88	-
UDD-Cl	87.99	0.55	8.27	2.36	-	0.83

UDD-Poly (iso-Butyl Methacrylate) Brushes by UDD-Br (UDD-PiBMA-1)

To synthesize PiBMA brushes on the surface of UDD particles, ATRP of iBMA monomers initiated by UDD-Br is carried out in 50% acetone solution. The “halogen exchange” technique is employed in this synthesis as well to improve the control of the ATRP of iBMA, in which CuCl is used to affect Br/Cl exchange during polymerization. ATRP conditions of iBMA initiated by UDD-Br are the same as those used in the

polymerization of iBMA initiated by GCNF-HEBP-Br in Chapter II except that the monomer/initiator ratio is about two times higher. Surprisingly, the reaction mixture becomes very viscous after 22 h, indicating that the ATRP polymerization rate of iBMA initiated by UDD-Br is much faster than that of the GCNFs system. Two important reasons may contribute to the improved polymerization rate for UDD-Br over GCNF-HEBP-Br. First, UDD particles have much larger specific surface area than GCNFs, so initiators immobilized on the surface of UDD are more accessible for the dissolved catalyst complex and monomers. Second, GCNFs act as “radical scavengers” in the ATRP process which greatly reduces the concentration of reactive radicals in the reaction system, while radical entrapment is much less distinct for UDD due to the lower graphene content. A control experiment was also carried out in the presence of as-received UDD under identical ATRP conditions except that free initiators were added to initiate the polymerization of iBMA. The polymerization was stopped after 22 h, and the resulting product, c-UDD-1, was thoroughly washed with THF to remove physically absorbed polymers. GPC measurements show that predetermined molecular weight and narrow polydispersity are obtained, indicating that the presence of UDD has no significant effect on ATRP polymerization of iBMA under these reaction conditions.

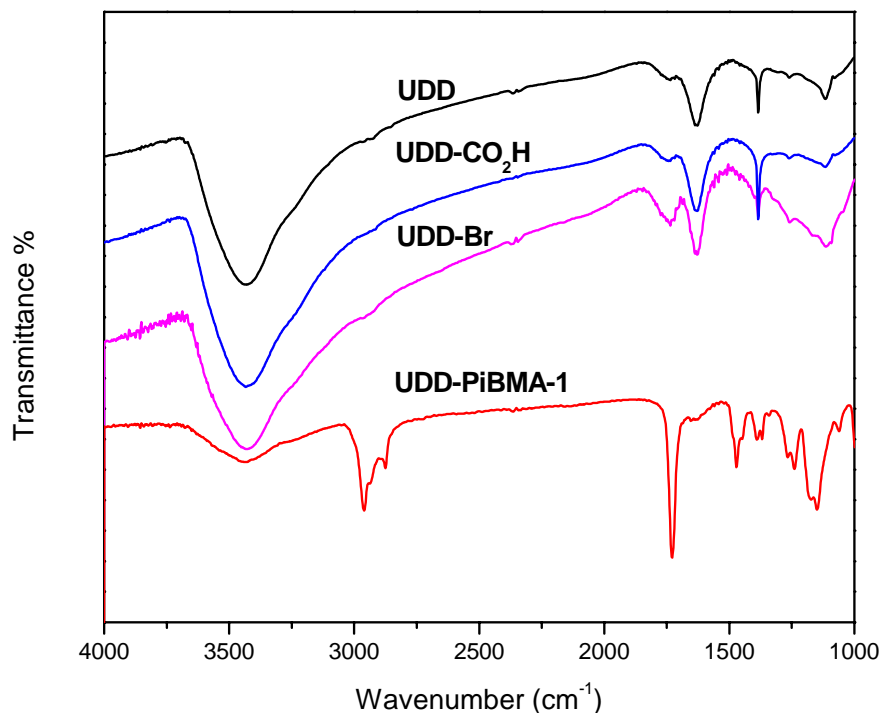


Figure 33. FT-IR spectra of UDD, UDD-CO₂H, UDD-Br, and UDD-PiBMA-Br samples.

FT-IR spectra in Figure 33 indicate that as-received UDD has nearly identical spectral features as oxidized UDD. The broad strong band at 3450 cm⁻¹ can be assigned to an OH stretching vibration. The shoulder observed at 1737 cm⁻¹ is assigned to the C=O stretching vibration of carboxyl groups present on the surface of UDD particles. A broad band centered at 1632 cm⁻¹ is associated with superposition of several bands, such as the OH deformation vibration of adsorbed water and N-H and C-N stretching vibrations. The sharp strong feature at 1384 cm⁻¹ is assigned to N-O bond stretching of NO_x groups introduced by nitric acid oxidation. Band intensity in the range of 1000-1200 cm⁻¹ is

attributed to the C-O vibration of C-O-C groups. The spectrum of UDD-Br shows a distinct enhancement of band intensity at 1737 cm^{-1} attributed to C=O stretching within ester groups of immobilized-initiator molecules. Spectral features uniquely identified with the formation of grafted polymer brush include a dominant band at 1728 cm^{-1} assigned to the C=O stretching vibration of the ester groups in the polymer chains, and characteristic C-H absorption bands at 2956 cm^{-1} and 2872 cm^{-1} .

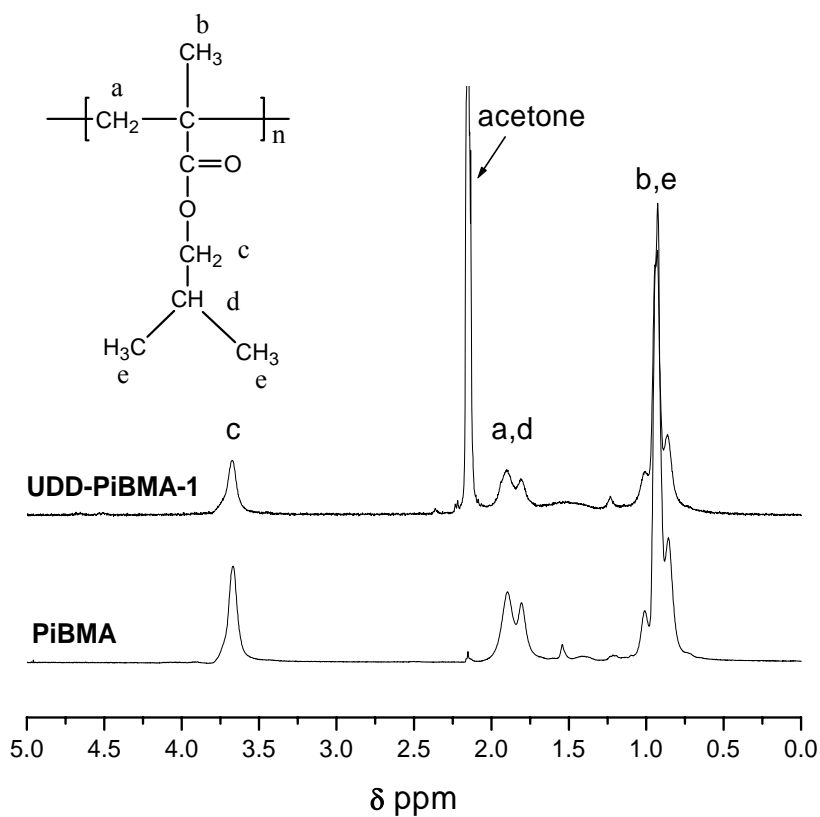


Figure 34. Solution $^1\text{H-NMR}$ spectra of UDD-PiBMA-1 brush and of PiBMA in CDCl_3 solution.

$^1\text{H-NMR}$ spectra of UDD-PiBMA-1 and of PiBMA pure polymer are shown in

Figure 34. Resonances observed at 0.93 ppm, 1.81 ppm, 1.89 ppm, and 3.67 ppm for the UDD-PiBMA-1 polymer brush are readily assigned to the corresponding resonances of the counterpart of PiBMA free polymer. Only a small degree of relaxation broadening is observed for the UDD/polymer brush indicating good extension of the polymer chains into the solution phase.

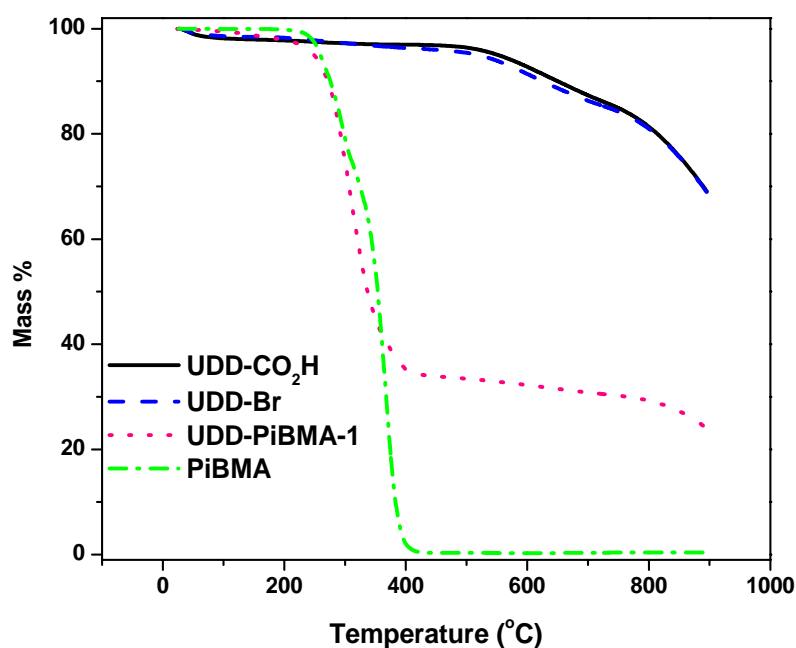


Figure 35. TGA curves of UDD-CO₂H, UDD-Br, UDD-PiBMA-1, and PiBMA samples.

TGA mass-loss curves for UDD-PiBMA-1 and related intermediate materials are shown in Figure 35. Oxidized UDD and initiator-immobilized UDD, UDD-Br, undergo a similar, gradual ca. 30 wt% mass-loss event from 500 °C to 900 °C attributed to decarboxylation, decarbonylation, and dehydration of surface-bound oxyhydrocarbyl groups, including CO₂H functional groups and initiator molecules. With an initiator

molecule content for UDD-Br estimated to be only ca. 2.6 wt% based on elemental analysis, observation of a distinct mass-loss event for degradation of the linker molecule component is not expected. In contrast, thermal decomposition of the UDD-PiBMA-1 polymer brush occurs as a single, mass-loss event centered near 330 °C due to the high polymer content of this material. This event parallels that observed for pure PiMBA and is clearly associated with the thermal decomposition of surface-bound PiMBA polymer chains.

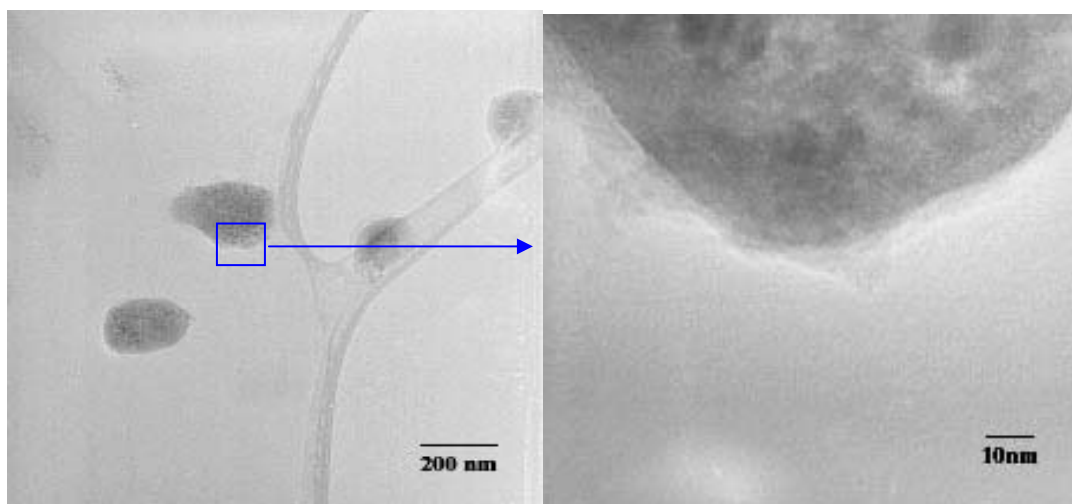


Figure 36. TEM images of UDD-PiBMA-1 sample.

The TEM images of UDD-PiBMA-1 (see Figure 36) reveal a UDD core aggregate feature ca. 100-200 nm diameter grafted by a thin polymer layer. Under high vacuum, the surface-bound polymer chains form condensed topologies due to intermolecular van der Waals interactions.

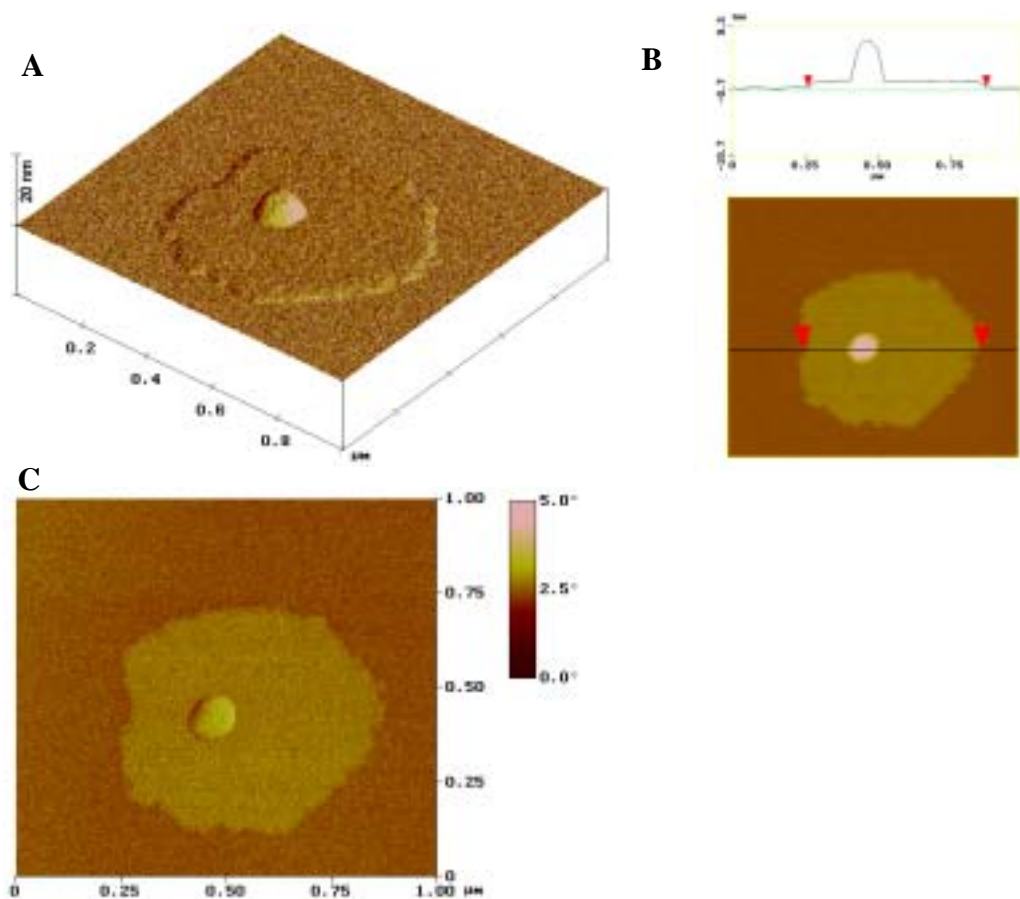


Figure 37. AFM tapping-mode height image (A and B) and phase image (C) of an individual UDD-PiBMA-1 brush as spin-coated onto a mica surface.

AFM tapping mode and phase images of the UDD/polymer brush, UDD-PiBMA-1, are shown in Figure 37. This sample was prepared by spin coating a dilute dispersion of UDD-PiBMA-1 onto a mica surface. It is evident that polymer chains extend outwardly ca. 150-400 nm beyond the surface of a central aggregate about 80 nm in diameter.

Since UDD particles in UDD-polymer brushes are covered by a layer of organic polymer, the specific surface area of UDD-PiBMA-1 is expected to have a lower surface

area than that of as-received UDD. Figure 38 shows a comparison of specific surface area of UDD, UDD-CO₂H, c-UDD-1, and UDD-PiBMA-1 samples. There is a dramatic reduction in specific surface area of UDD-PiBMA-1 compared with those of UDD and UDD-CO₂H. The c-UDD-1 control sample has a slightly smaller specific surface area than that of oxidized UDD, because oligomer radical moieties are attached to UDD surface during the polymerization process, as discussed in Chapter II. However, since the graphene structure in UDD is less than in GCNFs, fewer oligomer fragments are randomly trapped by UDD surface in this control sample causing only a small reduction in specific surface area.

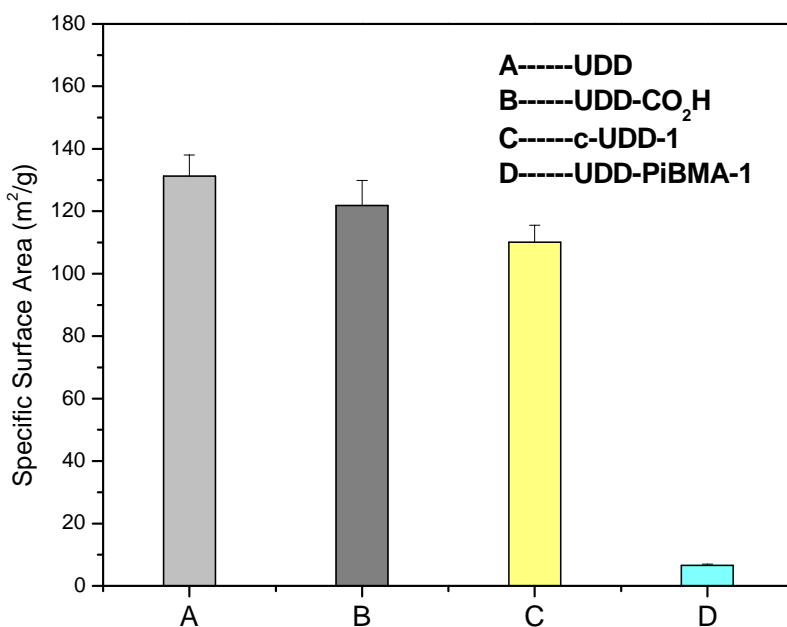


Figure 38. BET analysis of (A) UDD, (B) UDD-CO₂H, (C) c-UDD-1, and UDD-PiBMA-1 samples.

Grafted polymer brushes greatly improve the dispersibility of UDD in weak polar and nonpolar organic solvents. The dispersibility test results shown in Figure 39 reveal that the UDD-PiBMA-1 sample forms stable dispersions in acetone, toluene, and carbon tetrachloride but precipitates out from the polar solvent methanol, a poor solvent for PiBMA polymers. The UDD-PiBMA-1/CCl₄ dispersion starts to separate after 2 weeks of storage at room temperature, whereas the UDD-PiBMA-1/acetone and UDD-PiBMA-1/toluene dispersions remain uniform even after 4 weeks. The dispersibility difference among these solvents is attributed to the different solubility of PiBMA chains in these solvents.

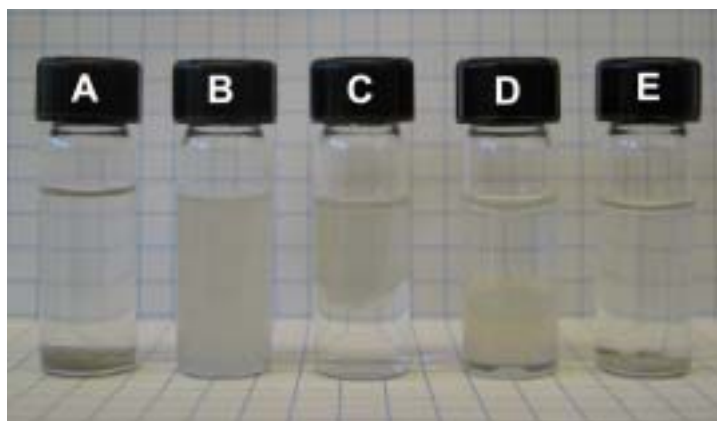


Figure 39. Dispersibility test: (A) UDD in acetone; (B), (C), (D), (E) UDD-PiBMA-1 in acetone, toluene/H₂O, H₂O/CCl₄, and MeOH. Concentration of the dispersions is about 2.5 mg/mL.

UDD-Poly(iso-Butyl Methacrylate) Brushes by UDD-Cl (UDD-PiBMA-2)

The bromine-based UDD-Br initiators are used to initiate *in situ* ATRP of iBMA to

grow PiBMA brushes from the UDD particles surface for synthesis of UDD-PiBMA-1 polymer brushes. However, Matyjaszewski and coworkers⁶⁷ investigated the ATRP of *n*-butyl methacrylate and reported that when EBriB is used as initiator with CuCl/PMDETA catalyst complex, the GPC curves of PnBMA have tailing toward low molecular weight, indicating either notable termination or slow initiation. To overcome this problem, a chlorine-based initiator 2,2,2-trichloroethanol (TCE) was used as a substitute for EBriB. The ATRP of nBMA initiated by TCE with CuBr/PMDETA catalyst complex resulted in better control of polymerization.

To optimize ATRP conditions for the synthesis of UDD-iBMA polymer brushes in this work, TCE is reacted with acylated UDD to form a chlorine-based UDD-Cl initiator. PiBMA brushes are successfully synthesized by *in situ* ATRP of iBMA using UDD-Cl. A control experiment is carried out again to verify that polymer brushes are grown from the surface of UDD instead of being grafted onto the surface by free polymer chains. The reaction conditions are nearly identical to normal ATRP of iBMA except for the presence of as-received UDD. No significant difference is observed in molecular weight and polydispersity between the polymers of PiBMA-2 and of c-PiBMA-2, as shown in Table 9, indicating that the presence of UDD has no distinct effect on ATRP in this system.

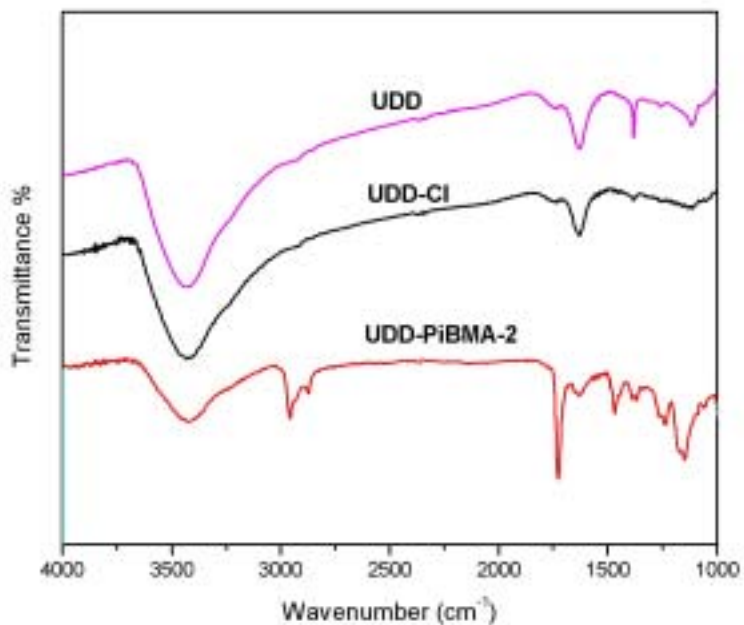


Figure 40. FT-IR spectra of UDD, UDD-Cl, and of UDD-PiBMA-2.

The FT-IR spectrum of UDD-PiBMA-2, as shown in Figure 40, has similar features as that of UDD-PiBMA-1. The distinct C=O stretching band at 1728 cm^{-1} and C-H stretching vibration band at 2956 cm^{-1} and 2872 cm^{-1} originate from the polymer chains in the UDD-PiBMA-2 sample.

TGA mass-loss curves (see Figure 41) show that UDD-Cl has nearly identical profile as as-received UDD because only a small amount of molecules of initiators are bound on the surface which are not able to alter the mass-loss features. On the other hand, the c-UDD-2 sample has a relatively greater mass-loss than as-received UDD due to the oligomer radical moieties trapped by graphitic structures on the surface of UDD during polymerization. A sharp mass-loss in the temperature range of $240\text{ }^{\circ}\text{C}$ - $400\text{ }^{\circ}\text{C}$ in the TGA curve of UDD-PiBMA-2, consistent with major mass-loss of free PiBMA polymers,

originates from the grafted polymer brushes.

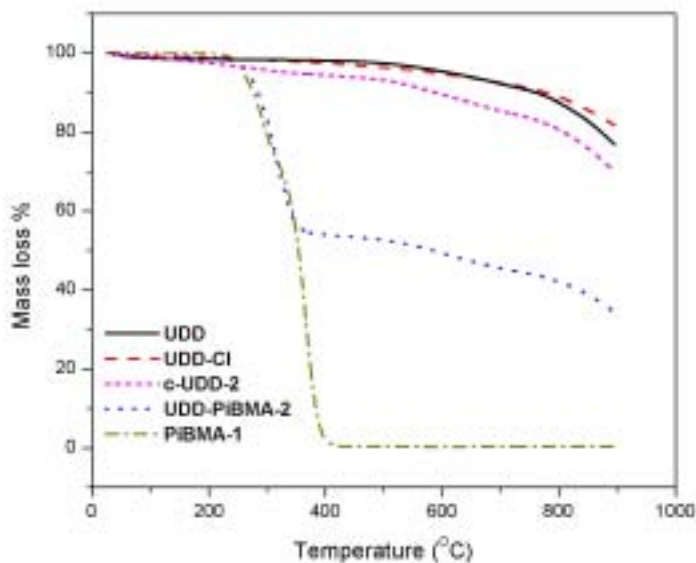


Figure 41. TGA curves of UDD, UDD-Cl, c-UDD-2, UDD-PiBMA-2, and PiBMA-1 samples.

The polymer brush phase of UDD-PiBMA-2 is imaged by tapping-mode AFM, as shown in Figure 42. Two UDD particles with diameters about ca. 50 nm and 100 nm, respectively, are surrounded by polymer chains extending outwardly from the substrate surface as far as about ca. 200 nm. PiBMA molecules cleaved from UDD-PiBMA-2 have a number-average molecular weight of 78,400, which is consistent with the chain lengths of the polymers observed in AFM images. Local-site variations in the rate of ATRP chain growth give a wide distribution of polymer chain length, as evidenced by a polydispersity of 2.47 for polymers cleaved from UDD-PiBMA-2.

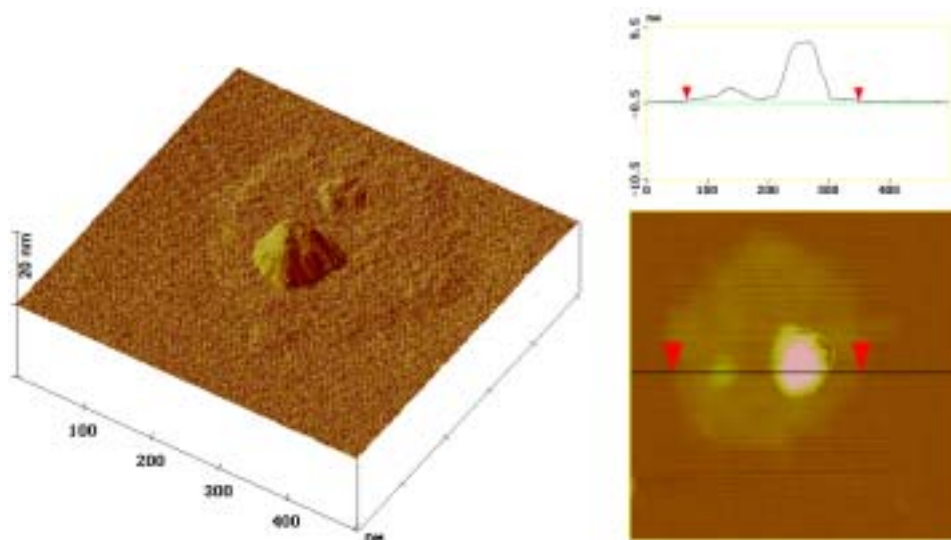


Figure 42. AFM tapping-mode height image (left) and phase image (right) of an individual UDD-PiBMA-2 brush as spin-coated onto a mica surface.

BET analysis results shown in Figure 43 indicate that the presence of polymer brushes in UDD-PiBMA-2 greatly reduces the specific surface area of UDD particles (from ca. 131.22 m²/g to 59.48 m²/g). However, the control sample, c-UDD-2, has a specific surface area ca. 105.73 m²/g, slightly smaller than that of as-received UDD ca. 131.22 m²/g, because the oligomer fragments entrapped by the graphitic structures on the surface of UDD particles during the polymerization can only partially cover the UDD particles surface. From the BET specific surface area of as-received UDD ca. 131.22 m²/g and the average polymer chain content ca. 3.4×10^{18} chains/g determined for UDD-PiBMA-2, a surface density of ca. 5 polymer chains/100 nm² can be calculated.

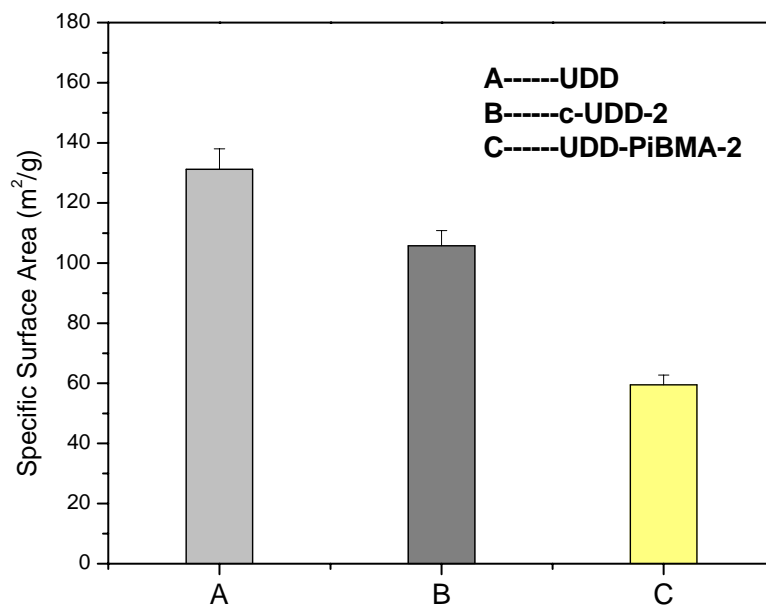


Figure 43. BET analysis of specific surface area of UDD, c-UDD-2, and UDD-PiBMA-2 samples.

Similar to UDD-PiBMA-1, the dispersibility of UDD-PiBMA-2 is significantly improved by surface-grafted polymer brushes. A dispersibility test (see Figure 44) in a series of organic solvents indicates that the UDD-PiBMA-2 sample can be easily dispersed into CCl₄, toluene, and acetone. Only one minute of sonication at room temperature is required to achieve these dispersions. Again, UDD-PiBMA-2 starts to precipitate from the CCl₄ dispersion in 2 weeks at room temperature, while the UDD-PiBMA-2/toluene and UDD-PiBMA-2/acetone dispersions remain uniform even after 4 weeks of storage due to the different solubilities of PiBMA chains in these solvents.

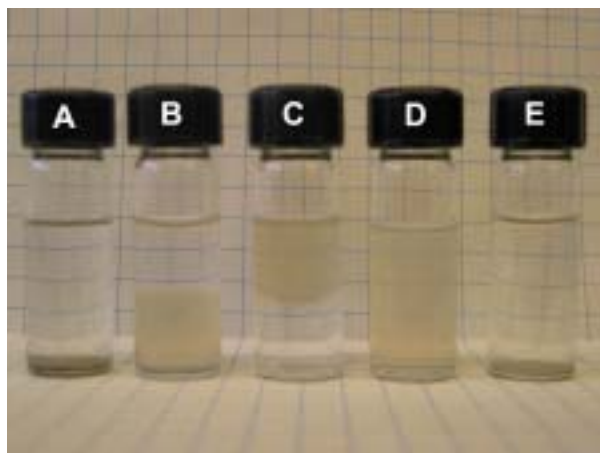


Figure 44. Dispersibility test: (A) UDD in CCl_4 ; (B), (C), (D), (E) UDD-PtBMA-2 in $\text{H}_2\text{O}/\text{CCl}_4$, toluene/ H_2O , acetone, and MeOH. Concentration of the dispersions is about 2.5 mg/mL.

UDD-Poly (tert-Butyl Methacrylate) Brushes (UDD-PtBMA)

As precursors of hydrophilic PMAA brushes, UDD-PtBMA brushes are synthesized by *in situ* ATRP of tBMA initiated with UDD-Cl. For ATRP of tBMA initiated by free TCE in toluene solution at 90 °C, the polymerization rate is fast due to the relatively high temperature.¹⁰⁴ However, polymerization of tBMA initiated by UDD-Cl initiator in 50% toluene solution at 90 °C affords UDD-PtBMA with a polymer content of only 18 wt% along with a great amount of free polymers. These results suggest that many immobilized initiators are cleaved from the surface of UDD particles during polymerization at such a high temperature. A control experiment is carried out to verify that PtBMA chains grow from the surface of UDD particles other than graft onto the surface of UDD particles. The reaction conditions are the same as that of normal ATRP of tBMA except for the

presence of as-received UDD. The resulting polymers and UDD are identified as c-PtBMA and c-UDD-3, respectively. No significant difference in molecular weight and polydispersity between the polymers of PtBMA and c-PtBMA samples is observed (see Table 10), indicating that the presence of UDD has no distinct effect on the features of the ATRP of tBMA in this system. The obtained UDD-PtBMA was hydrolyzed in $\text{CF}_3\text{CO}_2\text{H}$ to prepare hydrophilic UDD-PMAA brushes.

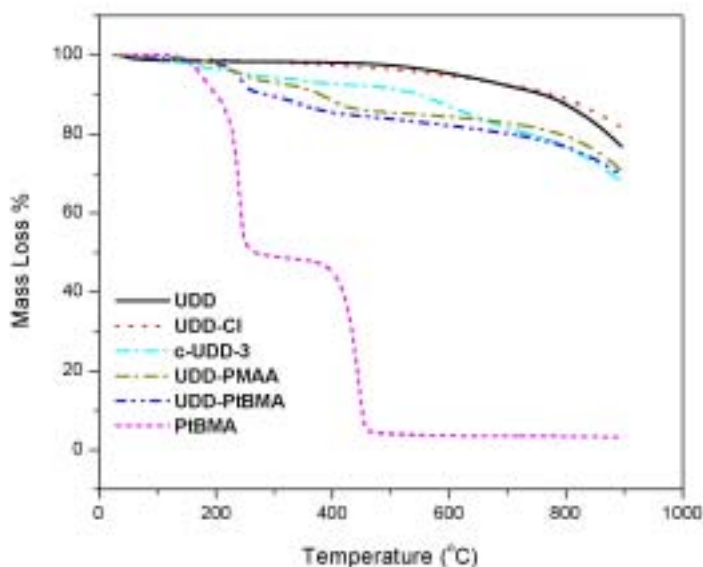


Figure 45. TGA curves of UDD, UDD-Cl, c-UDD-3, UDD-PtBMA, and PtBMA.

As shown in Figure 45, free PtBMA polymers have unique TGA features with two major mass-loss processes: 150 °C - 240 °C and 390 °C - 460 °C, respectively. The first mass-loss event is assigned to the release of tert-butoxy groups, and the second one is attributed to the loss of remaining parts of the polymer chains. Similarly, the sharp mass-loss from 200 °C to 240 °C in the TGA curve of UDD-PtBMA can be assigned to loss of the tert-butoxy groups of the PtBMA brushes, and the gradual mass-loss at the

range of 240 °C - 460 °C is attributed to loss of the remaining backbone atoms of the polymer chains. UDD-PMAA has a similar profile but smaller mass-loss is observed due to the smaller molecular weight of a methacrylic acid unit compared to the mass of a tert-butyl methacrylate unit.

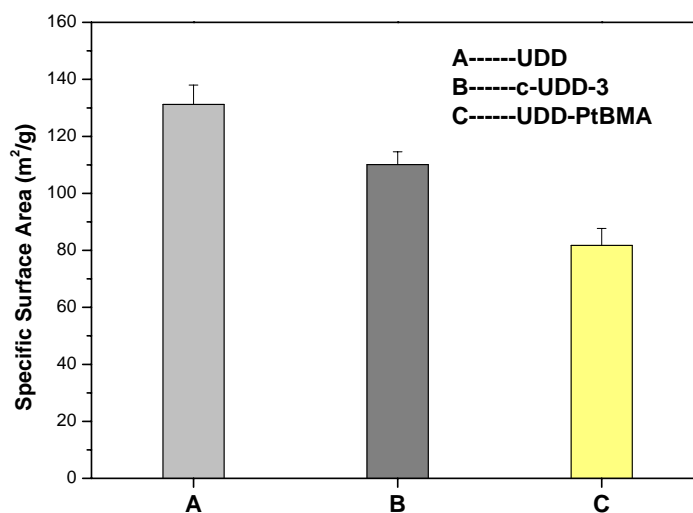


Figure 46. BET analysis of specific surface area of UDD, c-UDD-3, and UDD-PtBMA samples.

BET analysis results (see Figure 46) indicate that the grafted PtBMA brushes reduce the specific surface area of UDD-PtBMA to ca. 81.73 m²/g compared with ca. 131.22 m²/g for as-received UDD, because the rough UDD particles surface is covered by a layer of smooth polymer brushes. The specific surface of c-UDD-3 ca. 110.11 m²/g is also smaller than that of as-received UDD, which is again attributed to the oligomers trapped on the surface of UDD particles during the polymerization.

As shown in Figure 47, the solution dispersibility of UDD/polymer brushes is controlled by the solubility properties of the polymer chains. Hydrophobic UDD-PtBMA has a greatly improved dispersibility in organic solvents, while the hydrophilic UDD-PAA disperses well in water. The excellent dispersibilities of these UDD/polymer brushes are attributed to the high degree of surface derivatization achieved by this synthesis method.

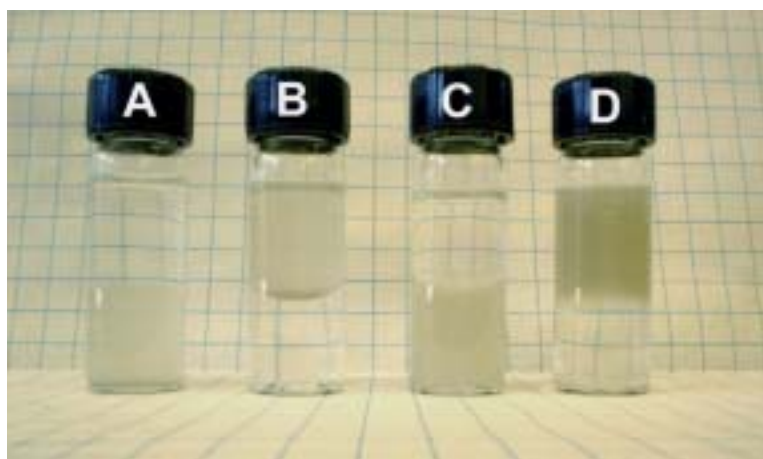


Figure 47. Dispersibilities (ca. 2.5 mg/mL) of the hydrophobic UDD-PtBMA brush, in water(upper)/CHCl₃(lower), vial A, and in toluene(upper)/water(lower), vial B, contrasted with that of the hydrophilic UDD-PMAA brush in toluene(upper)/water(lower), vial C, and in water(upper)/CHCl₃(lower), vial D.

UDD-Poly(Octadecyl Methacrylate) Brushes (UDD-POMA)

Syntheses of well defined homopolymers and copolymers of octadecyl methacrylate (OMA) by ATRP have been reported.^{105,106} Due to the hydrophobic nature of long alkyl side chains in OMA, a nonpolar solvent, *o*-xylene, and a hydrophobically modified

bipyridine ligand, 4,4'-di(5-nonyl)-2,2'-bipyridine, were used to improve the homogeneity of the ATRP reaction mixture. The halogen exchange technique was also used to improve the control of ATRP polymerization. In this work, however, *in situ* ATRP of OMA by UDD-Cl, an efficient initiator for UDD-PiBMA-2, is carried out to grow polymer brushes on the UDD surface with the “grafting-from” method.

Table 12. Experimental conditions of ATRP to prepare UDD-POMA polymer brushes

Sample	[OMA]:[UDD-Cl] ^c	[OMA]:[I] ^d : [L] ^e : [CuCl]:[CuCl ₂]	Time (h)	Polyme r wt% ^f
UDD-POMA-1 ^a	710:1	100:0:1:1:0	24	55
UDD-POMA-2 ^a	710:1	100:0: 1.1:1:0.1	24	65
UDD-POMA-3 ^a	710:1	100:1:1:1:0	24	15
UDD-POMA-4 ^b	710:1	100:0:1:1:0	96	20

a. Reactions were carried out at 90°C in *o*-xylene (50% v/v); b. Reaction was carried out at 90°C in *o*-xylene (27% v/v); c. Molarity of immobilized initiator calculated by (wt UDD-Cl × 0.14 mM/g); d. [I] = TCE; e. [L] = [PMDETA]; f. Obtained from TGA analysis.

As shown in Table 12, ATRP of OMA to form UDD-POMA-1 is performed in *o*-xylene at elevated temperature with CuCl/PMDETA complex as catalyst. For ideal living-brush-growth polymerization, a plot of polymer brush content as a function of polymerization time is linear. However, from the curves plotted in Figure 48, the increase of polymer brush content slows down over time, indicating that the polymer brush growth process is not well controlled. One critical requirement for ATRP is an adequate

concentration of deactivator at the beginning stage of initiation to establish effective exchange equilibrium between reactive radicals and dormant halides. In surface-initiated polymerization, a low concentration of surface-bound initiators limits the creation of sufficient deactivators for polymerization control.⁷²

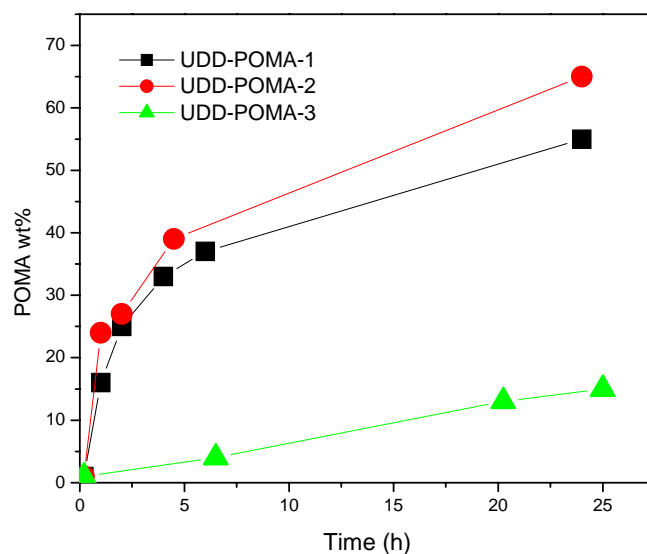


Figure 48. Kinetic plots of polymer brush content versus polymerization time: UDD-POMA-1 (square) [OMA]:[TCE]:[PMDETA]:[CuCl] =100:0:1:1; UDD-POMA-2 (circle) [OMA]:[TCE]:[PMDETA]:[CuCl]:[CuCl₂] =100:0:1.1:1:0.1; UDD-POMA-3 (triangle) [OMA]:[TCE]: [PMDETA]:[CuCl] =100:1:1:1

To suppress this disadvantage, two experiments are conducted to improve control of the surface-initiated ATRP of OMA: (a) an appropriate amount of CuCl₂ is added as deactivator at a concentration of 10 mol% to CuCl (see Table 12, UDD-POMA-2); (b) sacrificial initiator TCE is added and the polymerization is simultaneously initiated by both surface-bound and free initiators (see Table 12, UDD-POMA-3).

Addition of CuCl_2 increases the polymerization rate slightly, but polymerization still occurs with poor control. On the other hand, when sacrificial initiators are added to the polymerization system, polymerization occurs with good control throughout the timescale of the polymerization as the linear shape of the kinetic plot indicates in Figure 48, although the polymerization rate of UDD-POMA-3 is dramatically reduced due to competition between the small amount of surface-bound initiators and the relatively large number of free initiators in solution.

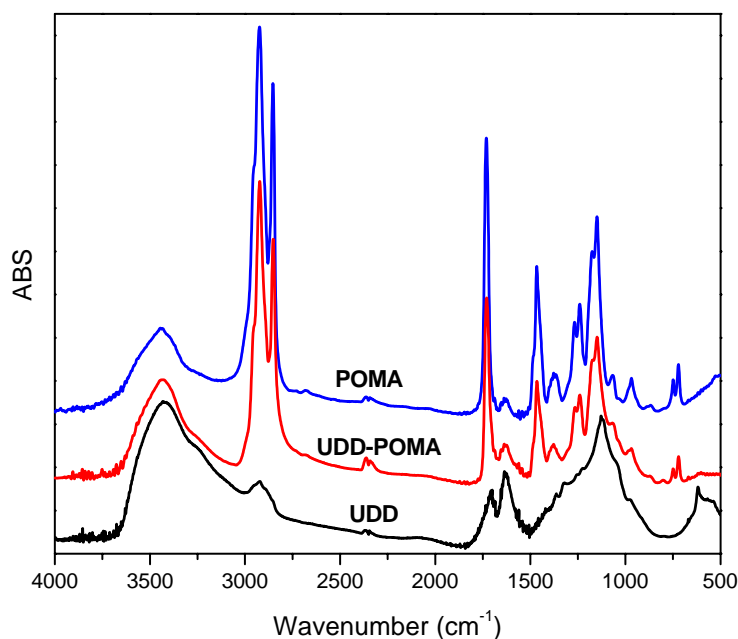


Figure 49. FT-IR spectra of as-received UDD, UDD-POMA polymer brush, and POMA polymer.

To verify that polymer brushes are grafted from UDD surfaces instead of being adsorbed onto the surface by free polymers formed in solution, two control reactions: (1)

OMA monomer with free initiator TCE, and (2) OMA monomer without initiator, in the presence of as-received UDD, are carried out under identical conditions to those used for the preparation of UDD-POMA-1.

No significant polymer brush is observed on the surface of UDD particles as a result of control polymerization (1). Neither polymer brushes nor free polymers are observed from control reaction (2), indicating that the polymer brushes of UDD-POMA-1 are unlikely formed by the grafting of thermally initiated polymers onto the UDD particles surface.

Representative FT-IR spectra of as-received UDD, UDD-POMA polymer brush and free POMA polymer are shown in Figure 49. Broad bands centered at 3450 cm^{-1} and 1737 cm^{-1} in the spectrum of as-received UDD are assigned to hydroxyl, O-H, and carboxyl group, C=O, stretching bands due to the presence of surface CO_2H groups. The FT-IR spectrum of UDD-POMA polymer brush is dominated by bands associated with the polymer chains. An intense peak at 1730 cm^{-1} is assigned to C=O stretching of the ester functional groups within POMA chains. FTIR spectra of UDD-POMA and POMA also show strong bands centered at 2930 cm^{-1} and 2850 cm^{-1} originated from C-H stretching vibrations of the polymer chains.

TGA mass-loss curves of UDD-POMA polymer brush and related intermediate materials are illustrated in Figure 50. UDD-Cl undergoes a gradual ca. 35 wt% mass-loss event from $500\text{ }^\circ\text{C}$ to $900\text{ }^\circ\text{C}$ attributed to decomposition of surface-bound oxyhydrocarbyl groups from CO_2H functional groups and initiator molecules. In contrast,

UDD-POMA-1 possesses a sharp, single mass-loss event from 220 °C to 450 °C due to the grafted polymer content of this material. This event parallels that observed for pure POMA and is obviously associated with the thermal decomposition of surface-grafted POMA polymer chains.

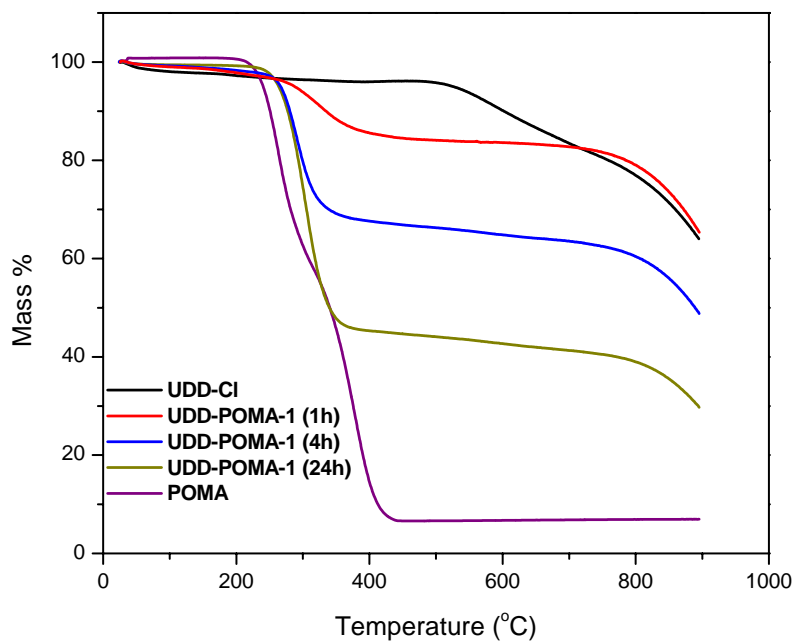


Figure 50. TGA curves of UDD-Cl, UDD-POMA-1 aliquots of 1 h, 4 h, and 24 h, and POMA polymer.

¹H-NMR spectra of UDD-POMA polymer brushes and of POMA pure polymer are shown in Figure 51. Resonances at 0.83 ppm, 1.25 ppm, 1.50 ppm, and 3.85 ppm for the UDD-POMA-1 polymer brush (polymer content = 55 wt%) are readily assigned to the corresponding resonances of the free polymer counterpart with only a small degree of relaxation broadening. However, the UDD-POMA-4 polymer brush with less polymer

content, ca. 20 wt%, has much weaker and broader resonance signals at 0.83 ppm, 1.25 ppm, and 1.50 ppm, and the resonance at 3.85 ppm is absent. These results indicate good extension of the polymer chains into the solution phase can be achieved by increasing the polymer brush content ca. 55 wt%.

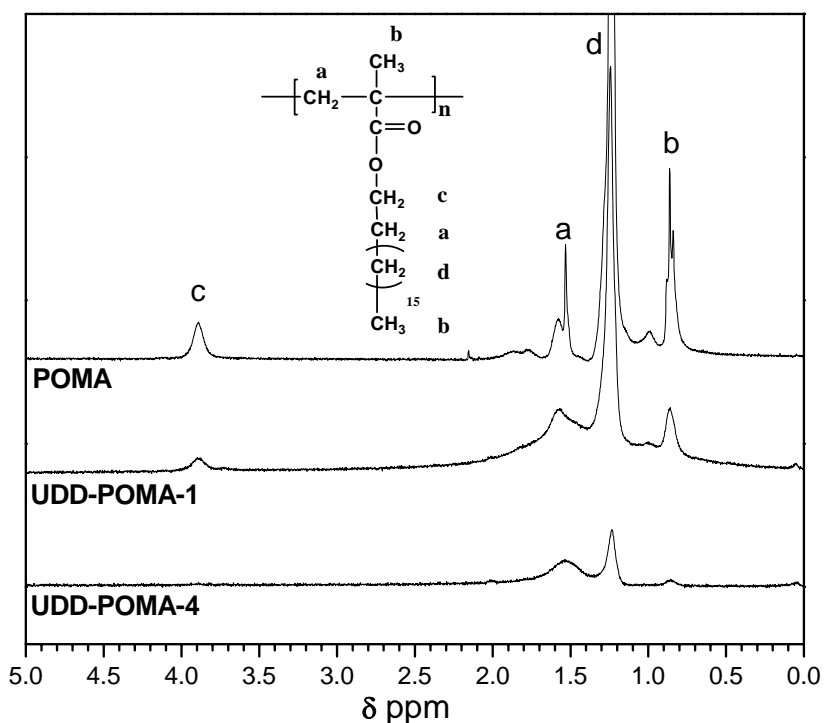


Figure 51. $^1\text{H-NMR}$ spectra of UDD-POMA-4 (polymer content 20 wt%), UDD-POMA-1 (polymer content 55 wt%), and POMA polymer in CDCl_3 .

Direct imaging of a UDD-POMA polymer brushes is obtained by tapping mode AFM. The height and phase images of an individual UDD particle covered by grafted polymer brushes are shown in Figure 52. The centered UDD particle has a diameter about 70 nm,

while the surrounding polymer brush chains extend outwardly by 40 nm to 200 nm, consistent with a broad distribution of chain lengths for the grafted polymer brushes. The broad distribution of polymer brushes could originate from variant local polymerization rate, a result of different local initiator concentration on the UDD particles surface. Similar phenomena are also observed with UDD-PiBMA and UDD-PtBMA brushes, as discussed in previous sections of this chapter.

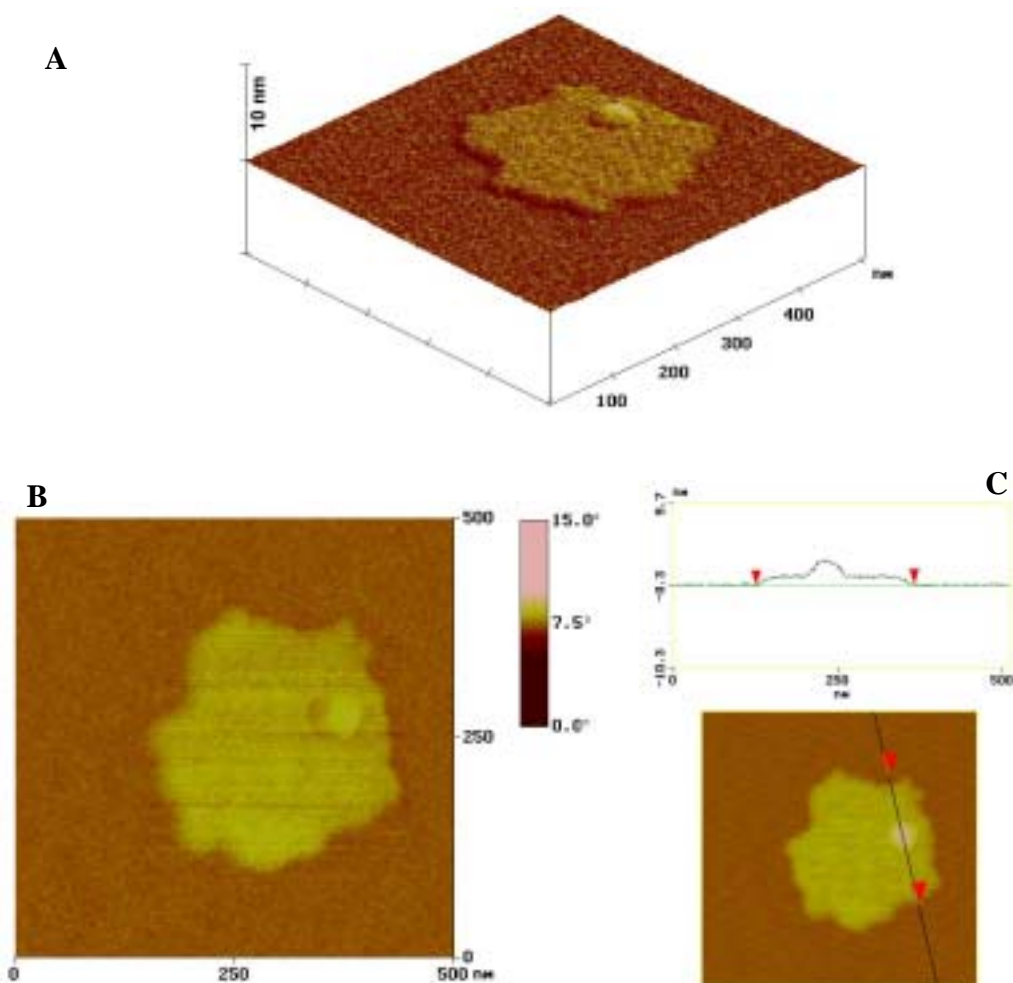


Figure 53. Tapping mode AFM images of UDD-POMA polymer brush spin-coated on a mica surface: A) Height image, B) Phase image, C) Cross-intersectional height profile.

Dispersibility test of UDD-POMA sample in common organic solvents indicates that surface-grafted POMA polymer chains greatly enhance the dispersibility of UDD-POMA compared with that of as-received UDD. In particular, due to the ultra-hydrophobic nature of POMA polymer chains, the UDD-POMA-1 sample can be dispersed into industrial transformer oil to form a relatively stable suspension with the concentration up to ca. 33.5 mg/mL or 1.0% in volume concentration. This dispersion is stable for longer than 1 week before the UDD-POMA particles begin to precipitate. As revealed in the high-resolution optical microscopy images shown in Figure 53, as-received UDD particles precipitate from transformer oil as large aggregates, ca. $>5\ \mu\text{m}$, immediately after sonication, whereas UDD-POMA brushes remain stable as a dispersion. Dispersions of UDD-POMA particles in transformer oil represent nanofluids that have been proposed as a way to enhance the thermal conductivity of such oils.

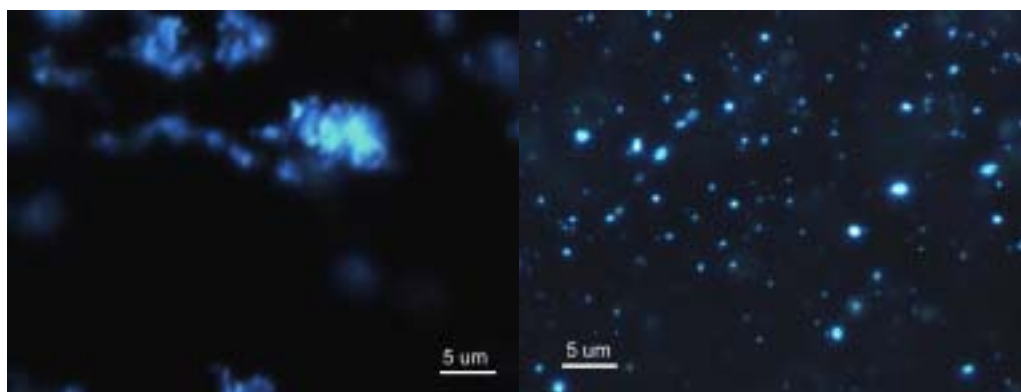


Figure 53. High-resolution optical microscopic images of as-received UDD (left) and UDD-POMA-1 (right) in transformer oil at the concentration of 2.5 mg/mL at room temperature.

UDD-Poly(Glycidyl Methacrylate) Brushes (UDD-PGMA)

Controlled growth of PGMA polymer brushes from the surface of UDD is obtained by using UDD-Cl to carry out *in situ* ATRP of GMA in DPE solution at ambient temperature, with CuBr/PMDETA as catalyst. As shown in Table 13, polymerization with different monomer/initiator and monomer/catalyst ratios is performed to investigate the effect of reaction conditions on the nature of polymer brush growth. As to UDD-PGMA-1 and UDD-PGMA-2, although the monomer/catalyst ratio of the former is twice that of the latter, the resulting polymer brush content of these products are almost the same, ca. 21 wt% for UDD-PGMA-1 and 19 wt% for UDD-PGMA-2. In contrast, polymerization time plays an important role in polymer brush growth. Longer polymerization time affords higher polymer brush content in the final UDD-polymer brush materials (UDD-PGMA-2 and UDD-PGMA-3).

Table 13. Experimental conditions of ATRP to prepare UDD-PGMA brushes

Sample ^a	[GMA]:[UDD-Cl] ^b	[GMA]:[L]:[CuBr]	Time (h)	Polymer wt% ^d
UDD-PGMA-1	2130:1	200 : 1 : 1	24	21
UDD-PGMA-2	2070:1	100 : 1 : 1	24	19
UDD-PGMA-3	1080:1	100 : 1 : 1	120	35

a. All reactions were carried out at 30 °C in DPE (50%, v/v); b. Molarity of immobilized initiator calculated by (wt UDD-Cl × 0.14 mM/g); c. [L] = [PMDETA]; d. Obtained from TGA analysis.

A plot of polymer brush content as a function of polymerization time is shown in Figure 54. Deviation of the plot from linear shape indicates that the growth of polymer brushes from the surface of UDD particles is not a well-controlled ATRP reaction and a higher polydispersity for polymer brush formation is expected. However, growth of polymer brushes with a narrow molecular weight distribution is extremely difficult to achieve with UDD/polymer brushes, because the broad size distribution of as-received UDD particles generates many different local site environments for *in situ* ATRP.

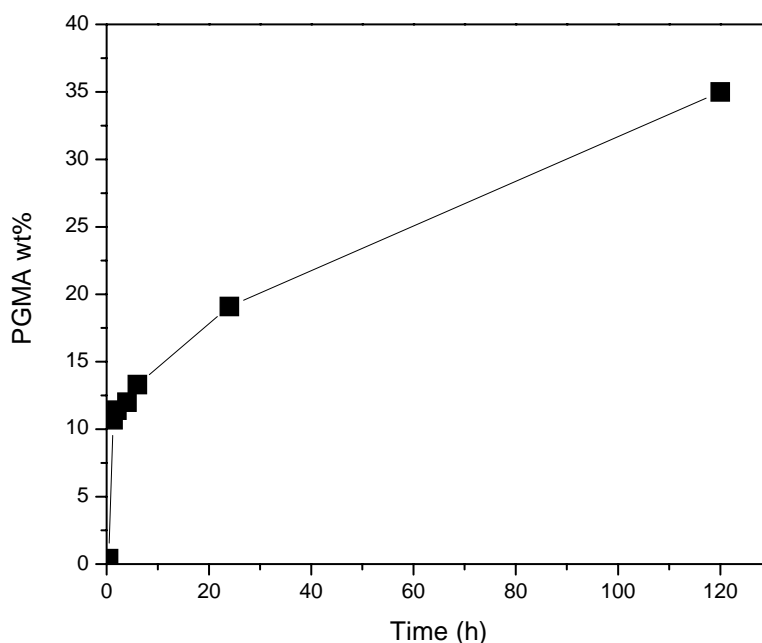


Figure 54. Kinetic plot of polymer brush content versus polymerization time of UDD-PGMA-3 ([GMA]: [PMDETA]:[CuBr]=100:1:1).

Representative FT-IR spectra of as-received UDD, UDD-PGMA polymer brush, and PGMA free polymer are shown in Figure 55. FT-IR spectrum of UDD-PGMA polymer

brush is dominated by bands associated the polymer chains. An intense band at 1730 cm^{-1} is assigned to C=O stretching in the ester functional groups of PGMA chains. FT-IR spectra of UDD-PGMA and PGMA also show a specific epoxide peak centered at 970 cm^{-1} , indicating that the pendant epoxide groups in PGMA chains remain intact under the ATRP conditions.

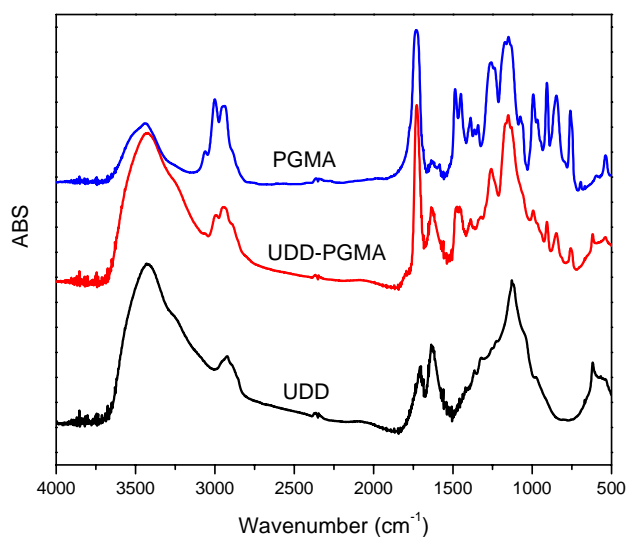


Figure 55. FT-IR spectra of as-received UDD, UDD-PGMA polymer brush, and PGMA polymer.

TGA mass-loss curves of as-received UDD, UDD-PGMA polymer brush, and free PGMA polymers are illustrated in Figure 56. As-received UDD undergoes a gradual 18 wt% mass-loss event from 500 °C to 900 °C attributed to decarboxylation, decarbonylation, and dehydration of surface-bound oxyhydrocarbyl groups, such as CO₂H groups. In contrast, thermal decomposition of the UDD-PGMA polymer brush

samples occurs as a mass-loss event from 100 °C to 450 °C attributed to the grafted polymer brushes. This event parallels that observed for pure PGMA and is clearly associated with the thermal decomposition of surface-grafted PGMA polymer chains. It is notable that longer reaction time results in higher polymer content in UDD-PGMA as ca. 13 wt% of polymer is obtained after 4 h polymerization whereas ca. 35 wt% can be achieved after 24 h.

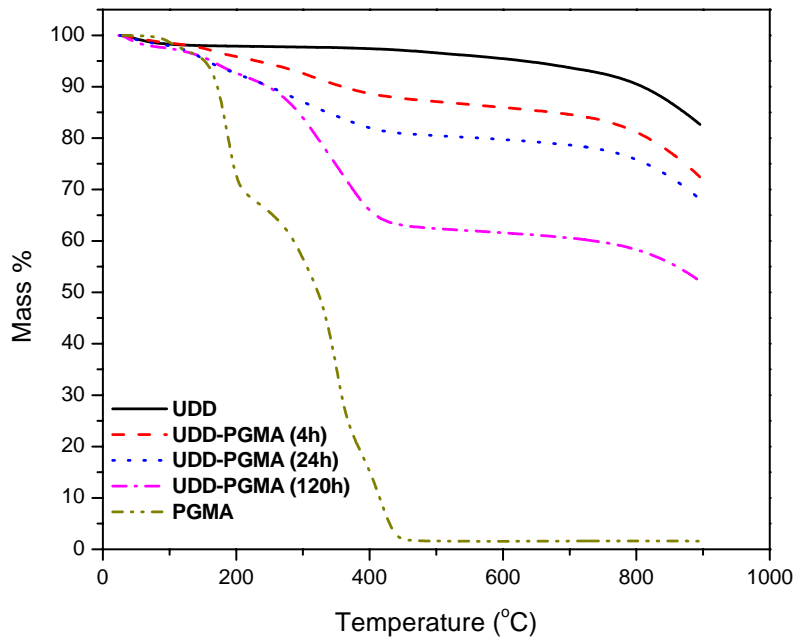


Figure 56. TGA curves of as-received UDD, UDD-PGMA polymer brush samples with different polymerization time of 4 h, 24 h, and 120 h, and PGMA polymer.

Since the rough UDD particles surface of UDD-PGMA is covered by the relatively smooth polymer brush layer, specific surface area of UDD-PGMA should be smaller compared to that of as-received UDD or initiator-bound UDD, UDD-Cl. As shown in

Figure 57, as-received UDD and UDD-Cl have specific surface area ca. 166.2 m²/g and 160.0 m²/g, respectively, while UDD-POMA-1 has a specific surface area only ca. 94.4 m²/g.

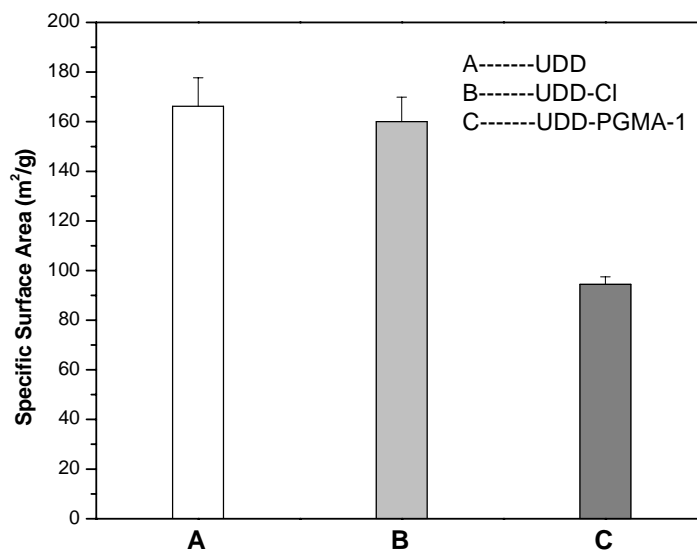


Figure 57. BET analysis of specific surface area of A) as-received UDD, B) UDD-Cl, and C) UDD-PGMA-1 polymer brush.

3.4. Conclusions

The “grafting from” strategy for surface-functionalization of UDD by *in situ* ATRP has been successfully applied to the preparation of UDD/polymer brushes. Two kinds of initiators, bromine-based HEBriB and chlorine-based TCE, are immobilized on the surface of UDD by sequential surface-functionalization of UDD using oxidation, acylation, and esterification reactions. Surface-initiated ATRP of *iso*-butyl methacrylate,

tert-butyl methacrylate, octadecyl methacrylate, and glycidyl methacrylate in solution gives the corresponding UDD-poly(*iso*-butyl methacrylate), UDD-poly(*tert*-butyl methacrylate), UDD-poly(octadecyl methacrylate), and UDD-poly(glycidyl methacrylate) polymer brushes. Chain length of polymer brush can be controlled by changing the conditions of *in situ* ATRP. The UDD/polymer brushes form stable dispersions in non-polar and weak-polar organic solvents, such as chloroform, toluene, and acetone, due to the excellent solubility of grafted polymers in these solvents. Acid hydrolysis of UDD-tBMA polymer brush forms a hydrophilic UDD-poly(methacrylic acid) (UDD-PMAA) polymer brush which has enhanced dispersibility in water.

CHAPTER IV

APPLICATION OF GCNF/POLYMER BRUSHES AS GAS SENSORS

4.1. Introduction

Due to the specific electrical properties and nanoscale diameter, nanocarbon materials, such as CNTs or GCNFs, have been used as electrochemical sensors.^{18,107-109} Gas sensors have been intensely investigated in recent years due to the rapidly increasing concerns about safety and security issues. Gas sensing is commonly evidenced by increased electrical resistance within a detector circuit upon exposure to analyte vapor. Maximum resistance response sensitivities can range from less than 100 % to over five orders of magnitude depending on analyte identity and analyte vapor concentration. A wide variety of carbon nanofiber materials have been recently reported as gas sensors. Among them, bare GCNF arrays prepared via a template synthesis approach are able to absorb large quantities of nitrogen and n-hexane vapor,¹¹⁰ electrodeposited GCNFs thin films on Si(001) substrates can detect methane with 65 % maximum resistance response sensitivity at room temperature,¹¹¹ GCNF/polypyrrole coaxial nanocables fabricated by vapor deposition polymerization of pyrrole on nanofibers detect NH₃ and HCl gases with maximum resistance response sensitivities ranging between 1 and 3.5 for various analyte concentrations,¹¹² GCNF/carbon black/polystyrene thin-film composites detect a variety of organic vapors with high sensitivity,^{113,114} and GCNF/polyester thin-film composites

respond to sensing acetone and methanol vapors with detection sensitivity as high as 1,000 in acetone vapors.¹¹⁵

As discussed in Chapter II, a variety of GCNF/polymer brushes can be synthesized via *in situ* ATRP of (meth)acrylate monomers. Both hydrophobic and hydrophilic GCNF/polymer brushes have now been fabricated as gas sensors to investigate their application for chemical analyte detection. Gas-sensing properties of two GCNF-polymer brushes, GCNF-poly(*n*-butyl acrylate), GCNF-PBA, and GCNF-poly(acrylic acid), GCNF-PAA, along with that of related GCNF materials for comparison were investigated. Thin films of milligram quantities of these GCNF materials were deposited onto a Pt-wire, interdigitated microelectrode (IME) chip by solution coating to construct a sensor circuit having measurable electrical resistance, R_0 . Exposing fabricated GCNF/IME sensors to various analyte vapors increases the circuit resistance, R_v . Maximum GCNF/IME detector response sensitivities, $(R_v - R_0)/R_0$, recorded for a variety of analyte vapors range over five orders of magnitude and are greatest for those vapor/GCNF combinations affording strong van der Waals or hydrogen-bonding interactions. A response sensitivity as large as 2×10^3 is observed for NH_3 vapor detection by GCNF-PAA/IME sensors where strong hydrogen bonding between ammonia molecules and the carboxyl groups of the GCNF-polymer chains is expected. Cycling GCNF/IME sensors between air and analyte vapor atmospheres produces cyclic response curves showing that sensor response times vary from the order of seconds to minutes.

4.2 Experimental Section

Sample Preparation

Comparison materials of amino-functionalized graphitic carbon nanofibers (GCNF-ODA) were prepared as described elsewhere.⁶⁰ Oxidation and acylation of as-received GCNFs were carried out to prepare GCNF-COCl which were then reacted with excess 3,4'-oxydianiline at 100 °C under nitrogen for 96 h. The reaction mixture was cooled to room temperature and washed with ethanol to remove unreacted 3,4'-oxydianiline. The GCNF-ODA product was collected after filtration and dried in vacuum overnight. GCNF-PBA (11 wt% polymer) and GCNF-PAA (22 wt% polymer) polymer brushes were prepared as described in chapter II and isolated as dry, black powders.

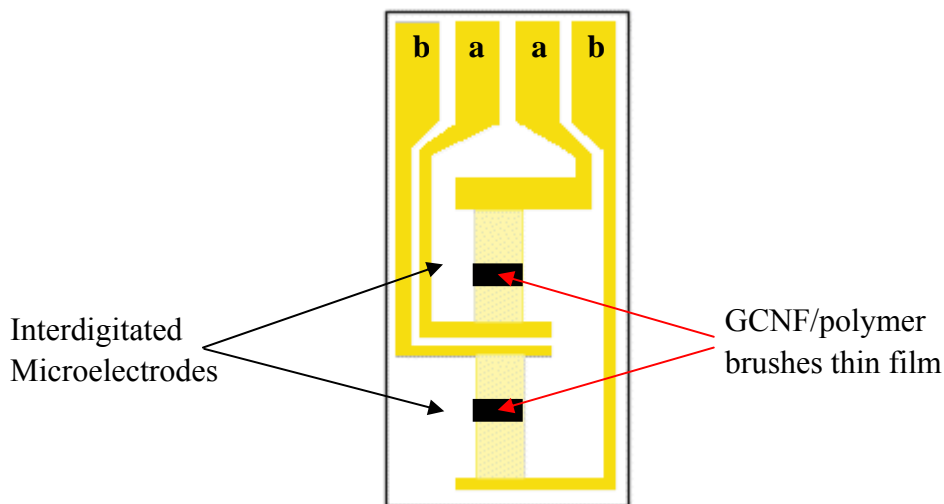


Figure 58. Construction of GCNF/polymer brushes sensors on an interdigitated microelectrode chip (electrode pairs a-a and b-b are connected to multimeter, respectively).

GCNF derivative materials to be tested as gas sensors were dispersed into acetone (or water for GCNF-PAA). The resulting dispersion was dropped onto an interdigitated microelectrode (IME) chip (IME 1525.3 SERIES, ABTECH Scientific, Inc.) constructed of parallel platinum metal lines (15 μm in both digit width and inter-digit spacing) printed on a glass substrate (see Figure 58). Approximately 1-3 mg of GCNF derivative materials was dispersed onto each fabricated IME. IME sensors were dried in air at room temperature for 24 h before electrical resistance measurements were performed.

Gas Sensor Measurements

Electrical resistance measurements were recorded at room temperature between the IME electrode pairs of a-a and b-b as shown in Figure 58, using a digital Fluka True RMS Multimeter. IME circuit resistance increased rapidly when fabricated GCNF/IME sensors were placed into chambers saturated with analyte vapor and abruptly dropped to previous values when removed from analyte vapor and exposed to ambient air atmosphere. Resistance changes were recorded over several cycles of exposure to analyte vapor. Resistance responses were converted to sensor sensitivity values defined as $(R_v - R_0)/R_0$, where R_v and R_0 are measured resistances in the presence and absence of analyte vapor, respectively. Ammonia vapor was generated by a 29 wt% aqueous ammonia solution at room temperature.

4. 3. Results and Discussion

For the two GCNF/polymer brushes used in this study, GCNF-PBA and GCNF-PAA, the polymer chains have an average surface density of ca. 3 polymer chains/10 nm². Similarly, amide coupling of 3, 4'-oxydianiline to surface carboxyl groups present in GCNF-CO₂H nanofibers gives GCNF-ODA nanofibers derivatized with small molecule amino functional groups.⁶⁰ The surface number density of ODA functional groups is ca. 2 molecules/10 nm², comparable to the extent of surface functionalization found in GCNF/polymer brushes.

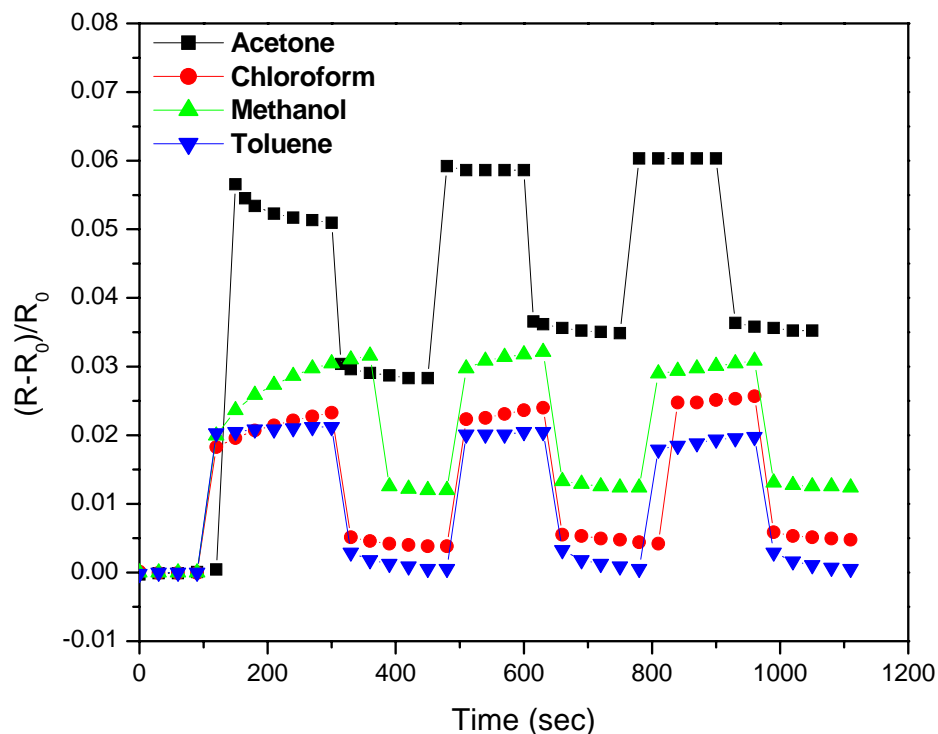


Figure 59. As-prepared GCNF/IME sensor response cycled between ambient atmosphere and acetone, chloroform, methanol, and toluene saturated vapor atmospheres.

As-prepared GCNFs, GCNF-ODA nanofibers, and two GCNF/polymer brushes (GCNF-PBA and GCNF-PAA) have been evaluated as solid-state gas sensors. GCNF/IME sensor circuits are fabricated by depositing GCNF powders onto a Pt-wire IME chip. Sensor response is monitored digitally at room temperature while cycling the GCNF/IME sensor between ambient air and saturated analyte vapor atmospheres in a glass chamber. Gas detection is recorded as an increase in electric resistance of sensor circuits. In related carbon nanotube(CNT)/polymer composite gas sensors, increased electrical resistance upon exposure to analyte vapor has been attributed to matrix-swelling or CNT/analyte charge-transfer mechanisms.¹¹⁶⁻¹¹⁹

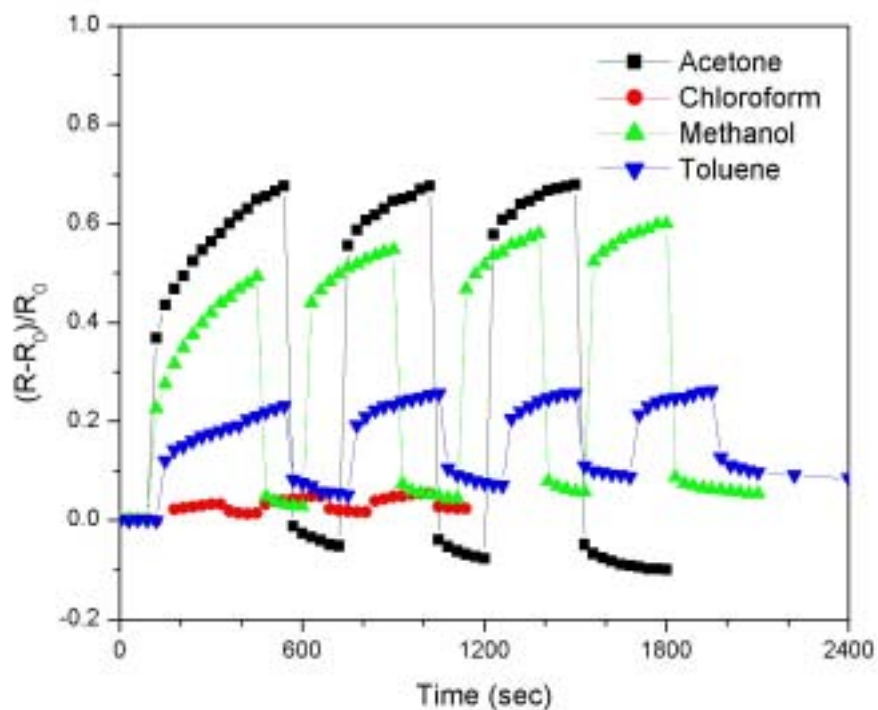


Figure 60. GCNF-ODA/IME sensor response cycled between ambient atmosphere and acetone, chloroform, methanol, and toluene saturated vapor atmospheres.

Resistance response sensitivities of GCNF/IME sensors fabricated with as-prepared GCNF and GCNF-ODA nanofibers in the presence of various analyte vapors are shown in Figure 59 and Figure 60, respectively. Very low sensor response sensitivities (ca. 0.02) are observed for as-prepared GCNFs, but response sensitivities nearly 10 times greater are observed for GCNF-ODA sensors. Presumably, the molecularly derivatized GCNF-ODA surface interacts more strongly with analyte molecules than does an as-prepared GCNF surface attributed to the strong polarity of amine groups in surface ODA molecules. Related carbon nanotube/poly(methyl methacrylate) composite thin-film gas sensors also show higher resistance response sensitivities for composites fabricated with surface-functionalized CNTs compared to those fabricated with as-prepared CNTs.¹²⁰

Table 14. Response sensitivity comparison $(R_v - R_0)/R_0$ of as-prepared GCNF and GCNF-ODA sensors to various organic vapors.

Analyte	Dipole moment, μ (D)	GCNF	GCNF-ODA
Acetone	2.88	0.055	0.8
Methanol	1.74	0.03	0.6
Chloroform	1.04	0.02	0.03
Toluene	0.375	0.02	0.15

As-prepared GCNF/IME and GCNF-ODA/IME sensors both show chemoselectivity in analyte detection. As-prepared GCNFs show greatest sensitivity to acetone vapor ca.

0.055, lower sensitivity to chloroform vapor ca. 0.03, and lowest sensitivity ca. 0.02 to both methanol and toluene vapors for the first cycles. Since herringbone GCNFs possess a long-axis surface dominated by graphite edge sites, the adsorption characteristics of as-prepared GCNFs might be expected to mimic those of a graphite edge surface. Graphite edge surfaces are known to preferentially adsorb molecules of highest dipole moment ¹²¹. The chemoselectivity of as-prepared GCNF gas sensors revealed in Figure 59 follows this same trend. Maximum sensor sensitivity decreases with decreasing gas-phase electric dipole moment of the analyte vapor [acetone (2.88), methanol (1.74), chloroform (1.04), and toluene (0.375)] as shown in Table 14. Especially strong acetone vapor/GCNF surface interactions apparently leads to incomplete desorption of acetone between detection cycles because the sensor sensitivity for as-received GCNFs falls down to around 0.02 after the first cycle.

A similar relationship between sensor chemoselectivity and analyte polarity is observed for GCNF-ODA/IME sensors, except that sensor sensitivity to toluene vapor is greater than that expected relative to the observed response to chloroform vapor. This effect probably results from favorable pi-pi van der Waals interactions between the aromatic rings of toluene analyte and the aromatic rings of surface-bound ODA molecules giving significantly enhanced sensitivity ca. 0.15 to toluene vapor. Lack of both hydrogen bonding and pi-pi interactions with surface-bound ODA molecules, chloroform gives the lowest sensor sensitivity ca. 0.03 for GCNF-ODA/IME sensors.

GCNF/IME sensor response times are quite abrupt and symmetrical for as-prepared

GCNF nanofibers, but more gradual and asymmetrical for GCNF-ODA nanofibers. This observation is consistent with slower analyte vapor adsorption/desorption kinetics expected for a molecularly derivatized nanofiber surface relative to that expected for an as-prepared nanofiber surface.

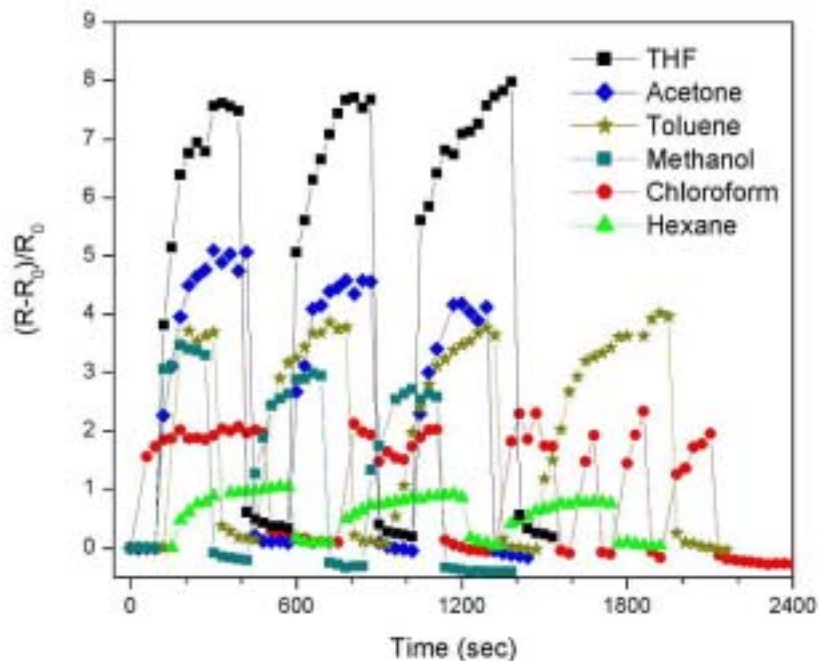


Figure 61. GCNF-PBA/IME sensor response cycled between ambient atmosphere and tetrahydrofuran (THF), acetone, toluene, methanol, chloroform, and hexane saturated vapor atmospheres.

Higher sensor response sensitivities and greater analyte chemoselectivities are observed for organic vapor detection by GCNF-PBA polymer brush sensors as shown in Figure 61. Maximum sensor sensitivities are 10 times greater than those observed for GCNF-ODA nanofiber sensors and nearly 100 times greater than those observed for as-prepared GCNF sensors. Clearly, the presence of a surface-grafted polymer brush

dramatically enhances the chemical sensing properties of GCNFs. Analyte response sensitivities for GCNF-PBA sensors decrease as THF > acetone > toluene > methanol > chloroform > hexane in close correspondence with the known general solubility of pure PBA polymer in these solvents, except for the relative sensitivity to methanol vapor.¹²² Solvent vapors of liquids known to be good solvents of pure PBA have greater tendencies to swell GCNF-PBA polymer chains, thereby increasing the distance between nanofibers forming conductive paths in thin films and consequently increasing detector resistance by greater amounts. Based on solubility parameter concepts,¹²² methanol should be the least swelling vapor of PBA polymer chains within this comparison and, therefore, the gas having the lowest sensor response sensitivity. The observed relatively high sensor response to methanol vapor has not been investigated in detail but could result from strong hydrogen bonding of methanol molecules to a small fraction of surface carboxyl groups that had not been completely derivatized by ATRP initiator molecules. GCNF-PBA/IME sensor response times are quite abrupt for analyte desorption but much longer for analyte absorption, as also observed for GCNF-ODA/IME sensors.

In Figure 62, GCNF-PAA/IME sensors show chemoselectivity and maximum response sensitivities for organic vapor sensing comparable to that observed for GCNF-PBA/IME sensors. Initial-cycle sensor sensitivities decrease as dimethylformamide (DMF)>triethylamine (TEA)>methanol>THF in close correspondence with the known decreasing solubility of pure PAA polymer in these respective solvents.

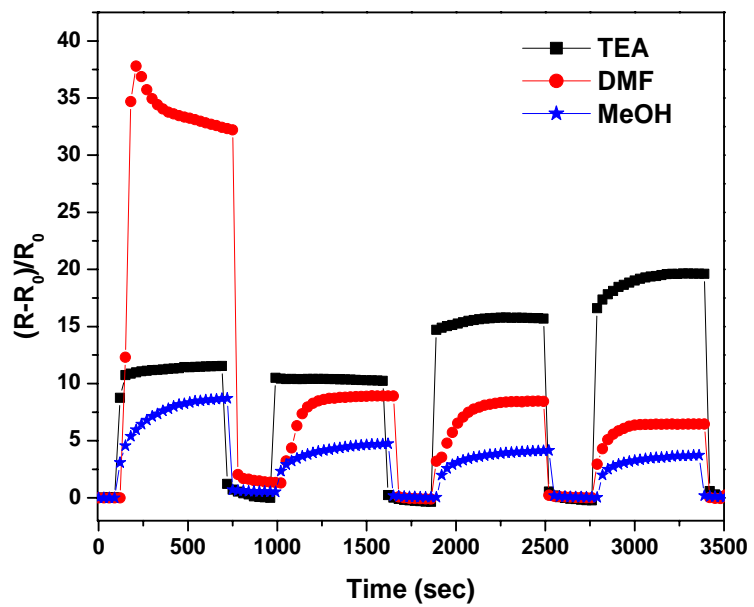
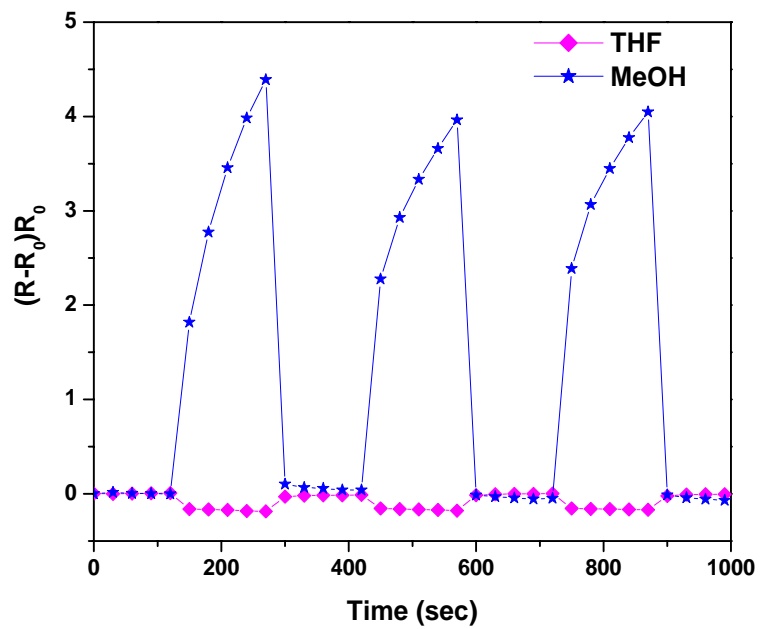


Figure 62. GCNF-PAA/IME sensor response to tetrahydrofuran (THF), methanol, triethylamine (TEA), and dimethylforamide (DMF) saturated vapor atmospheres.

Strong hydrogen bonding interactions between TEA, DMF, and methanol analyte molecules and carboxyl groups present in the PAA polymer brush chains afford large detector responses, while much weaker hydrogen bonding interactions with aprotic THF analyte molecules gives essentially a null response. DMF detection is unique in that initial-cycle maximum sensitivity is ca. three times greater than that measured in subsequent cycles. The origin of this effect has not been investigated but could result from some polymer brush deactivation mechanism.

However, when strong hydrogen-bonding interactions occur between analyte gas and a GCNF sensor material, a greatly enhanced maximum response sensitivity is observed in Figure 63. GCNF-PAA/IME sensing of NH_3 vapor occurs with maximum sensitivity values over 100 times greater than observed for GCNF-PAA sensing of organic solvent vapors and nearly 1,000 times greater than GCNF-PBA/organic vapor sensing. At least two sensing cycles are required to achieve this exceptionally high sensitivity for NH_3 detection, possibly due to some degree of salt formation. It is remarkable that NH_3 desorption occurs so rapidly and completely between each cycle. Similar enhanced sensitivity and sensor cycling characteristics for ammonia detection have been observed for polyaniline thin-film gas sensors.¹²³ The appearance of an unexpected peak in resistance ca. 12 minutes into each sensing cycle is curious. Since the vapor over aqueous ammonia solutions contain both water and ammonia.¹²⁴ this feature might indicate kinetic resolution of both analytes.

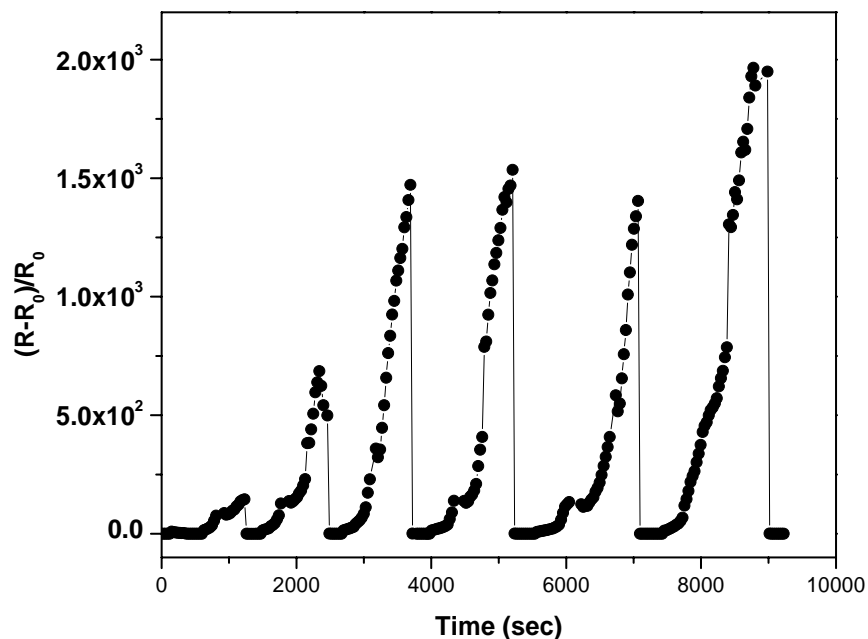


Figure 63. GCNF-PAA sensor response cycled between ambient atmosphere and exposure to NH_3 vapor atmosphere over 29 wt% aqueous ammonia.

4.4. Conclusions

Carbon nanofiber/IME circuits fabricated with as-prepared GCNFs, GCNF-ODA nanofibers, and GCNF-PBA or GCNF-PAA polymer brushes act as solid-state gas sensors showing analyte chemoselectivity and response times ranging from seconds to minutes. Electrical resistance increases upon exposure to analyte vapor with maximum sensor response sensitivities increasing with the expected strength of vapor/GCNF surface van der Waals interaction. Among these GCNF sensor materials, GCNF-polymer brush sensors show maximum response sensitivities to organic vapors 10 times greater than that observed for GCNF-ODA sensors and 100 times greater than that observed for

as-prepared GCNFs, consistent with the expectation that more highly surface-derivatized GCNFs will be more sensitive sensors of analyte gases. Within each type of sensor material, analyte chemoselectivity increases with expected analyte/surface wetting characteristics. GCNF-PAA detection of NH_3 vapor occurs with response sensitivity 1,000 times greater than that observed for GCNF-PBA detection of organic vapors showing that strong analyte/GCNF surface hydrogen bonding interactions give enhanced sensor sensitivity.

By tailoring the chemical composition of GCNF-polymer brushes, the design of detector response sensitivities for specific analyte materials is now feasible, thus permitting development of solid-state, multi-electrode arrays for gas sensing. The presence of a supporting polymer matrix is not required. More sophisticated and sensitive gas sensors can be expected with single GCNF-polymer brush strands fabricated into nanometer-scale devices.

CHAPTER V

APPLICATION OF NANOCARBON/POLYMER HYBRID MATERIALS IN POLYMER COMPOSITES

5.1 . Introduction

Among nanocarbon materials, GCNF nanofibers and UDD particles are very attractive and promising reinforcement materials for the fabrication of composite materials having excellent mechanical properties, such as ultrahigh hardness, strength and stiffness.^{3,125} GCNF nanofibers and UDD particles have been incorporated into a variety of polymer matrices for the purpose of improving mechanical properties.¹²⁶⁻¹³¹ However, the wettability and dispersibility of as-prepared GCNF nanofibers and UDD particles are limited, and spontaneous agglomeration of GCNF nanofibers and UDD particles usually occurs in polymer matrices. Agglomerated GCNF nanofibers and UDD particles are unable to achieve the expected enhancement of polymer properties due to insufficient interaction at the nanocarbon/polymer interface. Therefore, surface-functionalized GCNF nanofibers and UDD particles have been prepared via diverse chemistries and have been applied in various polymer matrices to increase the wettability and dispersibility.^{35,85-87,132-137}

Incorporation of UDD particles in fluoroelastomers, rubbers, and PDMS considerably improves the strength and wear-resistance of resulting composites, although agglomeration is unavoidable in these composites due to the limited dispersibility of

UDD particles without further surface functionalization.¹²⁷ Shenderova et al.¹³⁷ recently reported the fabrication of nanocomposites by incorporating UDD particles, surface-modified by heat treatment in air, into polyimide and PDMS matrices, respectively. The dispersing uniformity of UDD particles increases and so does the thermal degradation temperature as well as the adhesion of these nanocomposites. In this work, the UDD-PGMA polymer brushes discussed in Chapter III are used for the fabrication of epoxy/UDD-PGMA nanocomposites to enhance the mechanical properties of epoxy materials. These UDD-PGMA polymer brushes not only drastically improve the dispersibility of UDD particles in epoxy resins but can also cross link to epoxy resins, through the numerous glycidyl groups along the polymer chains of PGMA brushes, to achieve chemical bonding at the epoxy/UDD interface. The resulting epoxy/UDD-PGMA nanocomposites are expected to have enhanced mechanical properties with uniformly dispersed UDD particles and chemical bonding on the molecular level. The preparation and characterization of epoxy/UDD-PGMA nanocomposites is presented in this chapter.

GCNF nanofibers surface-functionalized with organic molecules bearing pendant primary amino functional groups, such as GCNF-hexanediamine (GCNF-HAD) and GCNF-oxydianiline (GCNF-ODA), have been successfully incorporated into polyimide and epoxy matrices.^{35,85-87,133-135} Epoxy/GCNF-HDA composites show enhancement in flexural properties at as low as 0.3 wt% nanofiber loading with good dispersion of nanofibers achieved in these composites.⁸⁵ With GCNF-ODA nanofibers reactivated by coupling with butyl glycidyl ether to form mono-, di-, tri-, and tetra-glycidyl oligomers

(r-GCNF-ODA), epoxy/r-GCNF-ODA nanocomposites exhibit significantly higher flexural strength than that of pure epoxy materials.^{86,133} At 0.50 wt% r-GCNF-ODA loading, the flexural toughness is improved by ca. 40 % compared with that of the epoxy counterparts. At 0.30 wt% of r-GCNF-ODA loading, storage modulus and loss modulus increase by ca. 122 % and 111 %, respectively.

Epoxy resins are widely used as adhesives in which strong cohesion is critical to prevent debonding at the adhesive/substrate interface. Zhong et al.¹³⁶ reported the adhesion study of epoxy/r-GCNF-ODA composites on high molecular weight polyethylene surfaces and the interfacial debonding energy increases by ca. 27 % as compared to pure epoxy composites. Preparation and selected characterization of epoxy/r-GCNF-ODA adhesives for poly (methyl methacrylate) (PMMA) and aluminum (Al) substrates are presented in this chapter. PMMA-PMMA and Al-Al joints bonded by epoxy/r-GCNF-ODA nanocomposite adhesives are fabricated and shear strength and tensile strength are evaluated as a function of r-GCNF-ODA loading in the epoxy/r-GCNF-ODA nanocomposite adhesives.

5.2. Experimental Section

Materials

UDD-PGMA (30 wt% polymer content) was prepared according to the procedure described in Chapter III. 3,4'-oxydianiline (ODA, 97%), butyl glycidyl ether (BGE, 95%), 1-(2-aminoethyl)-piperazine (AEP, 99%), boron trifluoride ethylamine complex

(BF₃·MEA) and 3-aminopropyltriethyl silane (99%) were purchased from Aldrich and used as received. Commercial epoxy resin EPON 828 was obtained from Miller Stephenson Chemical Co., and D.E.R. 331 and D.E.R. 736 were obtained from Dow Chemical Co., respectively. Solvents were distilled before use and other reagents were used without further purification.

Instruments and Measurements

A Digital Sonifier® 450 (Branson Ultrasonics Co.) was used to cut the length of GCNF nanofibers. A Bransonic® Ultrasonic Cleaner 1210 (Branson Ultrasonics Co.) was used to disperse GCNF nanofibers and UDD particles into epoxy resins. Poly (methyl methacrylate) (PMMA) and Aluminum (Al) specimens (19.12 × 38.04 × 5.56 mm, cross-section 5.56 × 11.84 mm) and the steel fixture were provided by Professor L. Roy Xu in Department of Civil and Environment Engineering at Vanderbilt University. Shear strength and tensile strength test were carried out on a MTS 880 testing machine at 1.0 mm/min loading rate. Rockwell hardness was measured on an Instron Rockwell Hardness testing machine set to the Rockwell E scale.

Fabrication of Epoxy / UDD-PGMA Epoxy Nanocomposites

For a typical fabrication process, 2.0 g BF₃·MEA was dissolved in 20.0 g EPON 828 epoxy resin at 80 °C within a 100-mL beaker. UDD-PGMA (4.15 g) and butyl glycidyl ether (10.0 g) were added into a 50-mL beaker and sonicated for 1 h to form a uniform dispersion. The UDD-PGMA dispersion was then filtered through a 50 mesh copper gauze directly into the above epoxy resin beaker and sonicated for 1 h. The resulting

mixture was poured into a mold (preheated in a vacuum oven at 50 °C) and degassed in vacuum for 1 h. After releasing the vacuum to atmospheric pressure, oven temperature was raised to 120 °C for 1 h followed by 170 °C for 4 h to cure the nanocomposites.

Preparation of Shortened Reactive GCNF-ODA (r-GCNF-ODA)

GCNF-ODA nanofibers were prepared as described in Chapter IV. To improve dispersibility and reactivity in the epoxy resin matrix, as-prepared GCNF-ODA nanofibers were cut in length by ultrasonication using the Digital Sonifier® 450 at a power level of 70 watts for 1 h. An epoxy diluent reagent, butyl glycidyl ether, was used as dispersant for this cutting procedure. The resulting nanofiber/diluent blend was stored in a sealed vessel for 30 h at room temperature followed by vacuum drying at 100 °C for 2 days to obtain dried r-GCNF-ODA nanofibers.

Fabrication of PMMA-PMMA Joints with Epoxy/r-GCNF-ODA Nanocomposite Adhesives

For a typical procedure, 0.6 g D.E.R.736 resin and 24.4 mg r-GCNFs-ODA were mixed by sonification using a Branson® Ultrasonic Cleaner 1210 for 30 min at room temperature. D.E.R. 331 (1.4 g) was then added in the mixture followed by sonication for another 30 min at room temperature. The mixture was vacuum degassed for 1 h at 40 °C to remove air bubbles. Then 0.456 g AEP was added into the mixture and stirred thoroughly before vacuum degassing at 40 °C for 20 min. The degassed mixture was applied onto the contact surfaces of two PMMA specimens which were then affixed into a fixture to form a PMMA-PMMA joint. These joints were cured at 60 °C overnight and

stored at room temperature for one week before the shear and tensile strength test was performed.

Fabrication of Al-Al Joints with Epoxy/r-GCNF-ODA Composite Adhesives

Surface treatment of aluminum specimens was carried out to increase bonding of the metal-adhesive interface. Aluminum specimens were degreased in acetone by sonication for 10 min and then were immediately dipped into a 1 M NaOH solution for 1 min. The resulting aluminum specimens were then surface-functionalized by dipping into a 3 % 3-aminopropyltriethoxyl silane solution for 15 min followed by drying in an oven at 110 °C for 1 h.

For a typical procedure for fabricating Al-Al joints, EPON 828 epoxy resin (1.00 g) and curing agent $\text{BF}_3 \cdot \text{MEA}$ (0.0275 g) were mixed at 80 °C. The r-GCNF-ODA (75.6 mg) was added into the epoxy resin followed by sonification at 60 °C for 1 h. The mixture was degassed in vacuum at 80 °C for 1 h to remove air bubbles and then applied onto the contact surfaces of preheated Al specimens. The Al-Al joints were affixed into the fixture and were cured with a sequential temperature program: 120 °C for 1 h → 160 °C for 1 h → 170 °C for 2 h. The cured joints were stored at room temperature for one week before shear and tensile strength tests.

5.3. Results and Discussion

Epoxy/UDD-PGMA Nanocomposites

Addition of UDD particles to polymers has been reported to give slight enhancement

of mechanical, surface and thermal stability properties.^{125,126} It is proposed that the presence of UDD particles in a composite generates a polymer/UDD interface which restricts the conformation and mobility of polymer molecules that reside near the added UDD particles, and consequently influences the mechanical strength and thermal transitions of the resulting polymer composite.³ According to this explanation, well-dispersed UDD particles will have a better chance to affect the properties of polymer matrices compared with agglomerated UDD particles, because larger interface area can be obtained and thus more polymer molecules in the polymer matrix are mobility and conformation-confined. For the epoxy/UDD-PGMA nanocomposites fabricated in this work, covalent chemical bonding between polymer brushes grafted from UDD particles and polymer molecules of epoxy matrix is also expected to contribute to the enhancement of mechanical properties.

Table 15. Composite specimens with different reinforcement materials incorporated.

Specimen	Materials	Reinforcement Loading
PE-1	Pure epoxy	0 wt%
CB-1	Epoxy/carbon black	1.23 wt%
PB-1	Epoxy/as-received UDD	1.23 wt%
NC-1	Epoxy/UDD-PGMA	1.23 wt%

As shown in Table 15, composite specimens of pure epoxy (PE-1), epoxy/carbon black (CB-1), epoxy/as-received UDD (PB-1), and epoxy/UDD-PGMA (NC-1) were fabricated by casting epoxy resin dispersions of corresponding reinforcement materials into a 10 cm×10 cm×1 cm mold followed by a complete thermal curing at high temperature. Identical fabrication conditions and reinforcement materials loading of 1.23 wt% were used to compare the influence of different reinforcement materials on physical properties of these composites.

Hardness is one of the important mechanical properties for engineering materials especially for surface coatings. A variety of reinforcement materials have been incorporated in polymer matrices to improve the hardness and wear-resistance of resulting composites.³ In this work, hardness enhancement is evaluated as a direct verification of the advantage of UDD-PGMA over other reinforcement materials used to fabricate epoxy composites. An Instron Rockwell Hardness testing machine was used to conduct hardness measurement of the composite specimens and the test results are shown in Figure 64. The carbon black incorporated composite (CB-1) shows lower hardness ca. 10.4 than the pure epoxy specimen ca. 14.7. The decrease of hardness in CB-1 could be attributed to the low hardness and also the large size of carbon black particles used in the composite. As-received UDD does harden the epoxy matrix by increasing the hardness of epoxy/UDD composites to ca. 20.3 due to the ultra-high hardness of diamond structures. With the same UDD loading of 1.23 wt%, however, epoxy/UDD-PGMA nanocomposites have an average hardness of ca. 24, about 20 % higher than that of the epoxy/UDD

composites. This greater hardness enhancement of UDD-PGMA over as-received UDD can be attributed to the dispersing uniformity difference between the two reinforcement materials in NC-1 and PB-1, respectively.

Optical images in Figure 65 illustrate that agglomeration of as-received UDD particles at 1.23 wt% loading induces macrophase separation in the specimen of PB-1 due to their limited dispersibility in epoxy resin. In contrast, the epoxy/UDD-PGMA specimen of NC-1 with the same UDD loading shows comparable uniformity with the pure epoxy specimen of PE-1, indicating that UDD particles are well-dispersed in epoxy matrix with the help of polymer brushes grafted from the UDD particle surface.

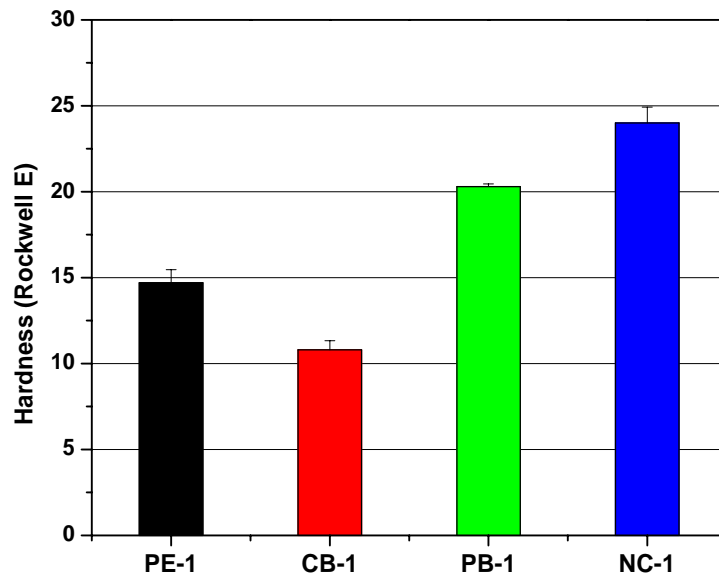


Figure 64. Rockwell E hardness of composite specimens of PE-1 (pure epoxy), CB-1 (epoxy/carbon black), PB-1 (epoxy/UDD), and NC-1 (epoxy/UDD-PGMA).

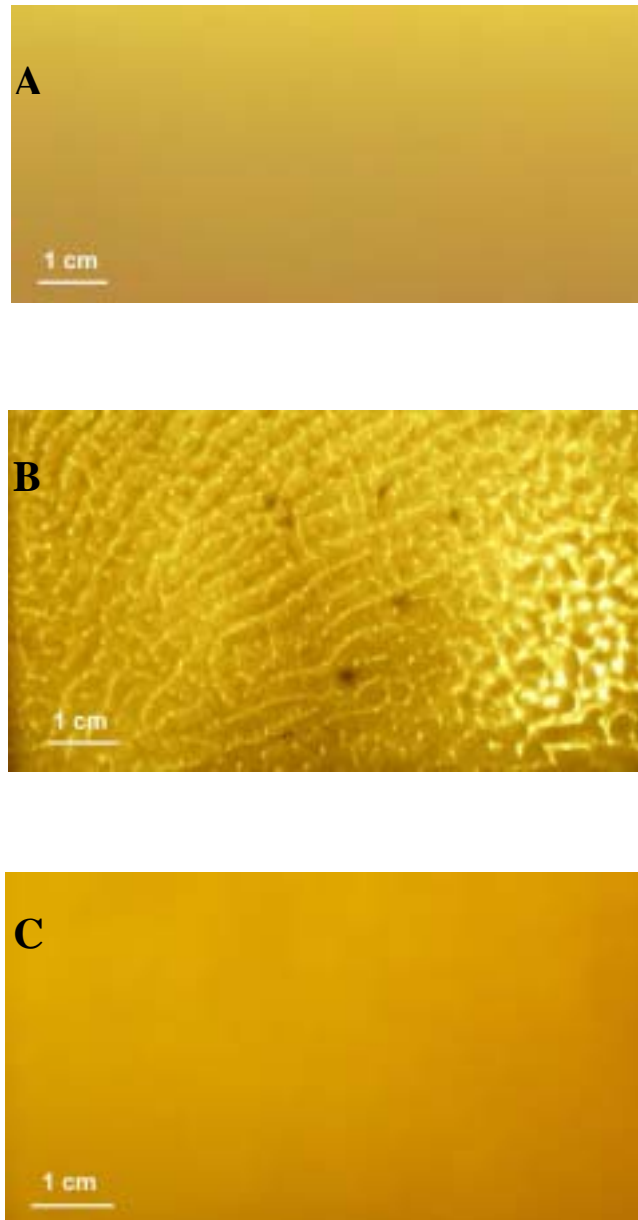


Figure 65. Optical images of composite specimens of A) PE-1 (pure epoxy), B) PB-1 (epoxy/UDD), and C) NC-1 (epoxy/UDD-PGMA).

A series of epoxy/UDD-PGMA nanocomposites were fabricated to study the effect of UDD-PGMA loading on the mechanical property reinforcement to epoxy matrices. As

shown in Table 16, UDD loadings increase from ca. 1.23 wt % for NC-1 to ca. 13.70 wt% for NC-4. All the nanocomposite specimens have similar uniformity as do the NC-1 nanocomposites and no obvious macrophase separation observed in optical images of these nanocomposites.

Table 16. Epoxy/UDD-PGMA nanocomposite specimens with different UDD loading

Specimen	NC-1	NC-2	NC-3	NC-4
UDD loading	1.23 wt%	5.73 wt%	10.46 wt%	13.70 wt%
Hardness	24	25.9	39.9	51.4

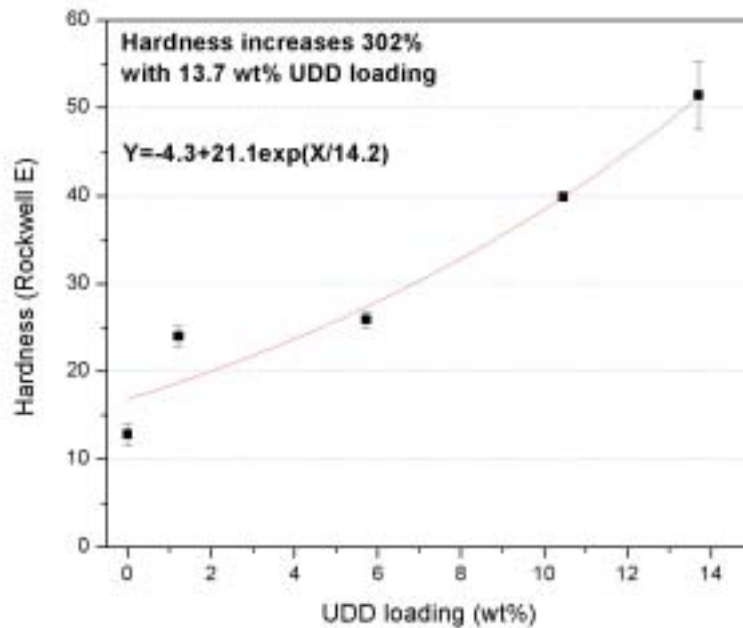


Figure 66. Rockwell E hardness of epoxy/UDD-PGMA nanocomposites as a function of UDD loading.

Hardness measurement was performed to these epoxy/UDD-PGMA nanocomposites for reinforcement effect evaluation. Figure 66 shows an exponential increase of Rockwell E hardness for the epoxy/UDD-PGMA nanocomposites as UDD loading increases. The highest value of hardness ca. 51.4 is achieved at 13.7 wt% UDD loading, about 302 % enhancement over the pure epoxy with hardness of ca. 12.8. Based on the hardness data in this work, it is reasonable to predict that UDD-PGMA polymer brushes can significantly improve mechanical properties of epoxy as structural and engineering polymers when incorporated in polymer matrices as reinforcement materials, given the high UDD loadings and good dispersing uniformity of UDD particles that can be achieved in the nanocomposites. Tensile and impact strength enhancements to epoxy/UDD-PGMA nanocomposites are under investigation in our lab to complete the study on UDD-PGMA polymer brushes as reinforcement materials in polymer matrices.

Epoxy/GCNF-ODA Nanocomposite Adhesives

Two types of substrate materials, PMMA and Al, are used to fabricate testing joints for low-temperature and high-temperature curing epoxy resin systems, respectively. PMMA specimens are bonded with a low-temperature curing epoxy mixture of D.E.R. 736/ D.E.R. 331 while Al joints are fabricated with a high-temperature curing epoxy EPON 828. As shown in Figure 67, the substrate joints fabricated by bonding two specimens together with epoxy/r-GCNF-ODA nanocomposite adhesives have construction dimensions of 19.12 mm (width) \times 38.04 mm (length) \times 5.56 mm (thickness) and a cross section of 11.84 mm (width) \times 5.56 mm (width). The specific design of the

joint shape is to ensure the fracture developing and propagating through the interface of two specimens. The iosipescu shear test and butt-joint tensile test used in this study are practical test methods to obtain the shear strength and tensile strength of a joint of two specimens fixed together by adhesives binding.

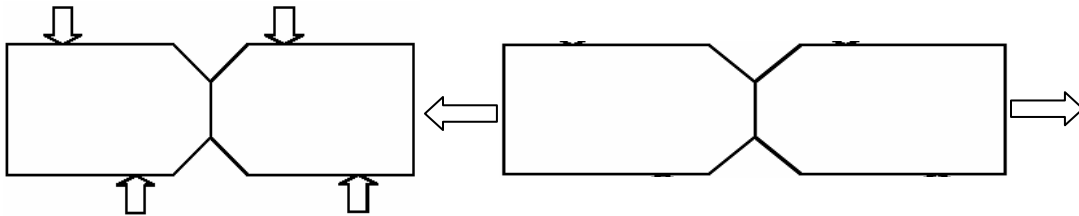


Figure 67. Iosipescu shear test (left) and Butt-joint tensile test (right) joints

PMMA-PMMA joints are fabricated by binding two identical PMMA specimens together with the low-temperature curing epoxy/r-GCNF-ODA nanocomposite adhesives of D.E.R. 736/ D.E.R. 331 (3/7 wt/wt) blend. Curing agent 1-(2-aminoethyl)-piperazine (AEP) is used to cure the nanocomposites at 60 °C. Before the curing process, it is important to remove air bubbles entrapped in epoxy/r-GCNF-ODA blend under vacuum degassing at 40°C for sufficient time. Appropriate degassing temperature is critical to lower the viscosity of the blend for complete removing of all air bubbles while limiting the curing reaction during degassing process.

A series of PMMA-PMMA joints with r-GCNF-ODA nanofibers loading from 0.0 v% to 1.32 v% in the nanocomposite adhesives are fabricated with 3-5 joints for each loading under identical processing conditions. The shear test is carried out on a MTS 880

testing machine at the loading rate of 1 mm/min at least one week after the joints are fabricated to allow the complete curing of nanocomposite adhesives. Figure 68 shows the shear strength of these PMMA-PMMA joints with different r-GCNF-ODA loadings in the epoxy/r-GCNF-ODA nanocomposite adhesives. It is notable that epoxy/r-GCNF-ODA nanocomposite adhesives with r-GCNF-ODA loading at 0.34 v% and 0.64 v% have lower shear strength ca. 16.37 MPa and 17.52 MPa, respectively, as compared to pure epoxy adhesive (ca. 24.38 MPa). However, there is a trend that shear strength of epoxy/r-GCNF-ODA nanocomposite adhesives increases as the r-GCNF-ODA loading is raised from 0.34 v% to 1.32 v%. At 0.88 v% loading, the epoxy/r-GCNF-ODA nanocomposite adhesives have comparable shear strength ca. 24.43 MPa to pure epoxy adhesives. When the r-GCNF-ODA loading increases to 1.32 v%, the highest shear strength ca. 33.98 MPa, a 39 % enhancement over pure epoxy adhesives, is obtained for the epoxy/r-GCNF-ODA nanocomposite adhesives.

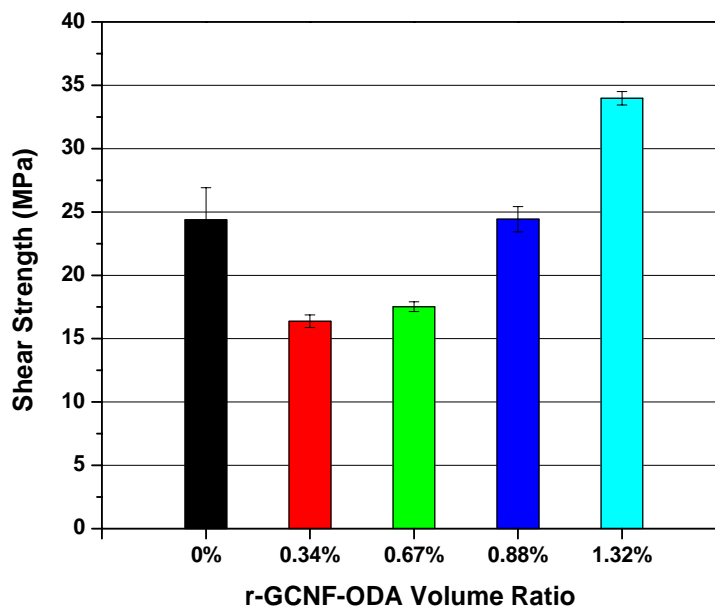


Figure 68. Shear strength of a series of PMMA-PMMA joints bonded by epoxy/r-GCNF-ODA nanocomposite adhesives with different r-GCNF-ODA loading

Tensile strength of the PMMA-PMMA joints is measured using butt-joint tensile test mode on the same MTS 880 testing machine at the loading rate of 1 mm/min. As shown in Figure 69, variable tensile strength enhancements are obtained with the r-GCNF-ODA loading in the nanocomposite adhesives ranging from 0.34 v% to 1.32 v%, consistent with the shear strength test results discussed above. The highest tensile strength ca. 13.6 MPa, a 33% increase compared to pure epoxy adhesives of ca. 10.2 MPa, among the nanocomposite adhesives is achieved by the lowest r-GCNF-ODA loading of 0.34 v%. The unexpected loss of shear strength and low enhancement of tensile strength in some of the epoxy/r-GCNF-ODA nanocomposite adhesives could be attributed to the

agglomeration of r-GCNF-ODA nanofibers formed during the joint fabrication, due to the insufficient dispersibility of r-GCNF-ODA nanofibers in the epoxy matrix and the relatively high viscosity of the epoxy resin blend at the processing temperature of 40 °C.

Although r-GCNF-ODA nanofibers have improved dispersibility, it has been revealed that agglomeration occurs even in the butyl glycidol ether dispersion in which the r-GCNF-ODA is prepared.¹³⁶ Therefore, more dispersible nanofibers are preferred in fabricating epoxy/nanofiber nanocomposite adhesives to achieve a more well-dispersed mixture during the fabrication process. GCNF-PGMA polymer brushes as reinforcement additives in epoxy/nanofiber nanocomposite adhesives are now under investigation in our lab. On the other hand, proper processing techniques are also critical in dispersing nanofibers into epoxy resins. High shear mixer, three-mill mixer, and screw extruder are effective mixing techniques for high viscosity polymer blends and could significantly improve the uniformity of epoxy/nanofiber mixture when combined with sonication treatment.

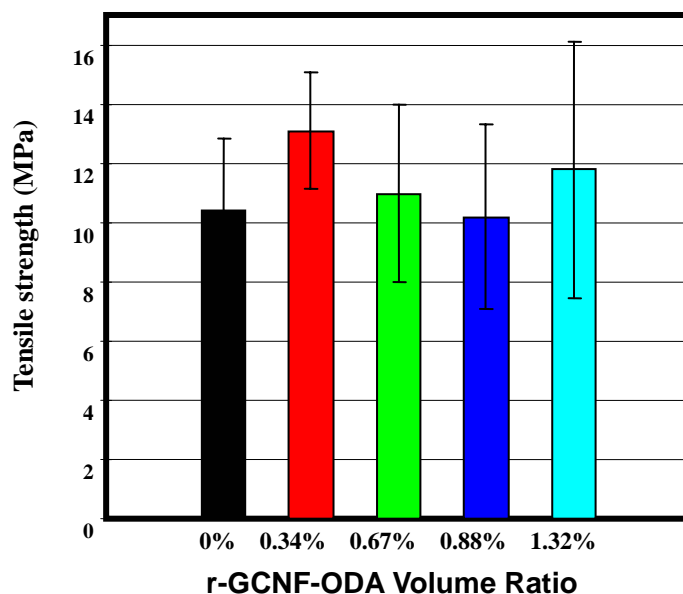


Figure 69. Tensile strength of a series of PMMA-PMMA joints bonded by epoxy/r-GCNF-ODA nanocomposite adhesives with different r-GCNF-ODA loading

A high-temperature curing epoxy resin EPON 828 is used to prepare nanocomposites with r-GCNF-ODA for the fabrication of aluminum joints. Surface treatment in sodium hydroxide solution followed by 3-aminopropyltriethyl silane solution is conducted to chemically bond amine molecules on the surface of aluminum specimens in order to improve bonding between aluminum surface and epoxy adhesives. A series of Al-Al joints are fabricated through epoxy/r-GCNF-ODA nanocomposite adhesives with r-GCNF-ODA loading from 1.54 v% to 5.71 v%. Control Al-Al joints with pure epoxy adhesives are also fabricated under identical conditions.

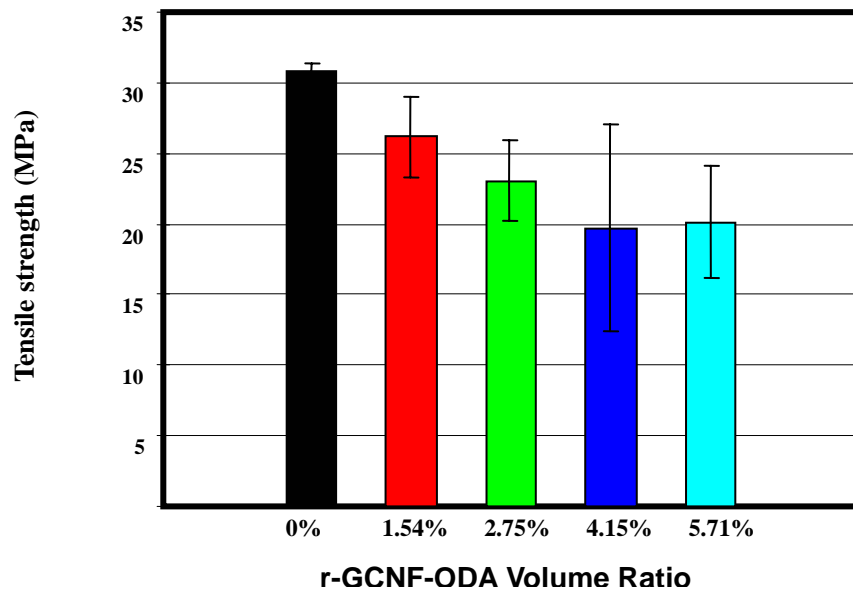


Figure 70. Tensile strength of a series of Al-Al joints bonded by epoxy/r-GCNF-ODA nanocomposite adhesives with different r-GCNF-ODA loading

Tensile strength test results shown in Figure 70 indicate that all the Al-Al joints with nanocomposites have lower tensile strength than the joints featuring pure epoxy. The reduction of tensile strength is determined by the tiny initial debonding areas found on the broken surface of the joints after tensile test. Limited wettability of the nanocomposites on Al surface might contribute to the formation of initial debonding areas although amine molecules are induced on the Al surface to react with epoxy molecules in nanocomposite adhesives. Therefore, selection of an appropriate epoxy

resin with good metal wettability and optimization of the fabrication process are needed to achieve strong bonding between nanocomposite adhesives and Al surface.

5.4. Conclusions

UDD-PGMA brushes and r-GCNF-ODA nanofibers are incorporated in epoxy matrix to prepare epoxy/nanocarbon nanocomposites. Epoxy/UDD-PGMA nanocomposites have better dispersibility than epoxy/as-received UDD due to the surface-grafted PGMA brushes. Up to 302% increase in hardness is obtained at ca. 13.7 wt% UDD loading, which indicates the positive influence of UDD-PGMA as reinforcement additives. Reactivated GCNF-ODA nanofibers are used to prepare epoxy/nanofiber nanocomposite adhesives to bond PMMA and Al specimens, respectively. About ca. 39 % improvement in shear strength and ca. 33 % tensile strength enhancement have been achieved in PMMA-PMMA joints with epoxy/r-GCNF-ODA nanocomposite adhesives. Al-Al joints with epoxy/r-GCNF-ODA nanocomposite adhesives have even lower tensile strength than their counterparts of Al-Al joints with pure epoxy adhesives due to the debonding at the Al-nanocomposite interface.

APPENDIX A

SYNTHESIS OF UDD/EPOXIDE HYBRID MATERIALS VIA RING-OPENING REACTIONS

1. Introduction

In Chapter III, UDD/polymer brushes have been synthesized via *in situ* ATRP of (meth)acrylate monomers demonstrating a successful approach for surface-functionalization of UDD particles. However, the *in situ* ATRP approach requires not only a multi-step process but relatively critical conditions because immobilization of initiator molecules on UDD surface involves acylation and esterification reactions under anhydrous conditions. Given the large number of carboxyl groups on the surface of UDD particles, surface-functionalization could also be achieved by directly reacting surface-bound carboxyl groups with epoxide monomers, since ring-opening of epoxides with carboxylic acids is known to occur with tertiary amines,¹³⁸ chromium (III) ethanoate,¹³⁹ and phase transfer catalysis.¹⁴⁰ Under proper conditions of reaction temperature and catalyst, epoxides undergo ring-opening polymerization resulting in the formation of linear or branch polyethers.¹⁴¹⁻¹⁴⁴ In this work, a series of epoxides featuring various functional groups, such as alkyl, allyl, phenyl, chlorine, methacrylate, and hydroxyl groups, have been found to react with surface-bound carboxyl groups on UDD particles resulting in the preparation of UDD/epoxide hybrid materials. Preliminary characterization data indicate that surface-initiated ring-opening reactions or

polymerization of epoxides occurs in the presence or absence of tertiary amine catalysts resulting in the formation of surface-grafted linker molecules or polymers covalently attached to UDD particles.

2. Experimental Section

Materials

N,N,N',N'',N'''-pentamethyldiethylenetriamine (PMDETA, 99%), 4-methoxyphenol (MEHQ, 98%), butyl glycidyl ether (BGE, 95%), phenyl glycidyl ether (PGE, 99%), allyl glycidyl ether (AGE, 99%), 1,2-epoxybutane (EB, 99%), epichlorohydrin (ECH, 99%), glycidol (96%) and glycidyl methacrylate (GMA, Aldrich, 97%) were purchased from Aldrich and used as received. Solvents were distilled before use and other reagents were used without further purification.

Instruments and Measurements

Infrared spectra (IR) were obtained from KBr pressed pellets with an ATI Mattson Genesis Series FT-IR spectrometer. Thermogravimetric analyses (TGA) were performed on a Thermal Analysis Instruments High-Resolution TGA 2950 Thermogravimetric Analyzer. BET surface area analysis was carried out on a NOVA 1000 High Speed Surface Area & Pore Size Analyzer using nitrogen gas as the adsorbent.

Synthesis of UDD-Epoxy Hybrid Materials

For a typical reaction: A 25 mL round-bottomed flask, with a magnetic stir bar, was

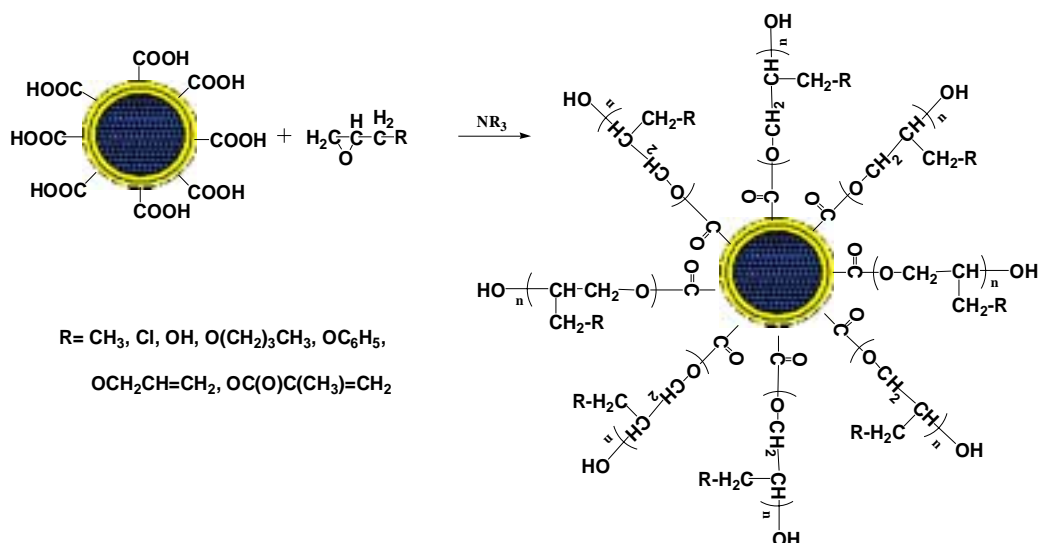
charged with 0.4 g as-received UDD. The flask was sealed with a rubber septum and degassed and refilled with N₂ three times. Then 16 mL PGE was added by syringe and the reaction mixture was sonicated 10 min followed by the addition of 0.56 mL PMDETA via syringe. The flask was placed into a 70 °C oil bath. After 24 h, the reaction mixture was diluted with methanol. The mixture was centrifuged and washed with methanol six times to remove unreacted PGE and free oligomers. The solid product of UDD-PGE-1 was collected and dried in a vacuum oven overnight at room temperature. Other UDD-epoxide hybrid materials were prepared according to the same procedure except reaction temperature varies for different epoxides.

Hydrolysis of UDD-PGE

A 100-mL round-bottomed flask was charged with 0.20 g UDD-PGE-1, 10 mL methanol and 25 mL 2N NaOH solution. The flask was then connected to a condenser and placed into a 75 °C oil bath. After 9 days, the reaction mixture was cooled to room temperature and HCl was added to adjust pH=7. The mixture was filtered through a 0.45 µm Nylon membrane and the residue was redispersed in acetone and centrifuged to wash off hydrolyzed molecules. The UDD residual was collected and dried in vacuum overnight at room temperature. The supernate was combined with the filtrate and rotary evaporated to remove solvents. Then the remaining water solution was extracted with CH₂Cl₂ three times and organic phase was dried over MgSO₄ overnight. MgSO₄ was filtered off and CH₂Cl₂ was removed afterwards by rotary evaporation to collect hydrolyzed product.

3. Results and Discussion

Ring-opening reactions of epoxides can be catalyzed through cationic, anionic, or ionic coordinative mechanisms.¹⁴⁴ Carboxylic acids are common initiators for ring-opening reactions or even ring-opening polymerization of epoxides in the presence of either tertiary amine or Lewis acid catalysts. UDD particles have surface-bound carboxyl groups which can be used as initiating sites to carry out anion-induced ring-opening reactions or polymerization of epoxides using tertiary amines as catalysts (see Scheme 12).



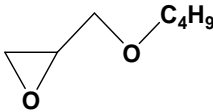
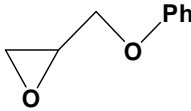
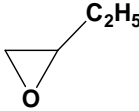
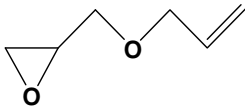
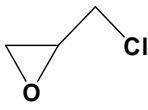
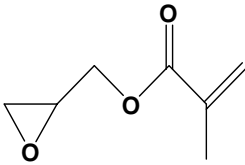
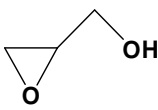
Scheme 12. Synthesis of UDD-epoxide hybrid materials

Table 17 shows the reaction conditions and results when treating as-received UDD particles and epoxides with different functionalities of alkyl, phenyl, allyl, chlorine, methacrylic, and hydroxyl groups. PMDETA is used as tertiary amine catalyst at a

relatively high concentration of ~ 2.5 % except for the UDD-glycidol-1 reaction where a 0.025 % catalyst concentration is used. The low catalyst concentration needed in the UDD-glycidol-1 reaction will be discussed in detail later in this chapter. Reaction temperature also varies as required to account for the different reactivity of oxirane groups and the thermal or chemical stabilities of functional groups present in these epoxides. A free-radical inhibitor, MEHQ, is present during the synthesis of UDD-GMA-1 to prevent radical polymerization of GMA even at the low temperature of 30 °C. The surface-initiated ring-opening reaction of epoxides results in linker molecules grafted on UDD particles and these UDD/epoxide hybrid materials possess organic molecule content ranging from 4.0 wt% to 74.6 wt% according to the TGA results.

FT-IR spectra (see Figure 71) of as-received UDD and UDD/epoxide hybrid materials reveal that different functionalities have been incorporated into the UDD products by surface-grafting of epoxides bearing functional groups. Strong bands observed at 3450 cm^{-1} and 1737 cm^{-1} for UDD are assigned, respectively, to O–H and carboxyl group C=O stretching of the UDD surface carboxyl groups. An intense band at 1730 cm^{-1} for UDD-GMA-1 is assigned to C=O stretching of the ester functional groups in GMA molecules while strong bands at 1730 cm^{-1} for UDD-Glycidol-1 and UDD-ECl-1 are unexpected. FT-IR spectra of UDD-BGE-1 and UDD-Glycidol-1 show strong bands centered at 2930 cm^{-1} and 2850 cm^{-1} originating from C–H stretching in BGE and glycidol molecules, respectively.

Table 17. Conditions and results of ring-opening reaction of a variety of epoxides with as-received UDD.

Sample	Epoxide	UDD/PMDETA/Epoxide	T (°C)	Time (h)	Organic content
UDD-BGE-1		0.4g/0.56mL/16mL	70	24	13.2%
UDD-PGE-1		0.4g/0.56mL/16mL	70	24	11.0%
UDD-EB-1		0.2g/0.28mL/8mL	70	24	4.0%
UDD-AGE-1		0.4g/0.56mL/16mL	30	24	7.6%
UDD-ECI-1		0.4g/0.56mL/16mL	70	24	4.5%
UDD-GMA-1		0.4g/0.56mL/16mL /MEHQ 0.19g	30	24	14.4%
UDD-Glycidol-1		0.4g/5.6μL/16mL	50	24	42.3%

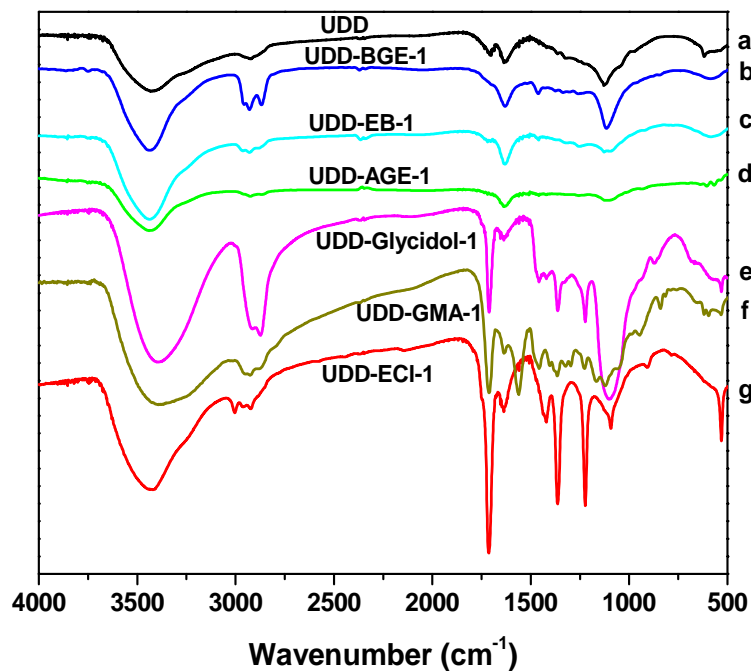


Figure 71. FT-IR spectra of as-received UDD and UDD/epoxide hybrid materials with various functionalities.

BET specific surface area analysis confirms the presence of surface-grafted linker molecules and polymers of epoxides (see Figure 72). When the surface of UDD particles is covered by epoxide linker molecules in UDD-epoxide hybrid materials, the specific surface area decreases from ca. 156.3 m²/g for as-received UDD to as low as ca. 108 m²/g for UDD-GMA-1. The extremely low specific surface area ca. 8.9 m²/g for UDD-Glycidol-1 could be attributed to the surface-grafted polymers of glycidol, rather than to small molecules of glycidol, given that the organic content in UDD-Glycidol-1 is as high as ca. 42.3 wt%.

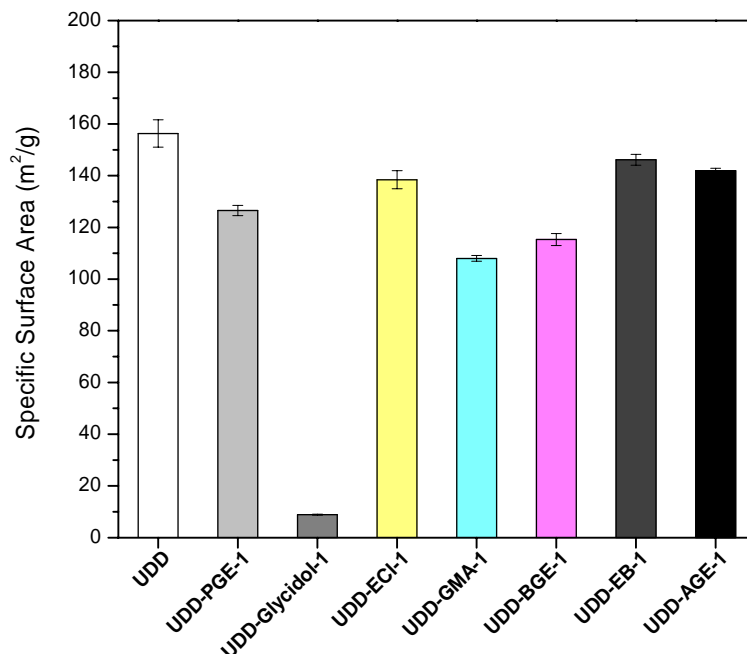


Figure 72. BET results of as-received UDD and UDD/epoxide hybrid materials with various functionalities.

TGA mass-loss curves for as-received UDD and UDD-epoxide hybrid materials are shown in Figure 73. As-received UDD undergoes a gradual ca. 20 wt% mass-loss event from 500 °C to 900 °C attributed to decomposition of surface-bound carboxyl, hydroxyl and other oxyhydrocarbyl groups. In contrast, the UDD-epoxide hybrid materials possess a mass-loss event from 200 °C to 400 °C due to thermal decomposition of the surface-grafted linker molecules of epoxides. However, this event varies in decomposition temperature because of the different epoxide structures.

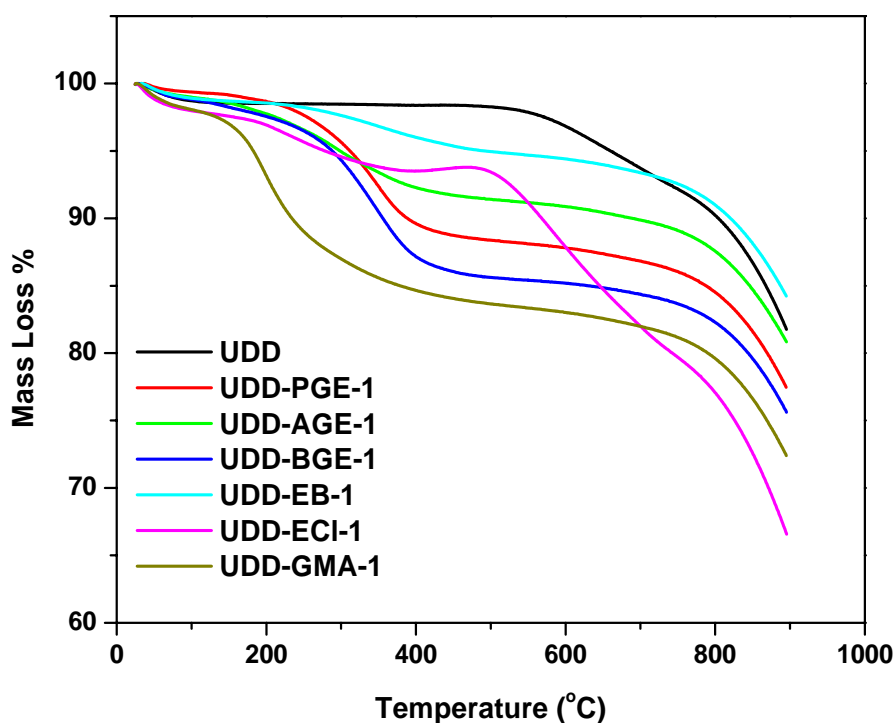


Figure 73. TGA mass-loss curves of as-received UDD and UDD-epoxide hybrid materials with various functionalities.

To verify the presence of surface-grafted epoxide molecules, UDD-PGE-1 was hydrolyzed in NaOH solution to cleave ester linkages attaching PGE chains to UDD surface sites. FT-IR spectra of as-received UDD, UDD-PGE-1 and hydrolyzed UDD-PGE-1 are shown in Figure 74. It is remarkable that after hydrolysis, the IR spectrum of the UDD particles recovers to almost the same as that of the as-received UDD particles, indicating that the features in the IR spectrum of UDD-PGE-1 originate from the grafted PGE linker molecules.

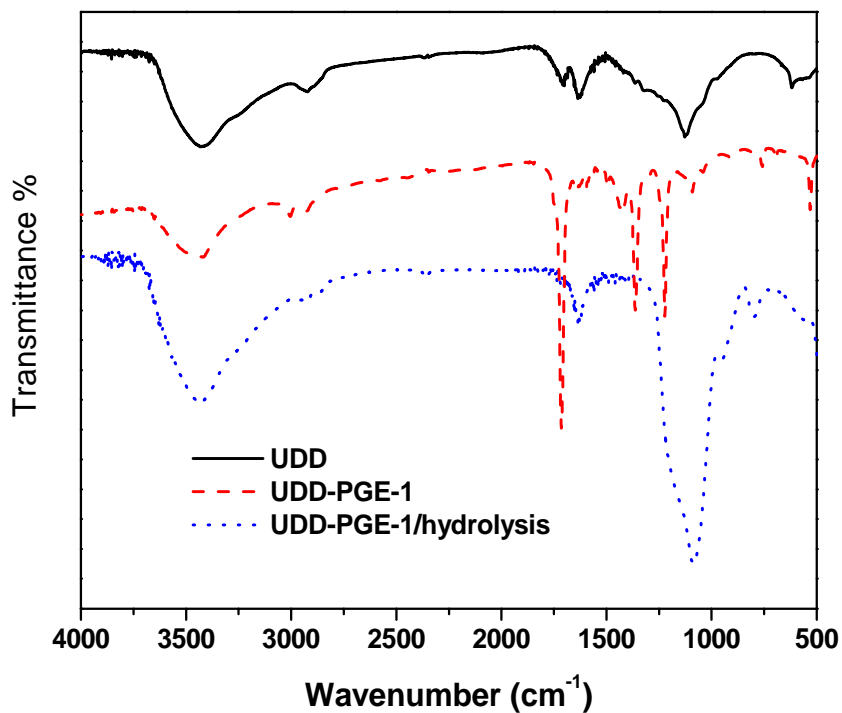


Figure 74. FT-IR spectra of as-received UDD, UDD-PGE-1 and hydrolyzed UDD-PGE-1.

As mentioned above, the reaction of UDD particles and glycidol results in high organic content for the UDD-Glycidol-1 hybrid material, suggesting that the reaction is more of a surface-initiated ring-opening polymerization than a ring-opening reaction of glycidol. The resulting UDD-Glycidol hybrid materials have different structures compared with as-received UDD due to the surface-grafted polymers of glycidol. XRD scans of as-received UDD and UDD-Glycidol-1 (see Figure 75) both contain diffraction

peaks of UDD near 44° in 2θ and 75° in 2θ , as expected. However, an intense peak near 20° in 2θ observed in the UDD-Glycidol-1 diffraction pattern could be amorphous scattering from a carbonaceous phase, indicative of formation of glycidol polymers.

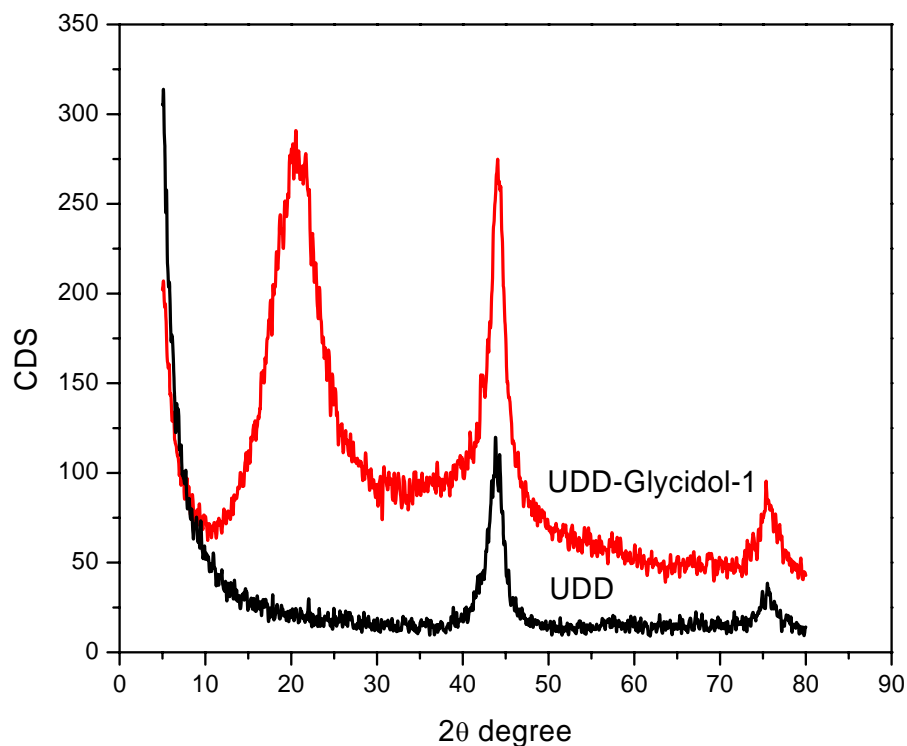
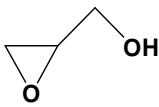
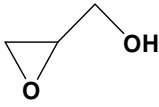
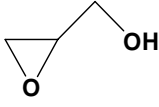
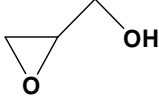
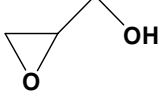
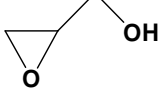
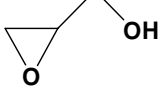
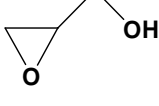


Figure 75. XRD scans of as-received UDD and UDD-Glycidol-1.

It has been reported that cationic ring-opening polymerization of glycidol can be performed at room temperature with $\text{BF}_3 \cdot \text{OEt}_2$ as catalyst at very fast polymerization rates.^{141,143} Surface-initiated ring-opening polymerization of glycidol in this work, however, could be effected by a tertiary amine catalyst. To study the influence of the tertiary amine catalyst PMDETA and temperature on the polymerization of glycidol with

UDD particles, a series of UDD-glycidol hybrid materials were synthesized under different conditions as shown in Table 18.

Table 18. Conditions and results of ring-opening polymerization of glycidol with as-received UDD particles.

Sample	Oxirane	UDD/PMDETA/Glycidol	Temp (°C)	Time (h)	Organic Content
UDD-Glycidol-1		0.4g /0μL/16mL	50	24	41.6%
UDD-Glycidol-2		0.4g /0μL/16mL	70	24	74.6%
UDD-Glycidol-3		0.4g/0μL/16mL	30	24	14%
UDD-Glycidol-4		0.4g/5.6μL/16mL	30	24	9.8%
UDD-Glycidol-5		0.4g/56μL/16mL	30	24	5.0%
UDD-Glycidol-6		0.4g/110μL /16mL	30	24	6.8%
UDD-Glycidol-7		0.4g/56μL/16mL	50	24	24%
UDD-Glycidol-8		0.4g/5.6μL/16mL	50	24	42.0%

It is notable that more surface-grafted polymers are obtained at higher reaction temperature as indicated by organic contents ca. 74.6 wt% in UDD-Glycidol-2 (70 °C), ca. 41.6 wt% in UDD-Glycidol-1 (50 °C), and ca. 14 wt% in UDD-Glycidol-3 (30 °C). However, addition of the PMDETA catalyst to the reaction gives an unexpected lower organic content at the same temperature. For instance, UDD-Glycidol-4 with 0.25 % PMDETA has ca. 9.8 wt% organic content which is less than that of UDD-Glycidol-3 (ca. 14 wt%) without catalyst at the same temperature of 30 °C. Similar results are obtained at higher temperature of 50 °C with 0.25 % PMDETA resulting in ca. 24 wt% organic content for UDD-Glycidol-7, compared with ca. 42.0 wt% for UDD-Glycidol-8 with 0.025 % catalyst concentration. This phenomenon might be attributed to the cationic polymerization mechanism for glycidol polymerization being operative in the presence of UDD particles. Although tertiary amines are effective catalysts for the addition of carboxyl to oxirane groups in epoxides,^{138,139} the propagation reaction may not favor the anionic mechanism, resulting a lower polymerization rate in the presence of tertiary amines.

Figure 76 shows the TGA mass-loss curves of aliquot samples of UDD-Glycidol-1 taken at different time during the reaction course. The mass-loss event from 250 °C to 400 °C is assigned to the decomposition of glycidol polymers grafted on the surface of UDD particles.

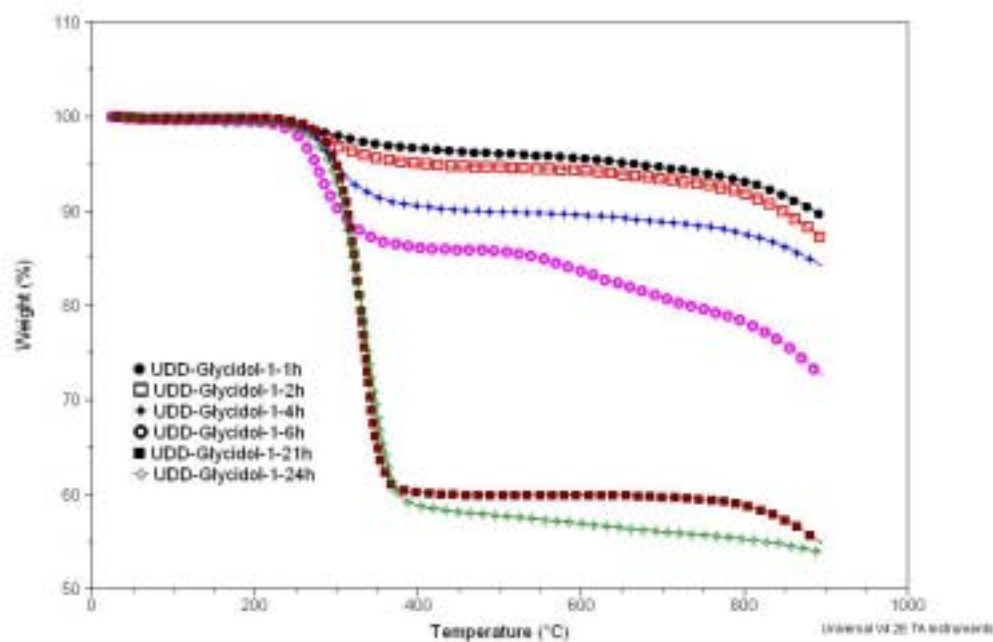


Figure 76. TGA mass-loss curves of UDD-Glycidol-1 at different reaction time.

The kinetic difference between the two reactions forming UDD-Glycidyl-1 and UDD-Glycidyl-2 can be obtained in Figure 77. The plot of organic content over reaction time for UDD-Glycidyl-1 has a nearly linear shape, indicating a possible linear growth of polymer chains during the reaction. On the other hand, the plot for UDD-Glycidyl-2 levels off after 6 hours, even though the reaction rate is higher than that of UDD-Glycidyl-1 because the reaction of UDD-Glycidol-2 is carried out at a higher temperature (70°C). This result indicates that the surface-initiated polymerization of glycidol in the presence of UDD is more controllable at relatively low temperature,

which is consistent with the fast polymerization rate of glycidol even at room temperature.¹⁴³

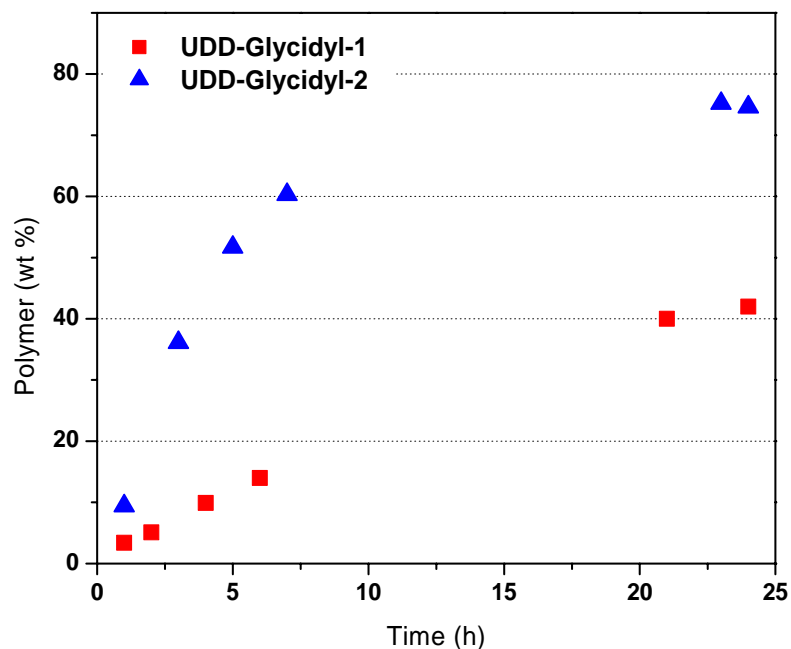


Figure 77. Grafted polymer amount as a function of reaction time for UDD-Glycidol-1 and UDD-Glycidol-2.

4. Conclusions

Surface functionalization of UDD particles can be achieved by a simple ring-opening reaction or polymerization of epoxides initiated by surface-bound carboxyl groups on UDD particles. UDD/epoxide hybrid materials featuring alkyl, phenyl, allyl, chlorine, methacrylic, or hydroxyl groups have been synthesized with organic content ranging from ca. 4.0 wt% to 14.4 wt% via ring-opening reaction of epoxides bearing various functional groups. Ring-opening polymerization of glycidol can be conducted to prepare

UDD- Glycidol hybrid materials with surface-grafted polymer content as high as ca. 74.6 wt%. PMDETA is active for ring-opening reaction of epoxides as a tertiary amine catalyst while it acts as inhibitor in ring-opening polymerization of glycidol. The surface-grafted polymer content in UDD-Glycidol hybrid materials can be controlled simply by changing reaction temperature for glycidol ring-opening polymerization. This approach could be a versatile surface-functionalization method for UDD particles, since only one reaction with mild conditions is required to graft linker molecules or polymer chains on the surfaces of UDD particles.

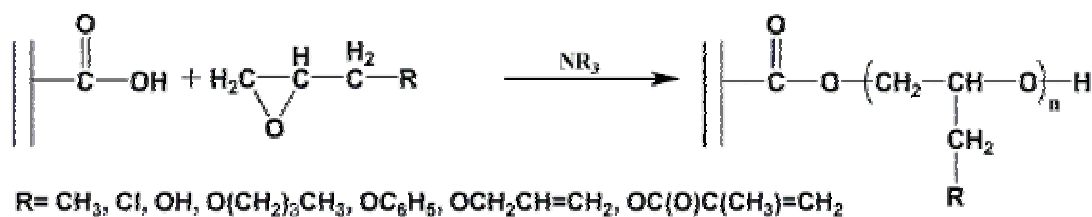
APPENDIX B

SYNTHESIS OF GCNF/EPOXIDE HYBRID MATERIALS VIA RING-OPENING REACTIONS

1. Introduction

Surface-functionalization of GCNF nanofibers through surface-bound carboxyl groups has been extensively investigated. Most approaches involve multi-step reactions to achieve desired functionalities mainly through active intermediate acyl chlorides converted from carboxyls on the surface of GCNF nanofibers. Acylation reaction requires critical anhydrous conditions and complicated purification procedures. Therefore, alternative reactions with mild conditions and simple purification procedures are preferable. Carboxyl groups can react directly with epoxide molecules through ring-opening reactions in the presence of a proper catalyst.¹⁴¹⁻¹⁴⁴ As discussed in Appendix A, surface-functionalization of UDD particles has been conducted by surface-bound carboxylic acid-initiated ring-opening reactions of epoxides bearing various functional groups. This simple reaction can also be applied to GCNF nanofibers for a one-step reaction surface functionalization process, which has obvious advantages over current approaches requiring an intermediate acyl chloride intermediate. The reaction conditions for ring-opening of epoxides are ambient, and various functional groups such as alkyl, phenyl, allyl, chlorine, methacrylic, and hydroxyl groups can be bound to the surface of GCNF nanofibers by using epoxide molecules featuring these

functionalities. Synthesis of GCNF-epoxide hybrid materials through the surface-bound carboxylic acid-initiated ring-opening reaction of a series of epoxides is reported (see Scheme 13) and selected characterizations data are discussed in this chapter.



Scheme 13. Synthesis of GCNF-epoxide hybrid materials via ring-opening reaction.

2. Experimental Section

Materials

N,N,N',N'',N'''-pentamethyldiethylenetriamine (PMDETA, 99%), benzyldimethylamine (BDMA, 97%), butyl glycidyl ether (BGE, 95%), phenyl glycidyl ether (PGE, 99%), allyl glycidyl ether (AGE, 99%), 1,2-epoxybutane (EB, 99%), epichlorohydrin (ECl, 99%), glycidol (96%) and glycidyl methacrylate (GMA, Aldrich, 97%) were purchased from Aldrich and used as received. Solvents were distilled before use and other reagents were used without further purification.

Instruments and Measurements

Infrared spectra (IR) were obtained from KBr pressed pellets with an ATI Mattson Genesis Series FT-IR spectrometer. Thermogravimetric analyses (TGA) were performed on a Thermal Analysis Instruments High-Resolution TGA 2950 Thermogravimetric

Analyzer. BET surface area analysis was carried out on a NOVA 1000 High Speed Surface Area & Pore Size Analyzer using nitrogen gas as the absorbent.

Synthesis of GCNF/Epoxy Hybrid Materials

For a typical reaction: a 25-mL dried round-bottomed flask was charged with 0.20 g GCNF-CO₂H and 5 mL PGE was added. The reaction mixture was sonicated for 5 min to form a uniform dispersion. After addition of 55 μ L BDMA, the reaction mixture was allowed to stir at room temperature for 5 min before placing the flask into a 120 °C oil bath. After 24 h, the reaction was quenched by adding acetone to dilute the mixture followed by centrifuge to separate the nanofibers. The sonication-centrifuge process was repeated six times to ensure no unreacted PGE left in the residue. The collected product was dried in vacuum at room temperature overnight. A variety of epoxides were reacted with GCNF-CO₂H under similar conditions to prepare GCNF-epoxy hybrid materials.

3. Results and Discussion

Oxidized GCNFs, when treated with epoxy monomers containing alkyl, phenyl, allyl, chlorine, methacrylic, and hydroxyl functional groups, form the corresponding GCNF/epoxy oligomeric materials. Selected reaction conditions and GCNF/epoxy product identities and organic content are provided in Table 19. Two tertiary amine catalysts, PMDETA and BDMA, were used at a concentration of 0.25% but no obvious catalytic reactivity difference was observed in the reactions of GCNF-BGE-1 and

GCNF-BGE-2 under identical conditions. Therefore, PMDETA was used as catalyst in most of the reactions for other epoxides. Reaction temperatures were chosen based on the reactivity and thermal stability of each epoxide monomer. Specifically, low temperature is necessary for the reaction of glycidol and GMA, because the former is a very reactive epoxide monomer which can undergo ring-opening polymerization at fast rates under ambient conditions, and the latter will conduct free-radical polymerization through the methacrylic double bond. Both GCNF-Glycidol-1 and GCNF-GMA-1 reactions are performed at 30 °C with the same 0.25 % concentration of PMDETA catalyst. However, even at this low temperature, glycidol in GCNF-Glycidol-1 reaction still undergoes fast polymerization and more than 90 % of glycidol monomer was converted to polymer in 2 hours, whereas only 10 wt% of organic content was obtained in the resulting GCNF-Glycidol-1 hybrid material.

On the other hand, the reaction of GCNF-GMA-1 might involve free-radical polymerization of methacrylic groups in GMA in addition to the ring-opening of oxirane groups in GMA, because when free-radical inhibitor MEHQ is added at 30 °C, the reaction of GCNF-GMA-2 gives ca. 8.1 wt% of organic content compared to ca. 13.7 wt% for UDD-GMA-1. Surface-initiated ring-opening reaction of other epoxides results in linker molecules grafted on GCNF nanofibers and these GCNF/epoxide hybrid materials possess organic molecule content ranging from 8.40 wt% to 11 wt% due to variable reactivity of these epoxide monomers having different functionalities.

Table 19. Conditions and results of ring-opening reaction of various epoxides with oxidized GCNF nanofibers

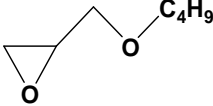
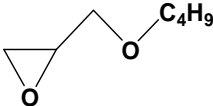
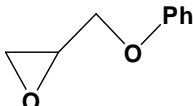
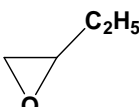
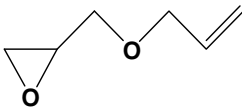
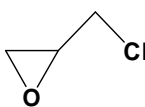
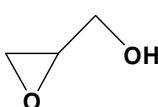
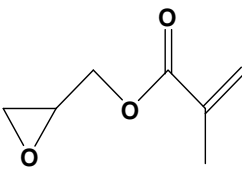
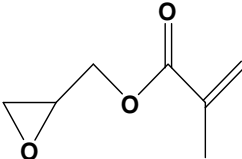
Sample	Oxirane	Catalyst	Temp (°C)	Time (h)	Organic Content
GCNF-BGE-1		PMDETA	70	24	8.3%
GCNF-BGE-2		BDMA	70	24	8.8%
GCNF-PGE-1		BDMA	120	24	11%
GCNF-EB-1		PMDETA	70	24	10%
GCNF-AGE-1		PMDETA	70	24	10.5%
GCNF-ECI-1		PMDETA	70	24	8.4%
GCNF-Glycidol-1		PMDETA	30	2	10%
GCNF-GMA-1		PMDETA	30	24	13.7%
GCNF-GMA-2		PMDETA/ MEHQ	30	24	8.1%

Figure 78 shows FT-IR spectra of oxidized GCNF and selected GCNF-epoxide hybrid materials. In the oxidized GCNF spectrum, the broad bands centered at 1222 cm^{-1} and 1576 cm^{-1} are attributed to the vibration of C-C stretching and aromatic rings in graphitic sheets, respectively. The other two feature bands at 3430 cm^{-1} and 1732 cm^{-1} are assigned to O-H and C=O stretching of the surface-bound carboxyl groups on GCNF nanofibers.

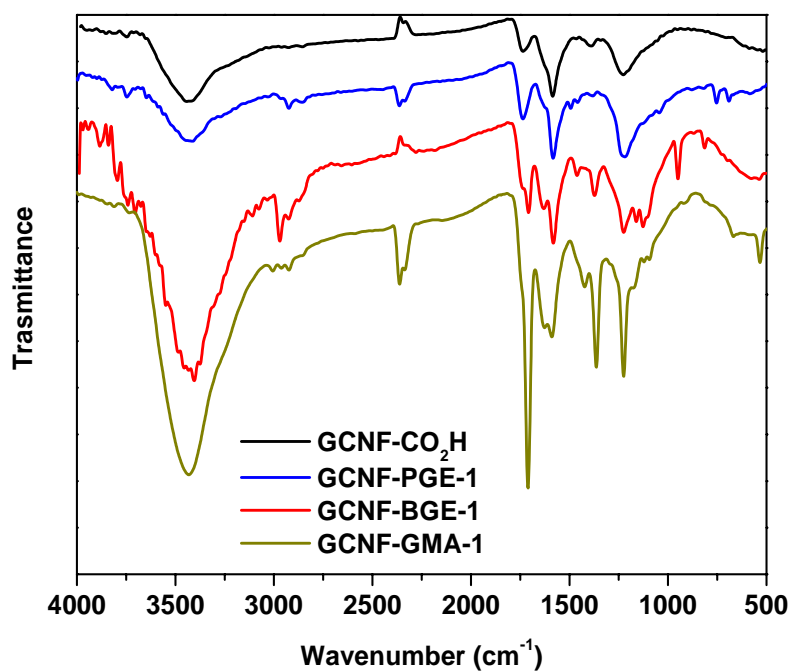


Figure 78. FT-IR spectra of GCNF-CO₂H and GCNF/epoxide hybrid materials.

The GCNF-PGE-1 spectrum shows similar FT-IR features as that of oxidized GCNF except the enhanced C-H stretching bands at 2944 cm^{-1} and 2829 cm^{-1} , which are

attributed to the surface-grafted linker molecules of PGE. The GCNF-BGE-1 spectrum also displays strong bands at 2969 cm^{-1} and 2858 cm^{-1} of C-H stretching vibration originated from the BGE linker molecules. The strong band at 1712 cm^{-1} for GCNF-GMA-1 spectrum is enhanced by C=O stretching of the ester groups in GMA molecules grafted on the surface of GCNF nanofibers.

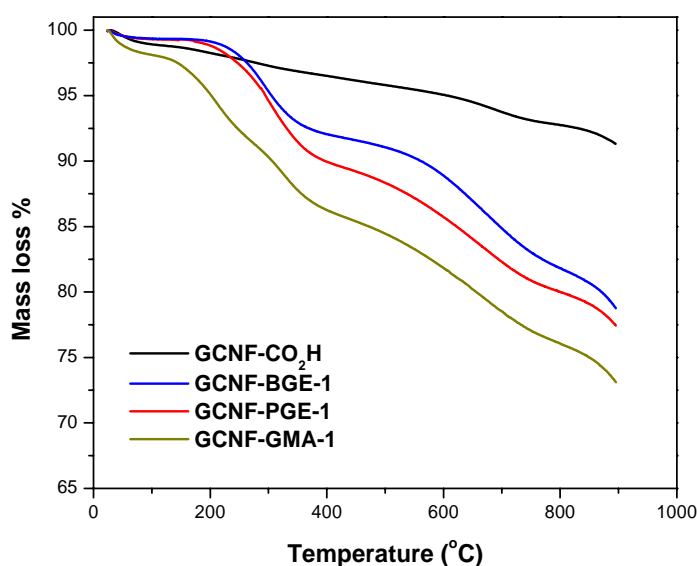


Figure 79. TGA curves of GCNF-CO₂H and GCNF-epoxide hybrid materials

TGA mass-loss curves for oxidized GCNF and selected GCNF/epoxide hybrid materials are shown in Figure 79. Oxidized GCNF has a gradual ca. 8 wt% mass-loss event from 100 °C to 900 °C which is attributed to decomposition of surface-bound carboxyl, hydroxyl, and other oxyhydrocarbyl groups. All of the GCNF/epoxide hybrid materials, however, have a mass-loss event from 200 °C to 400 °C due to the

decomposition of surface-grafted linker molecules of epoxides. Variable mass-loss from ca. 8.4 wt% to 13.7 wt% in this temperature range indicates different organic content in each of these GCNF-epoxide hybrid materials as a result of the ring-opening reaction of corresponding epoxides.

BET specific surface area analysis (see Figure 80) confirms that linker molecules of epoxides are indeed grafted on the surface of GCNF nanofibers. Oxidized GCNF has a specific surface area ca. 28.1 m²/g while GCNF-epoxide hybrid materials have much smaller specific surface area ranging from ca. 8.9 m²/g for GCNF-AGE-1 to ca. 15.5 m²/g for GCNF-BGE-1, respectively. The drastic decrease of specific surface area after the reaction of oxidized GCNF nanofibers with epoxides is attributed to the rough surface of nanofibers partially covered by surface-grafted linker molecules of epoxides.

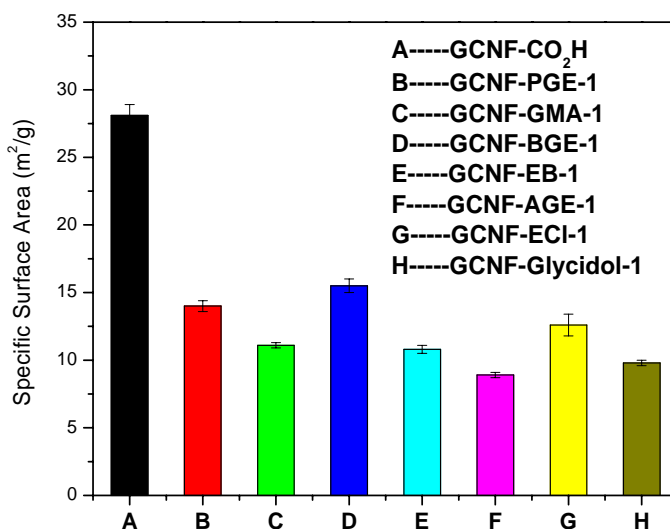


Figure 80. BET analysis of GCNF-CO₂H and GCNF-epoxide hybrid materials.



Figure 81. Dispersibility test of GCNF-CO₂H in A) Toluene, B) Chloroform, C) Isopropyl alcohol, D) Methanol, E) THF, F) Ethyl acetate, G) Water, H) Acetone, I) DMF at the concentration of about 0.1 mg/mL



Figure 82. Dispersibility test of GCNF-PGE-1 in A) Toluene, B) Chloroform, C) Isopropyl alcohol, D) Methanol, E) THF, F) Ethyl acetate, G) Water, H) Acetone, I) DMF at the concentration of about 0.1 mg/mL .

As discussed in chapter II, surface-grafted polymer brushes have great effect on the dispersibility of GCNF-polymer brush materials. GCNF-epoxide hybrid materials prepared in this chapter via surface-initiated ring-opening reaction of epoxides also change the dispersibility of GCNF nanofibers in common solvents due to the corresponding surface-grafted linker molecules of epoxide. For example, GCNF-PGE-1 has a different dispersibility “fingerprint” from oxidized GCNF in a series of solvents as shown in Figure 81 and Figure 82, respectively.

A total of nine solvents with increasing polarity are used to disperse GCNF-CO₂H nanofibers at the concentration of 0.1 mg/mL. In Figure 81, nanofibers precipitate out completely from the solvents of toluene and chloroform, while stable dispersions are obtained for those solvents with relatively higher polarity. In contrast, GCNF-PGE-1 hybrid material stays in chloroform resulting in a stable dispersion although precipitation does occur in toluene as illustrated in Figure 82. It is obvious that surface-grafted PGE linker molecules influence the dispersibility of GCNF nanofibers in common solvents especially in less polar solvents due to the molecular structure of PGE bearing a phenyl group. Therefore, the dispersibility of GCNF-epoxy oligomer materials is dominated by the functional groups present within the epoxide monomer. By incorporating proper functional groups into the GCNF-epoxide hybrid materials, desired dispersibility properties can be achieved.

4 . Conclusions

Another approach for surface functionalization of GCNF nanofibers has been demonstrated. Surface-grafted epoxy linker molecules can be formed in a single step by a simple ring-opening reaction of epoxide monomers initiated by surface-bound carboxylic acid groups present in oxidized GCNFs in the presence of tertiary amine catalysts. GCNF-epoxide hybrid materials featuring various functional groups have been synthesized with organic content ranging from ca. 8.1 wt% to 13.7 wt% via ring-opening reaction of epoxides bearing alkyl, phenyl, allyl, chlorine, methacrylic, or hydroxyl

groups. The dispersibility of GCNF nanofibers in common solvents can be altered by desired surface-grafted linker molecules, which is important for expanding the applications of GCNF nanofibers.

BIBLIOGRAPHY

1. Kroto, H. W.; Heath, J. R.; O'Brien, S. C.; Curl, R. F.; Smalley, R. E. *Nature* **1985**, *318*, 162-163.
2. Iijima, S. *Nature* **1991**, *354*, 56-58.
3. Shenderova, O. A.; Zhirnov, V. V.; Brenner, D. W. *Critical Reviews in Solid State and Materials Sciences* **2002**, *27*, 227-356.
4. Iijima, S.; Ichihashi, T. *Nature* **1993**, *363*, 603-605.
5. Bethune, D. S.; Kiang, C. H.; Devries, M. S.; Gorman, G.; Savoy, R.; Vazquez, J.; Beyers, R. *Nature* **1993**, *363*, 605-607.
6. Balasubramanian, K.; Burghard, M. *Small* **2005**, *1*, 180-192.
7. Dresselhaus, M. S.; Dresselhaus, G.; Avouris, P. *Carbon nanotubes: synthesis, properties and applications*; Springer: Berlin, **2001**.
8. Ajayan, P. M. *Chemical Reviews* **1999**, *99*, 1787-1799.
9. Ajayan, P. M.; Zhou, O. Z. *Carbon Nanotubes* **2001**, *80*, 391-425.
10. Baughman, R. H.; Zakhidov, A. A.; de Heer, W. A. *Science* **2002**, *297*, 787-792.
11. Robertson, N.; McGowan, C. A. *Chemical Society Reviews* **2003**, *32*, 96-103.
12. De Jong, K. P.; Geus, J. W. *Catalysis Reviews-Science and Engineerin* **2000**, *42*, 481-510.
13. Rodriguez, N. M. *Journal of Materials Research* **1993**, *8*, 3233-3250.
14. Rodriguez, N. M.; Chambers, A.; Baker, R. T. K. *Langmuir* **1995**, *11*, 3862-3866.
15. Vander Wal, R. L.; Ticich, T. M.; Curtis, V. E. *Journal of Physical Chemistry B* **2000**, *104*, 11606-11611.
16. Helveg, S.; Lopez-Cartes, C.; Sehested, J.; Hansen, P. L.; Clausen, B. S.; Rostrup-Nielsen, J. R.; Abild-Pedersen, F.; Norskov, J. K. *Nature* **2004**, *427*,

426-429.

17. Baker, R. T. K.; Kim, M. S.; Chambers, A.; Park, C.; Rodriguez, N. M. *Catalyst Deactivation* **1997**, *111*, 99-109.
18. Melechko, A. V.; Merkulov, V. I.; McKnight, T. E.; Guillorn, M. A.; Klein, K. L.; Lowndes, D. H.; Simpson, M. L. *Journal of Applied Physics* **2005**, *97*, 041301/041301-041301/041339.
19. Teo, K. B. K.; Chhowalla, M.; Amaratunga, G. A. J.; Milne, W. I.; Pirio, G.; Legagneux, P.; Wyczisk, F.; Pribat, D.; Hasko, D. G. *Applied Physics Letters* **2002**, *80*, 2011-2013.
20. Adhyapak, P. V.; Maddanimath, T.; Pethkar, S.; Chandwadkar, A. J.; Negi, Y. S.; Vijayamohanan, K. *Journal of Power Sources* **2002**, *109*, 105-110.
21. Chambers, A.; Park, C.; Baker, R. T. K.; Rodriguez, N. M. *Journal of Physical Chemistry B* **1998**, *102*, 4253-4256.
22. Tibbetts, G. G.; Meisner, G. P.; Olk, C. H. *Carbon* **2001**, *39*, 2291-2301.
23. Ahn, C. C.; Ye, Y.; Ratnakumar, B. V.; Witham, C.; Bowman, R. C.; Fultz, B. *Applied Physics Letters* **1998**, *73*, 3378-3380.
24. Banerjee, S.; Murad, S.; Puri, I. K. *Proceedings of the IEEE* **2006**, *94*, 1806-1814.
25. Serp, P.; Corrias, M.; Kalck, P. *Applied Catalysis a-General* **2003**, *253*, 337-358.
26. Chambers, A.; Nemes, T.; Rodriguez, N. M.; Baker, R. T. K. *Journal of Physical Chemistry B* **1998**, *102*, 2251-2258.
27. Salman, F.; Park, C.; Baker, R. T. K. *Catalysis Today* **1999**, *53*, 385-394.
28. Gao, R.; Tan, C. D.; Baker, R. T. K. *Catalysis Today* **2001**, *65*, 19-29.
29. Carneiro, O. C.; Anderson, P. E.; Rodriguez, N. M.; Baker, R. T. K. *Journal of Physical Chemistry B* **2004**, *108*, 13307-13314.
30. Steigerwalt, E. S.; Deluga, G. A.; Cliffl, D. E.; Lukehart, C. M. *Journal of Physical Chemistry B* **2001**, *105*, 8097-8101.

31. Steigerwalt, E. S.; Deluga, G. A.; Lukehart, C. M. *Journal of Physical Chemistry B* **2002**, *106*, 760-766.
32. Steigerwalt, E. S.; Deluga, G. A.; Lukehart, C. M. *Journal of Nanoscience and Nanotechnology* **2003**, *3*, 247-251.
33. Ros, T. G.; van Dillen, A. J.; Geus, J. W.; Koningsberger, D. C. *Chemistry-a European Journal* **2002**, *8*, 2868-2878.
34. Lu, W. J.; Steigerwalt, E. S.; Moore, J. T.; Sullivan, L. M.; Collins, W. E.; Lukehart, C. M. *Journal of Nanoscience and Nanotechnology* **2004**, *4*, 803-808.
35. Li, J.; Lukehart, C. M. *Composite Interfaces* **2004**, *11*, 525-535.
36. Hirota, K.; Takaura, Y.; Kato, M.; Miyamoto, Y. *Journal of Materials Science* **2007**, *42*, 4792-4800.
37. Finegan, I. C.; Tibbetts, G. G.; Glasgow, D. G.; Ting, J. M.; Lake, M. L. *Journal of Materials Science* **2003**, *38*, 3485-3490.
38. Tibbetts, G. G.; McHugh, J. J. *Journal of Materials Research* **1999**, *14*, 2871-2880.
39. Zeng, J. J.; Saltysiak, B.; Johnson, W. S.; Schiraldi, D. A.; Kumar, S. *Composites Part B-Engineering* **2004**, *35*, 245-249.
40. Lafdi, K.; Matzek, M. In *48th International SAMPE symposium proceedings*: Long Beach, USA, **2003**.
41. Lozano, K.; Barrera, E. V. *Journal of Applied Polymer Science* **2001**, *79*, 125-133.
42. Hu, Y. H.; Shenderova, O. A.; Brenner, D. W. *Journal of Computational and Theoretical Nanoscience* **2007**, *4*, 199-221.
43. Aleksenskii, A. E.; Baidakova, M. V.; Vul', A. Y.; Siklitskii, V. I. *Physics of the Solid State* **1999**, *41*, 668-671.
44. Osipov, V.; Baidakova, M.; Takai, K.; Enoki, T.; Vul, A. *Fullerenes Nanotubes and Carbon Nanostructures* **2006**, *14*, 565-572.
45. Nesterenko, P. N.; Fedyanina, O. N.; Volgin, Y. V. *Analyst* **2007**, *132*, 403-405.

46. Nesterenko, P. N.; Fedyanina, O. N.; Volgin, Y. V.; Jones, P. *Journal of Chromatography A* **2007**, *1155*, 2-7.
47. Yu, S. J.; Kang, M. W.; Chang, H. C.; Chen, K. M.; Yu, Y. C. *Journal of the American Chemical Society* **2005**, *127*, 17604-17605.
48. Fu, C. C.; Lee, H. Y.; Chen, K.; Lim, T. S.; Wu, H. Y.; Lin, P. K.; Wei, P. K.; Tsao, P. H.; Chang, H. C.; Fann, W. *Proceedings of the National Academy of Sciences of the United States of America* **2007**, *104*, 727-732.
49. Pramatarova, L.; Pecheva, E.; Stavrev, S.; Spasov, T.; Montgomery, P.; Toth, A.; Dimitrova, M.; Apostolova, M. *Journal of Optoelectronics and Advanced Materials* **2007**, *9*, 236-239.
50. Kruger, A.; Liang, Y. J.; Jarre, G.; Stegk, J. *Journal of Materials Chemistry* **2006**, *16*, 2322-2328.
51. Livramento, V.; Correia, J. B.; Shohoji, N.; Osawa, E. *Diamond and Related Materials* **2007**, *16*, 202-204.
52. Ekimov, E. A.; Gromnitskaya, E. L.; Gierlotka, S.; Lojkowski, W.; Palosz, B.; Swiderska-Sroda, A.; Kozubowski, J. A.; Naletov, A. M. *Journal of Materials Science Letters* **2002**, *21*, 1699-1702.
53. Tasis, D.; Tagmatarchis, N.; Bianco, A.; Prato, M. *Chemical Reviews* **2006**, *106*, 1105-1136.
54. Liu, J.; Rinzler, A. G.; Dai, H. J.; Hafner, J. H.; Bradley, R. K.; Boul, P. J.; Lu, A.; Iverson, T.; Shelimov, K.; Huffman, C. B.; Rodriguez-Macias, F.; Shon, Y. S.; Lee, T. R.; Colbert, D. T.; Smalley, R. E. *Science* **1998**, *280*, 1253-1256.
55. Chen, J.; Hamon, M. A.; Hu, H.; Chen, Y. S.; Rao, A. M.; Eklund, P. C.; Haddon, R. C. *Science* **1998**, *282*, 95-98.
56. Ros, T. G.; van Dillen, A. J.; Geus, J. W.; Koningsberger, D. C. *Chemistry-a European Journal* **2002**, *8*, 1151-1162.
57. Rasheed, A.; Howe, J. Y.; Dadmun, M. D.; Britt, P. F. *Carbon* **2007**, *45*, 1072-1080.
58. Zhou, J. H.; Sui, Z. J.; Zhu, J.; Li, P.; De, C.; Dai, Y. C.; Yuan, W. K. *Carbon* **2007**, *45*, 785-796.

59. Shi, D. L.; Lian, J.; He, P.; Wang, L. M.; Xiao, F.; Yang, L.; Schulz, M. J.; Mast, D. B. *Applied Physics Letters* **2003**, *83*, 5301-5303.
60. Li, J.; Vergne, M. J.; Mowles, E. D.; Zhong, W. H.; Hercules, D. M.; Lukehart, C. M. *Carbon* **2005**, *43*, 2883-2893.
61. Cataldo, F.; Koscheev, A. P. *Fullerenes Nanotubes and Carbon Nanostructures* **2003**, *11*, 201-218.
62. Shenderova, O.; Petrov, I.; Walsh, J.; Grichko, V.; Grishko, V.; Tyler, T.; Cunningham, G. *Diamond and Related Materials* **2006**, *15*, 1799-1803.
63. Osswald, S.; Yushin, G.; Mochalin, V.; Kucheyev, S. O.; Gogotsi, Y. *Journal of the American Chemical Society* **2006**, *128*, 11635-11642.
64. Dement'ev, A. P.; Maslakov, K. I. *Physics of the Solid State* **2004**, *46*, 678-680.
65. Kulakova, I. I. *Physics of the Solid State* **2004**, *46*, 636-643.
66. Wang, J. S.; Matyjaszewski, K. *Journal of the American Chemical Society* **1995**, *117*, 5614-5615.
67. Kato, M.; Kamigaito, M.; Sawamoto, M.; Higashimura, T. *Macromolecules* **1995**, *28*, 1721-1723.
68. Nishikawa, T.; Ando, T.; Kamigaito, M.; Sawamoto, M. *Macromolecules* **1997**, *30*, 2244-2248.
69. Fischer, H. *Chemical Reviews* **2001**, *101*, 3581-3610.
70. Tang, W.; Tsarevsky, N. V.; Matyjaszewski, K. *Journal of the American Chemical Society* **2006**, *128*, 1598-1604.
71. Braunecker, W. A.; Matyjaszewski, K. *Progress in Polymer Science* **2007**, *32*, 93-146.
72. Pyun, J.; Kowalewski, T.; Matyjaszewski, K. *Macromolecular Rapid Communications* **2003**, *24*, 1043-1059.
73. Kong, X. X.; Kawai, T.; Abe, J.; Iyoda, T. *Macromolecules* **2001**, *34*, 1837-1844.

74. Matrabi, T.; Save, M.; Charleux, B.; Pinson, J.; Cabet-Deliry, E.; Adenier, A.; Chehimi, M. M.; Delamar, M. *Surface Science* **2007**, *601*, 2357-2366.
75. Rupert, B. L.; Mulvihill, M. J.; Arnold, J. *Chemistry of Materials* **2006**, *18*, 5045-5051.
76. Fan, X. W.; Lin, L. J.; Messersmith, P. B. *Composites Science and Technology* **2006**, *66*, 1198-1204.
77. Min, K.; Hu, J. H.; Wang, C. C.; Elaissari, A. *Journal of Polymer Science Part a-Polymer Chemistry* **2002**, *40*, 892-900.
78. Carrot, G.; Diamanti, S.; Manuszak, M.; Charleux, B.; Vairon, I. P. *Journal of Polymer Science Part a-Polymer Chemistry* **2001**, *39*, 4294-4301.
79. Jayachandran, K. N.; Takacs-Cox, A.; Brooks, D. E. *Macromolecules* **2002**, *35*, 4247-4257.
80. Qin, S. H.; Oin, D. Q.; Ford, W. T.; Resasco, D. E.; Herrera, J. E. *Journal of the American Chemical Society* **2004**, *126*, 170-176.
81. Yao, Z. L.; Braidy, N.; Botton, G. A.; Alex, A. T. *Journal of the American Chemical Society* **2003**, *125*, 16015-16024.
82. Kong, H.; Gao, C.; Yan, D. Y. *Journal of the American Chemical Society* **2004**, *126*, 412-413.
83. Baskaran, D.; Mays, J. W.; Bratcher, M. S. *Angewandte Chemie-International Edition* **2004**, *43*, 2138-2142.
84. Kong, H.; Gao, C.; Yan, D. Y. *Journal of Materials Chemistry* **2004**, *14*, 1401-1405.
85. Zhong, W. H.; Li, J.; Xu, L. Y. R.; Michel, J. A.; Sullivan, L. M.; Lukehart, C. M. *Journal of Nanoscience and Nanotechnology* **2004**, *4*, 794-802.
86. Zhong, W. H.; Li, J.; Lukehart, C. M.; Xu, L. Y. R. *Polymer Composites* **2005**, *26*, 128-135.
87. Xu, L. R.; Bhamidipati, V.; Zhong, W. H.; Li, J.; Lukehart, C. M.; Lara-Curzio, E.; Liu, K. C.; Lance, M. J. *Journal of Composite Materials* **2004**, *38*, 1563-1582.

88. Homenick, C. M.; Lawson, G.; Adronov, A. *Polymer Reviews* **2007**, *47*, 265-290.
89. Liu, T. Q.; Jia, S.; Kowalewski, T.; Matyjaszewski, K.; Casado-Portilla, R.; Belmont, J. *Langmuir* **2003**, *19*, 6342-6345.
90. Blum, F. D. *Annual Reports on NMR Spectroscopy* **1994**, *28*, 277-321.
91. Davis, K. A.; Matyjaszewski, K. *Chinese Journal of Polymer Science* **2004**, *22*, 195-204.
92. Matyjaszewski, K.; Shipp, D. A.; Wang, J. L.; Grimaud, T.; Patten, T. E. *Macromolecules* **1998**, *31*, 6836-6840.
93. Davis, K. A.; Matyjaszewski, K. *Macromolecules* **2000**, *33*, 4039-4047.
94. Ghosh, S.; Krishnamurti, N. *European Polymer Journal* **2000**, *36*, 2125-2131.
95. Canamero, P. F.; de la Fuente, J. L.; Madruga, E. L.; Fernandez-Garcia, M. *Macromolecular Chemistry and Physics* **2004**, *205*, 2221-2228.
96. Li, G.; Zhu, X. L.; Zhu, J.; Cheng, Z. P.; Zhang, W. *Polymer* **2005**, *46*, 12716-12721.
97. Xu, F. J.; Cai, Q. J.; Li, Y. L.; Kang, E. T.; Neoh, K. G. *Biomacromolecules* **2005**, *6*, 1012-1020.
98. Xu, F. J.; Zhong, S. P.; Yung, L. Y. L.; Tong, Y. W.; Kang, E. T.; Neoh, K. G. *Biomaterials* **2006**, *27*, 1236-1245.
99. Edmondson, S.; Huck, W. T. S. *Journal of Materials Chemistry* **2004**, *14*, 730-734.
100. Dolmatov, V. Y.; Burkat, G. K. *Journal of Superhard Materials* **2000**, 84-95.
101. Dolmatov, V. Y.; Kostrova, L. N. *Journal of Superhard Materials* **2000**, 82-85.
102. Zhu, Y. W.; Shen, X. Q.; Wang, B. C.; Xu, X. Y.; Feng, Z. J. *Physics of the Solid State* **2004**, *46*, 681-684.
103. Liu, Y.; Khabashesku, V. N.; Halas, N. J. *Journal of the American Chemical Society* **2005**, *127*, 3712-3713.

104. Matyjaszewski, K. *Current Organic Chemistry* **2002**, *6*, 67-82.
105. Qin, S. H.; Matyjaszewski, K.; Xu, H.; Sheiko, S. S. *Macromolecules* **2003**, *36*, 605-612.
106. Qin, S. H.; Saget, J.; Pyun, J. R.; Jia, S. J.; Kowalewski, T.; Matyjaszewski, K. *Macromolecules* **2003**, *36*, 8969-8977.
107. Kang, I. P.; Heung, Y. Y.; Kim, J. H.; Lee, J. W.; Gollapudi, R.; Subramaniam, S.; Narasimhadevara, S.; Hurd, D.; Kirikera, G. R.; Shanov, V.; Schulz, M. J.; Shi, D. L.; Boerio, J.; Mall, S.; Ruggles-Wren, M. *Composites Part B-Engineering* **2006**, *37*, 382-394.
108. Yun, Y. H.; Gollapudi, I. K.; Lee, R. J. W.; Hurd, D.; Shanov, V. N.; Schulz, M. J.; Kim, J.; Shi, D.; Boerio, J. F.; Subramaniam, S. *Proceedings of SPIE (Optical Engineering) 5763 (Smart Electronics, MEMS, BioMEMS, and nanotechnology)* **2005**.
109. Terrones, M.; Endo, M.; Rao, A. M.; Kim, Y. A.; Hayashi, T.; Terrones, H.; Chaliar, J. C.; Dresselhaus, G.; Dresselhaus, M. S. *Materials Today* **2004**, *7*, 30-45.
110. Hsieh, C. T.; Chen, J. M.; Kuo, R. R.; Huang, Y. H. *Applied Physics Letters* **2004**, *84*, 1186-1188.
111. Roy, R. K.; Chowdhury, M. P.; Pal, A. K. *Vacuum* **2005**, *77*, 223-229.
112. Jang, J.; Bae, J. *Sensors and Actuators B-Chemical* **2007**, *122*, 7-13.
113. Zhang, B.; Fu, R. W.; Zhang, M. Q.; Dong, X. N.; Zhao, B.; Wang, L. C.; Pittman, C. U. *Composites Part a-Applied Science and Manufacturing* **2006**, *37*, 1884-1889.
114. Zhang, B.; Fu, R. W.; Zhang, M. Q.; Dong, X. M.; Wang, L. C.; Pittman, C. U. *Materials Research Bulletin* **2006**, *41*, 553-562.
115. Wei, G.; Fujiki, K.; Saitoh, H.; Shirai, K.; Tsubokawa, N. *Polymer Journal* **2004**, *36*, 316-322.
116. Safadi, B.; Andrews, R.; Grulke, E. A. *Journal of Applied Polymer Science* **2002**, *84*, 2660-2669.
117. Allaouia, A.; Baiab, S.; Chengb, H. M.; Baia, J. B. *Composites Science and*

- Technology* **2002**, 62, 1993-1998.
118. Someya, T.; Small, J.; Kim, P.; Nuckolls, C.; Yardley, J. T. *Nano Letters* **2003**, 3, 877-881.
 119. Hutchison, G. R.; Ratner, M. A.; Marks, T. J.; Naaman, R. *Journal of Physical Chemistry B* **2001**, 105, 2881-2884.
 120. Philip, B.; Abraham, J. K.; Chandrasekhar, A.; Varadan, V. K. *Smart materials & structures* **2003**, 12, 935-939.
 121. Groszek, A. J.; Andrews, G. I. *Conf. Ind. Carbons Graphite* **1971**, 156-164.
 122. Brandrup, J.; Immergut, E. H.; Grulke, E. A. *Polymer Handbook*; 4th ed.; Wiley, NY, **1999**.
 123. Krutovertsev, S.A.; Sorokin, S. I.; Zorin, A. V.; Letchy, Y. A.; Antonova, O. Y. *Sensors and Actuators B-Chemical* **1992**, 7, 492-494.
 124. Field, P. E.; Combs, R. J. *Journal of Solution Chemistry* **2002**, 31, 719-742.
 125. Hu, Y. H.; Shenderova, O. A.; Hu, Z.; Padgett, C. W.; Brenner, D. W. *Reports on Progress in Physics* **2006**, 69, 1847-1895.
 126. Detkov PY, P. V., Kulichikhin VG, and Chukhaeva SI *Molecular building blocks for nanotechnology : from diamondoids to nanoscale materials and applications* **2007**, 109, 29-43.
 127. Shenderova, O. A.; Gruen, D. M. *Ultrananocrystalline diamond: synthesis, properties, and applications*; William-Andrew Publishing: Norwich, NY, **2006**.
 128. Choi, Y. K.; Sugimoto, K.; Song, S. M.; Endo, M. *Composites Part a-Applied Science and Manufacturing* **2006**, 37, 1944-1951.
 129. Cho, M. H.; Bahadur, S. *Tribology Letters* **2007**, 25, 237-245.
 130. Yang, S. Y.; Taha-Tijerina, J.; Serrato-Diaz, V.; Hernandez, K.; Lozano, K. *Composites Part B-Engineering* **2007**, 38, 228-235.
 131. Kabir, M. E.; Saha, M. C.; Jeelani, S. *Materials Science and Engineering a-Structural Materials Properties Microstructure and Processing* **2007**, 459,

111-116.

132. Gao, Y.; He, P.; Lian, J.; Wang, L. M.; Qian, D.; Zhao, J.; Wang, W.; Schulz, M. J.; Zhang, J.; Zhou, X. P.; Shi, D. L. *Journal of Macromolecular Science Part B-Physics* **2006**, *45*, 671-679.
133. Salehi-Khojin, A.; Jana, S.; Zhong, W. H. *Journal of Nanoscience and Nanotechnology* **2007**, *7*, 898-906.
134. Zhamu, A.; Jana, S.; Salehi-Khojin, A.; Kolodka, E.; Gan, Y. X.; Zhong, W. H. *Composite Interfaces* **2007**, *14*, 177-198.
135. Jana, S. M.; Zhong, W. H.; Gan, Y. X. *Materials Science and Engineering a-Structural Materials Properties Microstructure and Processing* **2007**, *445*, 106-112.
136. Zhamu, A.; Wingert, M.; Jana, S.; Zhong, W. H.; Stone, J. J. *Composites Part a-Applied Science and Manufacturing* **2007**, *38*, 699-709.
137. Shenderova, O.; Tyler, T.; Cunningham, G.; Ray, M.; Walsh, J.; Casulli, M.; Hens, S.; McGuire, G.; Kuznetsov, V.; Lipa, S. *Diamond and Related Materials* **2007**, *16*, 1213-1217.
138. Fedoseev, M.; Gurina, M.; Sdobnov, V.; Kondyurin, A. *Journal of Raman Spectroscopy* **1996**, *27*, 413-418.
139. Bukowska, A.; Bukowski, W. *Organic Process Research & Development* **1999**, *3*, 432-436.
140. Khalafi-Nezhad, A.; Rad, M. N. S.; Khoshnood, A. *Synthesis-Stuttgart* **2003**, 2552-2558.
141. Tokar, R.; Kubisa, P.; Penczek, S.; Dworak, A. *Macromolecules* **1994**, *27*, 320-322.
142. Shao, J. J. H., P.; Liu, Y. H.; Yang, X. H.; Wang, X. L. *Journal of Shanghai Jiaotong University* **2004**, *38*, 1764-1767.
143. Royappa, A. T. *Journal of Applied Polymer Science* **1997**, *65*, 1897-1904.
144. Giamberini, M.; Reina, J. A.; Ronda, J. C. *Journal of Polymer Science Part a-Polymer Chemistry* **2006**, *44*, 1722-1733.